

The Outer Stellar Mass of Massive Galaxies: A Simple Tracer of Halo Mass with Scatter Comparable to Richness and Reduced Projection Effects

Song Huang (黄崧) ^{1,2*}, Alexie Leauthaud ², Christopher Bradshaw ², Andrew Hearin ³, Peter Behroozi ⁴, Johannes Lange ^{2,5}, Jenny Greene ¹, Joseph DeRose ⁶, Joshua S. Speagle (沈佳士) ^{7,8,9}, Enia Xhakaj²

¹Department of Astrophysical Sciences, Peyton Hall, Princeton University, Princeton, NJ 08540, USA

²Department of Astronomy and Astrophysics, University of California Santa Cruz, 1156 High St., Santa Cruz, CA 95064, USA

³Argonne National Laboratory, Argonne, IL 60439, USA

⁴Department of Astronomy and Steward Observatory, University of Arizona, Tucson, AZ 85721, USA

⁵Kavli Institute for Particle Astrophysics and Cosmology and Department of Physics, Stanford University, CA 94305, USA

⁶Lawrence Berkeley National Laboratory, 1 Cyclotron Road, Berkeley, CA 93720, USA

⁷Department of Statistical Sciences, University of Toronto, Toronto, M5S 3G3, Canada

⁸David A. Dunlap Department of Astronomy & Astrophysics, University of Toronto, Toronto, M5S 3H4, Canada

⁹Dunlap Institute for Astronomy & Astrophysics, University of Toronto, Toronto, M5S 3H4, Canada

Accepted 2021. Received 2021; in original form 2021 Sep 1

ABSTRACT

Using the weak gravitational lensing data from the Hyper Suprime-Cam Subaru Strategic Program (HSC survey), we study the potential of different stellar mass estimates in tracing halo mass. We consider galaxies with $\log_{10}(M_{\star}/M_{\odot}) > 11.5$ at $0.2 < z < 0.5$ with carefully measured light profiles, and clusters from the redMaPPer and CAMIRA richness-based algorithms. We devise a method (the “Top- N test”) to evaluate the scatter in the halo mass-observable relation for different tracers, and to inter-compare halo mass proxies in four number density bins using stacked galaxy-galaxy lensing profiles. This test reveals three key findings. Stellar masses based on CModel photometry and aperture luminosity within $R < 30$ kpc are poor proxies of halo mass. In contrast, the stellar mass of the outer envelope is an excellent halo mass proxy. The stellar mass within $R = [50, 100]$ kpc, $M_{\star,[50,100]}$, has performance comparable to the state-of-the-art richness-based cluster finders at $\log_{10} M_{\text{vir}} \gtrsim 14.0$ and could be a better halo mass tracer at lower halo masses. Finally, using N-body simulations, we find that the lensing profiles of massive halos selected by $M_{\star,[50,100]}$ are consistent with the expectation for a sample without projection or mis-centering effects. Richness-selected clusters, on the other hand, display an excess at $R \sim 1$ Mpc in their lensing profiles, which may suggest a more significant impact from selection biases. These results suggest that M_{\star} -based tracers have distinct advantages in identifying massive halos, which could open up new avenues for cluster cosmology. The codes and data used in this work can be found here: [🔗](#)

Key words: cosmology: observations – gravitational lensing: weak – galaxies: structure – galaxies: cluster: general – galaxies: haloes

1 INTRODUCTION

With the rapid developments of multi-wavelength sky surveys, galaxy clusters have become increasingly important for

studies of cosmology and the galaxy-halo connection. As the rare highest density peaks of the matter density distribution, galaxy clusters have long been recognised as powerful probes of the mean cosmic matter density (Ω_m), the amplitude of the power spectrum (σ_8), and the cosmic expansion (e.g., Evrard 1989; Peebles et al. 1989; White et al. 1993; Viana & Liddle 1996; Wang & Steinhardt 1998; Wagoner et al.

* E-mail: sh19@astro.princeton.edu (SH)

2021; see Allen et al. 2011; Kravtsov & Borgani 2012; Weinberg et al. 2013 for recent reviews). The abundance, spatial distribution, and total mass distributions of galaxy clusters encode valuable cosmological information (see, e.g., Haiman et al. 2001; Holder et al. 2001; Vikhlinin et al. 2009; Rozo et al. 2010; Benson et al. 2013; Mantz et al. 2014; Bocquet et al. 2019; Abbott et al. 2020a; To et al. 2021b,a; Wu et al. 2021). Galaxy clusters are also promising laboratories for studying the boundaries of dark matter halos (e.g., Diemer & Kravtsov 2014; More et al. 2015, 2016; Chang et al. 2018; Shin et al. 2019; Zürcher & More 2019; Tomooka et al. 2020; Xhakaj et al. 2020)¹, and for investigating halo assembly bias (e.g., Tinker et al. 2012; Miyatake et al. 2016; Zu et al. 2017). To achieve these goals, a reliable “cluster finder” that can identify galaxy clusters is fundamental. In addition the identification of clusters, it is also critical to be able to measure the halo masses of clusters, as well as to calibrate halo mass–observable scaling relations.

Thanks to the advent of large optical surveys such as the Sloan Digital Sky Survey (SDSS, York et al. 2000; Abazajian et al. 2009; Ahumada et al. 2020)², the Dark Energy Survey (DES, Dark Energy Survey Collaboration et al. 2016; Abbott et al. 2018; DES Collaboration et al. 2021)³, and the Hyper Suprime-Cam Subaru Strategic Program (HSC-SSP, Miyazaki et al. 2012; Aihara et al. 2017a,b, 2019)⁴, optical cluster finders are widely used to construct cluster samples (e.g., Kepner et al. 1999; Gladders & Yee 2000; Koester et al. 2007; Hao et al. 2010; Wen et al. 2012; Rykoff et al. 2014; Oguri et al. 2018; Aguena et al. 2021; Wen & Han 2021; Zou et al. 2021), and weak gravitational lensing is also regarded as the most promising approach for calibrating mass-observable relations (e.g., Leauthaud et al. 2010; Becker & Kravtsov 2011; von der Linden et al. 2014; Applegate et al. 2014, 2016; Okabe & Smith 2016; Grandis et al. 2019; also see Umetsu 2020 for a recent review). Among optical cluster finders, red–sequence based methods such as redMaPPer (e.g., Rykoff et al. 2014; Rozo & Rykoff 2014; Rozo et al. 2015a,b; Rykoff et al. 2016) and CAMIRA (e.g., Oguri 2014; Oguri et al. 2018) are among the most widely-used in the literature.

While red–sequence cluster finders enjoy many successes, these methods are subject to numerous potential sources of systematic error, such as anisotropic selection biases (including both projection bias and orientation bias; e.g., Noh & Cohn 2012; Dietrich et al. 2014; Osato et al. 2018; Herbonnet et al. 2019) and mis-centering (e.g., Saro et al. 2015; Zhang et al. 2019a). Projection effects arising from structures surrounding the clusters in the line-of-sight direction raise a number of especially challenging difficulties (e.g., Cohn et al. 2007; Erickson et al. 2011; Farahi et al. 2016; Zu et al. 2017; Busch & White 2017; Costanzi et al. 2019; Sunayama & More 2019; Sunayama et al. 2020). In particular, projection effects can significantly complicate the calibration of the mass–richness relation, which in turn impacts cosmological inference (e.g., Erickson et al. 2011; Costanzi et al. 2019; Sunayama et al. 2020; Wu et al. 2021).

In Abbott et al. (2020b), the authors conclude that projection effects alone can lead to a $\sim 20\%$ over-estimate of halo mass in a given richness bin, and could lead to a “tension” with a Planck 2018 cosmology (e.g., Planck Collaboration et al. 2020). However, it is difficult to precisely evaluate the impact of projection effects on red–sequence cluster finders, because such a quantification requires realistic mock catalogues of cluster galaxies with red–sequences that are consistent with observations, which is not an easy task (e.g., DeRose et al. 2019; Korytov et al. 2019).

In this context, it is of great interest to study potential alternative methods that might suffer less from projection effects. One example is to use the light from massive central galaxies (or the brightest cluster galaxy, BCG). The stellar mass of the BCG follows a well-established stellar–halo mass relation (SHMR, e.g., Leauthaud et al. 2012; Tinker et al. 2017; Kravtsov et al. 2018; also see Wechsler & Tinker 2018 for a recent review) with moderate scatter at the high-mass end (e.g., More et al. 2009; Leauthaud et al. 2012; Reddick et al. 2013; Zu & Mandelbaum 2015; Lehmann et al. 2017; Kravtsov et al. 2018). Historically, BCG luminosity or stellar mass has not been considered as a competitive halo mass proxy, but optical surveys have also struggled to accurately measure BCG total luminosity (e.g., Bernardi et al. 2013; Huang et al. 2018c). Recently, deep imaging surveys have showed that total BCG luminosity may correlate well with halo mass (e.g., Huang et al. 2018a; Sampaio-Santos et al. 2021). In Huang et al. (2020), for example, the authors showed that a simple phenomenological model based on the stellar masses of BCGs measured within two apertures further reduces the scatter in the halo mass – observable relation. In addition, recent work has also highlighted the connection between the diffuse envelope around a BCG (often referred to as the Intra-Cluster Light, or ICL) and dark matter halo mass (e.g., Montes & Trujillo 2018, 2019; Zhang et al. 2019a; Furnell et al. 2021).

In this paper, we use data from the HSC survey to quantify the potential of using BCG light to identify massive clusters. We design a so-called Top- N test to evaluate their relative performance with respect to the red–sequence methods. The Top- N test compares the stacked galaxy–galaxy lensing profiles (the excess surface density profiles, or the $\Delta\Sigma$ profiles) of “clusters” selected by different halo mass proxies in fixed number density bins (e.g., Reyes et al. 2008). We model these lensing signals using cosmological simulations and evaluate the scatter of the halo mass–observable relations. Section 2 explains the philosophy behind the Top- N test and the methodology for estimating the scatter in mass–observable relations. Section 3 presents the data and Section 4 presents key measurements, including different M_* measurements based on 1-D mass profiles and galaxy–galaxy lensing profiles. Section 5 presents the different proxies that we test. Our results are presented in Section 6 and discussed in Section 7. Finally, we summarise and conclude in Section 8.

We assume $H_0 = 70 \text{ km s}^{-1} \text{ Mpc}^{-1}$, $\Omega_m = 0.3$, and $\Omega_\Lambda = 0.7$. Stellar mass (M_*) is derived using a Chabrier Initial Mass Function (IMF; Chabrier 2003). We adopt M_{vir} for dark matter halo mass as defined in Bryan & Norman 1998. We use $\mathcal{M} \equiv \log_{10}(M_{\text{vir}}/M_\odot)$ and $\mathcal{O} \equiv \log_{10}$ Observable to indicate the ten-base logarithms of halo mass and observ-

¹ Please see [Benedikt Diemer’s webpage](#) for a more complete list of reference on this topic.

² <https://www.sdss.org/>

³ <https://www.darkenergysurvey.org/>

⁴ <https://hsc.mtk.nao.ac.jp/ssp/>

ables. We also use $\sigma_{M_{\text{vir}}} \equiv \sigma_{\log_{10} M_{\text{vir}}}$ for the scatter of halo mass and $\sigma_{M_*} \equiv \sigma_{\log_{10} M_*}$ for the scatter of stellar mass.

2 METHODOLOGY AND MODELLING FRAMEWORK

This section explains the basic idea of the Top- N test and presents our modelling framework for estimating the scatter in M_{vir} -observable relations.

2.1 Philosophy of the Top- N Test

Cosmological simulations permit a precise prediction for how $\Delta\Sigma$ of dark matter halos scales with true halo mass, M_{vir} . Since simulated halos can easily be rank-ordered by their mass, it is a trivial matter to use a cosmological simulation to generate a prediction for the $\Delta\Sigma$ profiles of samples of dark matter halos that have been stacked according to number density. The philosophy behind the Top- N test is to capitalise upon this predictive power. When analysing observational data, of course one does not have direct access to true halo mass, and so one must instead rely upon an observational proxy. In the analogous manner as can be done for simulated halos, observed galaxy clusters can be arranged into stacked samples according to any particular halo mass proxy, and so it is equally straightforward to measure the $\Delta\Sigma$ profile of clusters as a function of the number density defined by the choice of proxy. When the halo mass proxy presents a scaling relation with M_{vir} that has low scatter and a steep slope, then the associated stacked samples will exhibit a lensing amplitude that scales steeply with number density, and the stacks will furthermore exhibit $\Delta\Sigma$ profiles whose shape closely resembles the profile of M_{vir} -ranked stacks of simulated halos of the corresponding number density. For example, by comparing the stacked $\Delta\Sigma$ profile of the top 100 most massive galaxies with the $\Delta\Sigma$ profile of the top 100 richest clusters selected in the same survey volume, one can compare which of these proxies is more “ M_{vir} -like”. In this manner, the Top- N test compares $\Delta\Sigma$ for cluster samples defined in bins of fixed number density, and uses such comparisons to inform the optimal choice of halo mass proxy.

Figure 1 illustrates the main idea of the Top- N test using halos from the MultiDark Planck 2 (MDPL2)⁵ simulation. In this exercise, each halo is characterised by its true halo mass, $\mathcal{M} \equiv \log_{10} M_{\text{vir}}$, and additionally by three hypothetical observables, $\mathcal{O} \equiv \log_{10}(\text{Observable})$. We assume that each \mathcal{O} follows a log-linear scaling relation with M_{vir} that is characterised by a value for the slope, α , and by a level of Gaussian scatter in \mathcal{O} at fixed \mathcal{M} , $\sigma_{\mathcal{O}|\mathcal{M}}$ (e.g., Lieu et al. 2016, Ziparo et al. 2016, Evrard et al. 2014; Farahi et al. 2018). We then select the top $N = 5000$ objects using \mathcal{O} to rank-order the clusters. The value of N translates into a fixed volume number density threshold shown on the right sub-panel using the number density distributions of these observables. When comparing the M_{vir} distributions of the Top- N -selected samples (bottom panel), the halo mass proxies with smaller α and/or larger $\sigma_{\mathcal{O}|\mathcal{M}}$ result in M_{vir} distributions with larger $\sigma_{\mathcal{M}|\mathcal{O}}$ and lower mean M_{vir} . This

selection at fixed number density (Top- N selection) yields a M_{vir} distribution that reflects the properties of the underlying M_{vir} -observable relation. Figure 1 also shows the *stacked* $\Delta\Sigma$ profiles of these Top- N samples. The Top- N sample with a higher mean M_{vir} and a lower value of $\sigma_{\mathcal{M}|\mathcal{O}}$ has a $\Delta\Sigma$ profile with larger overall amplitude. We can therefore use the *stacked* $\Delta\Sigma$ profiles of different Top- N samples to probe their underlying M_{vir} -observable relations. Reyes et al. (2008) applied a similar method to develop improved halo mass tracers of clusters.

The right panel of Figure 1 illustrates that the ratio of $\Delta\Sigma$ profiles exhibits scale-dependent features that reveal subtle differences in other halo properties, and also in large-scale environment. Our use of Top- N tests in this paper will additionally leverage the discriminating power of this scale-dependence when assessing various halo mass proxies.

Finally, Figure 1 also reveals a degeneracy between the slope, α , and the scatter, $\sigma_{\mathcal{O}|\mathcal{M}}$, such that different combinations of α and $\sigma_{\mathcal{O}|\mathcal{M}}$ can produce identical M_{vir} distributions. We discuss this degeneracy in the next section (§ 2.2.1).

2.2 Modelling Methodology

To quantitatively interpret differences between $\Delta\Sigma$ profiles, we develop a simple forward-modelling method based on data from the MDPL2 and the Small MultiDark Planck (SMDPL)⁶ N-body simulations (e.g., Klypin et al. 2016). We assume a log-linear M_{vir} -observable relation with a constant Gaussian scatter. We use this model to estimate the scatter in the mass-proxy relation, and also to infer the underlying M_{vir} distribution of different samples.

2.2.1 The relationship between $\sigma_{\mathcal{M}|\mathcal{O}}$, $\sigma_{\mathcal{O}|\mathcal{M}}$, and α

In this section, we use a simple analytic model to explore the connection between the scatter and slope of the log-linear M_{vir} -observable relation and the amplitude of the $\Delta\Sigma$ profiles.

The shape of the halo mass function (HMF) directly influences the characteristics of a M_{vir} -observable relation (e.g., Tinker et al. 2008). We will first use an analytic form of the HMF to demonstrate the relation between $\sigma_{\mathcal{M}|\mathcal{O}}$ and $\sigma_{\mathcal{O}|\mathcal{M}}$. We approximate the HMF using the following exponential functional form suitable for the high- M_{vir} end:

$$\Phi(\mu) \equiv \frac{dn(\mathcal{M})}{d\mu} = \exp\left(\beta_0 - \beta_1 \mathcal{M} - \frac{\beta_2}{2} \mathcal{M}^2\right). \quad (1)$$

For large values of mass, the HMF declines rapidly with M_{vir} ($\beta_1 > 0$) with a steepening slope ($\beta_2 > 0$)⁷. We model the halo mass proxy \mathcal{O} to follow a log-linear relation with a constant log-normal scatter value:

$$\mathcal{O} = \mathcal{N}(\alpha \mathcal{M} + \pi, \sigma_{\mathcal{O}|\mathcal{M}}). \quad (2)$$

The $\sigma_{\mathcal{O}|\mathcal{M}}$ value here is often quoted as the “scatter of

⁵ <https://www.cosmosim.org/cms/simulations/mdpl2/>

⁶ <https://www.cosmosim.org/cms/simulations/smdpl/>

⁷ For the MDPL2 HMF at $z \sim 0.4$, we adopt the best-fit parameter values of $\beta_0 = -0.558$, $\beta_1 = 0.670$, and $\beta_2 = 2.959$.

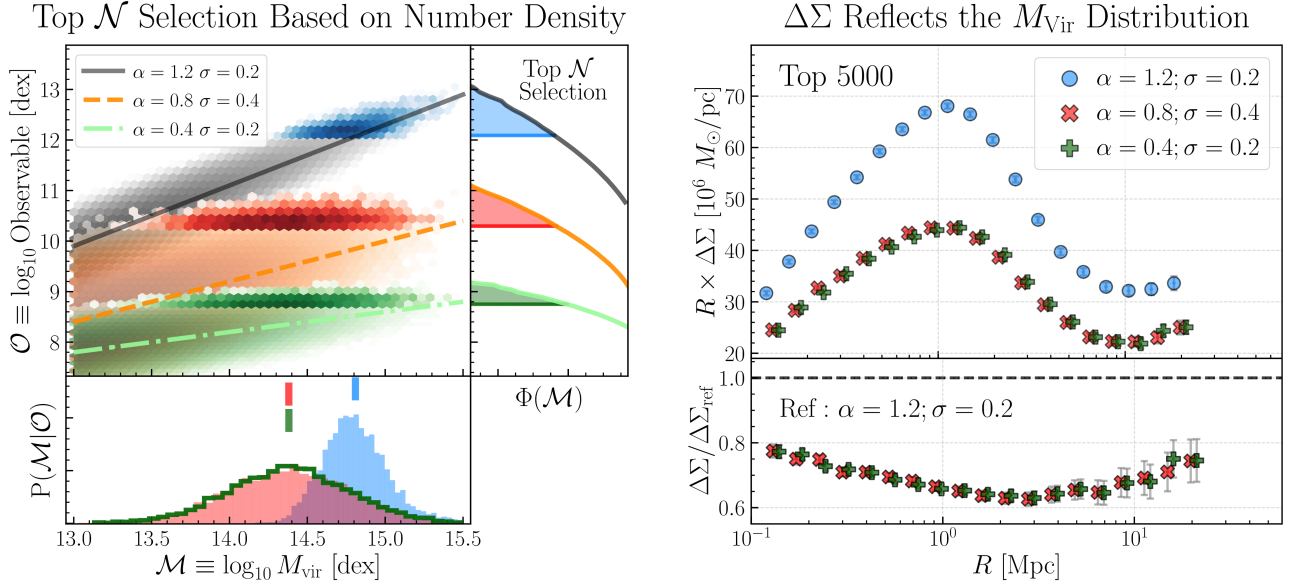


Figure 1. **Left:** coloured hexbins and corresponding lines illustrate three mock M_{vir} –observable relations with different slope and scatter values (grey: $\alpha = 1.2$ and $\sigma_{\mathcal{O}|\mathcal{M}} = 0.2$; orange: $\alpha = 0.8$ and $\sigma_{\mathcal{O}|\mathcal{M}} = 0.4$; light green: $\alpha = 0.4$ and $\sigma_{\mathcal{O}|\mathcal{M}} = 0.2$). Hexbins with darker colours highlight the top 5000 objects for each observable. The right panel shows the number density distributions of these observables and highlights the Top- N selections using shaded regions with corresponding colours. The bottom panel shows the M_{vir} distributions of the three Top- N bins. We use short vertical bars to indicate the mean M_{vir} values. **Right:** stacked $R \times \Delta\Sigma$ profiles of the three Top- N samples using the MDPL2 simulation. The bottom panel shows the ratios of lensing profiles using the sample with the steepest slope (blue) as a reference. The **Jupyter** notebook for reproducing this figure can be found here: [🔗](#).

the SHMR” (e.g., More et al. 2011; Leauthaud et al. 2012; Reddick et al. 2013; Behroozi et al. 2013) and has been frequently used to infer physical information about galaxy formation (e.g., Gu et al. 2016; Matthee et al. 2017; Tinker 2017; Wechsler & Tinker 2018). Yet it is the scatter of M_{vir} at fixed observable, $\sigma_{\mathcal{M}|\mathcal{O}}$, that we estimate in observations using the Top- N test. We now briefly discuss the connection between $\sigma_{\mathcal{O}|\mathcal{M}}$ and $\sigma_{\mathcal{M}|\mathcal{O}}$. First, the probability density of the observable \mathcal{O} is given by,

$$P(\mathcal{O}) \equiv \int_0^\infty \Phi(\mu) P(\mathcal{O}|\mathcal{M}) d\mathcal{M} \quad (3)$$

At fixed \mathcal{O} , the mean value of \mathcal{M} is,

$$\begin{aligned} \langle \mathcal{M}|\mathcal{O} \rangle &= \frac{1}{P(\mathcal{O})} \int_0^\infty \Phi(\mu) P(\mathcal{O}|\mathcal{M}) \mathcal{M} d\mathcal{M} \\ &= \frac{\left(\frac{\mathcal{O} - \pi}{\alpha} - \beta_1 \left(\frac{\sigma_{\mathcal{O}|\mathcal{M}}}{\alpha} \right)^2 \right)}{1 + \beta_2 \left(\frac{\sigma_{\mathcal{O}|\mathcal{M}}}{\alpha} \right)^2} \end{aligned} \quad (4)$$

The three components of $\langle \mathcal{M}|\mathcal{O} \rangle$ are:

- (i) The mean relation between the observable and halo mass, $(\mathcal{O} - \pi)/\alpha$.
- (ii) A shift due to the Eddington bias caused by the linear slope of the HMF, $-\beta_1 \left(\frac{\sigma_{\mathcal{O}|\mathcal{M}}}{\alpha} \right)^2$. In the case of $\beta_1 > 0$, this shift is to lower \mathcal{M} as there are more low \mathcal{M} objects up-scattered into the selection.
- (iii) A second shift is caused by the curvature of the HMF, $(1 + \beta_2 \left(\frac{\sigma_{\mathcal{O}|\mathcal{M}}}{\alpha} \right)^2)^{-1}$. Again, $\beta_2 > 0$ results in more low \mathcal{M} objects and thus a shift to lower \mathcal{M} .

For the scatter in \mathcal{M} at fixed \mathcal{O} , we have

$$\begin{aligned} \sigma_{\mathcal{M}|\mathcal{O}} &= \frac{1}{P(\mathcal{O})} \int_0^\infty \Phi(\mu) P(\mathcal{O}|\mathcal{M}) (\mathcal{M} - \langle \mathcal{M} \rangle)^2 d\mathcal{M} \\ &= \frac{\sigma_{\mathcal{O}|\mathcal{M}}}{\sqrt{\beta_2 \sigma_{\mathcal{O}|\mathcal{M}}^2 + \alpha^2}} \end{aligned} \quad (5)$$

In the case of a power law halo mass function ($\beta_2 = 0$), this expression reduces to the commonly seen $\sigma_{\mathcal{O}|\mathcal{M}}/\alpha$. The positive β_2 of the HMF decreases this scatter. Finally, the higher moments of $P(\mathcal{O})$ such as the skewness or excess kurtosis confirm that $P(\mathcal{M}|\mathcal{O})$ follows a Gaussian distribution for the approximated HMF in Equation 1.

We now rewrite Equation 5 in a more practical form that makes it clear that $\sigma_{\mathcal{M}|\mathcal{O}}$ depends on the ratio of $\sigma_{\mathcal{O}|\mathcal{M}}$ and α . This is obvious in the case of a power law mass function ($\beta_2 = 0$) and is also true for the more general quadratic form (1),

$$\sigma_{\mathcal{M}|\mathcal{O}} = \frac{\sigma_{\mathcal{O}|\mathcal{M}}}{\sqrt{\beta_2 \sigma_{\mathcal{O}|\mathcal{M}}^2 + \alpha^2}} = \left(\beta_2 + \left(\frac{\alpha}{\sigma_{\mathcal{O}|\mathcal{M}}} \right)^2 \right)^{-1/2} \quad (6)$$

This equation shows that, for a given Top- N selection, two M_{vir} –observable relations with the same $\sigma_{\mathcal{O}|\mathcal{M}}/\alpha$ ratio will have the same value $\sigma_{\mathcal{M}|\mathcal{O}}$. We demonstrate this in the right panel of Figure 1 by populating MDPL2 halos with mock observables that follow different M_{vir} –observable relations. The two observables whose M_{vir} –observable relations share the same value of $\alpha/\sigma_{\mathcal{O}|\mathcal{M}} = 2$ (red and green) lead to the same M_{vir} distributions in the top $N = 5000$ sample and result in almost identical stacked $\Delta\Sigma$ profiles.

As shown above, our Top- N test only probes the ob-

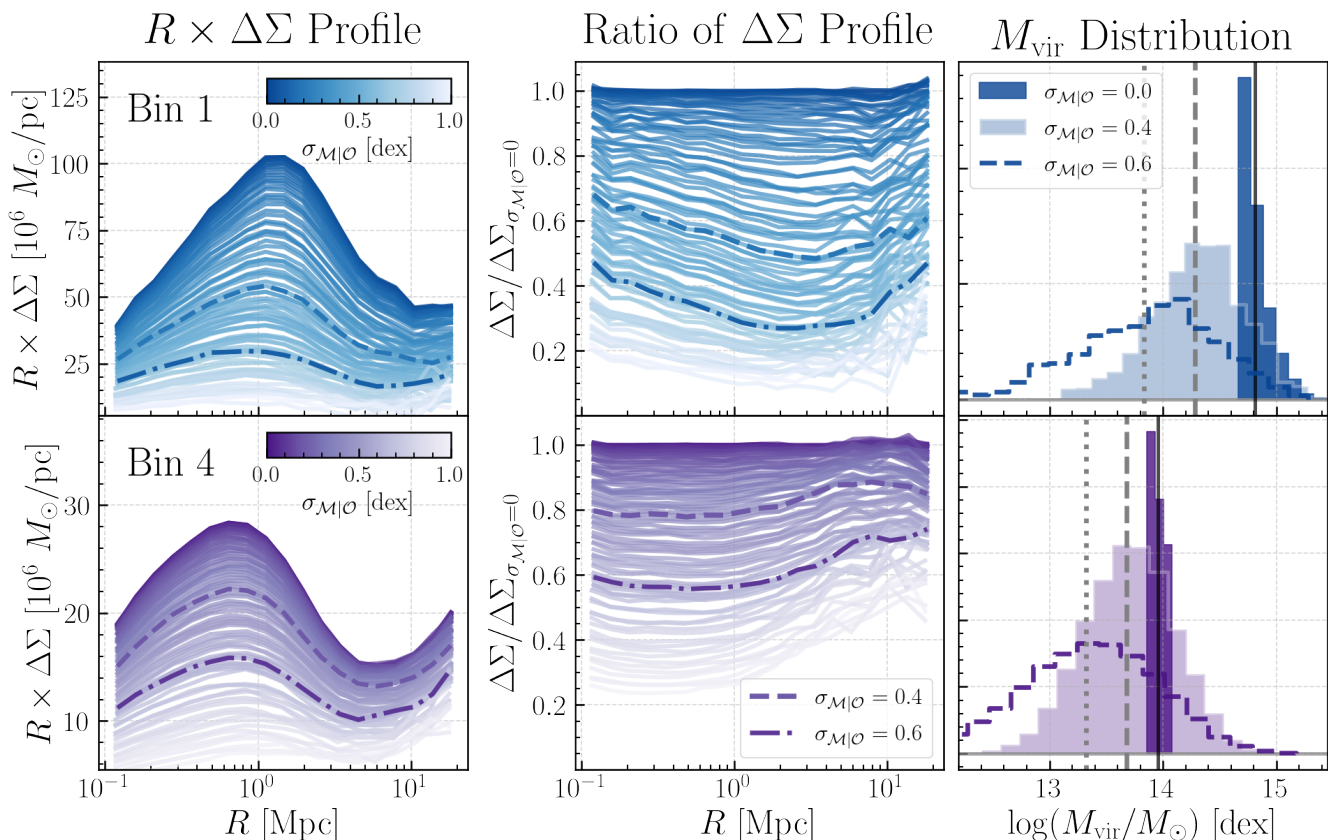


Figure 2. The $\Delta\Sigma$ profiles and M_{vir} distributions of different Top- N samples with a wide range of scatter values ($0 < \sigma_{\mathcal{M}|\mathcal{O}} < 1$). This combines data from both MDPL2 and SMDPL. The top and bottom rows display the first and last Top- N bins (the most and least massive in average M_{vir}) used in this work (see § 5.2). Their number density thresholds correspond to $0.2 < z < 0.5$ redMaPPer clusters in HSC S16A area with $35 < \lambda < 150$ (Bin 1) and $6 \leq \lambda < 10$ (Bin 4). **Left:** the $R \times \Delta\Sigma$ profiles of the Top- N samples with different $\sigma_{(s|\mu)}$ values. We highlight the profiles corresponding to $\sigma_{(s|\mu)} = 0.4$ (dashed line) and $= 0.6$ (dot-dashed line). **Middle:** the ratios between the $\Delta\Sigma$ profiles of the Top- N samples with non-zero scatter and the “perfect” sample ($\Delta\Sigma_{\sigma=0}$). **Right:** $\log M_{\text{vir}}$ distributions of the “perfect” Top- N sample and the $\sigma_{(s|\mu)} = 0.4$ and $= 0.6$ samples. Grey vertical lines indicate the mean $\log M_{\text{vir}}$ for each distribution. The **Jupyter** notebook for reproducing this figure can be found here: [🔗](#)

served M_{vir} distribution, and cannot even in principle distinguish between *i*) mass-observable relations with steep slopes and high scatter versus *ii*) mass-observable relations with shallow slopes but low scatter. We note that this degeneracy is unimportant for the present work, because here we only wish to perform *relative* comparisons between different proxies for M_{vir} . In this paper, we are not concerned with inferring the specific values of either α or $\sigma_{\mathcal{O}|\mathcal{M}}$; rather, our principal focus is on a comparative assessment of which observable proxies \mathcal{O} supply the strongest discriminating power regarding M_{vir} . For a few specific cases of \mathcal{O} that are of special importance, we will estimate the value of $\sigma_{\mathcal{O}|\mathcal{M}}$ by using the same value for the slope as is conventionally assumed in the literature on M_{vir} -observable relations. This allows us to inter-compare different proxies using $\sigma_{\mathcal{O}|\mathcal{M}}$, and also to make comparisons with previous results from observations or hydro simulations. However, we reiterate that in such cases, the specific value of our estimate on $\sigma_{\mathcal{O}|\mathcal{M}}$ will strictly depend upon the assumed values for the slope α , as this mathematical degeneracy cannot be evaded.

2.2.2 Estimating $\sigma_{\mathcal{M}|\mathcal{O}}$

The discussion in § 2.2.1 demonstrates that we can compare the $\sigma_{\mathcal{M}|\mathcal{O}}$ values of two Top- N samples using their stacked $\Delta\Sigma$ profiles: the sample selected by the “better” M_{vir} tracer should yield a $\Delta\Sigma$ profile with higher amplitude. More importantly, we can also estimate $\sigma_{\mathcal{M}|\mathcal{O}}$ from $\Delta\Sigma$ profiles by comparing with model profiles built from simulations using the same number density selection.

We build our model by populating halos in simulations with mock observables that follow log-linear relations (Equation 2) with fixed slope value at $\alpha = 1$ (see justification in previous section) but with different $\sigma_{\mathcal{O}|\mathcal{M}}$ values. In each realisation, we derive the best-fit $\mathcal{M}|\mathcal{O}$ relation and estimate the $\sigma_{\mathcal{M}|\mathcal{O}}$ value for the same pre-defined number density bins (Top- N bins) used in the observations. For each Top- N bin, we calculate the stacked $\Delta\Sigma$ profiles and store the underlying M_{vir} distributions at different $\sigma_{\mathcal{M}|\mathcal{O}}$ values. We adopt a densely sampled grid of $\sigma_{\mathcal{M}|\mathcal{O}}$ values between 0.0 and 1.0 dex.

Observations suggest that at high- M_{vir} and low redshift, $\sigma_{\mathcal{O}|\mathcal{M}} = 0.2$ dex (e.g., More et al. 2011; Leauthaud et al. 2012; Reddick et al. 2013; Behroozi et al. 2013; Tinker et al. 2017). Given the slope of the SHMR, this means that $\sigma_{\mathcal{M}|\mathcal{O}}$

is expected to be in the ~ 0.4 - 0.6 dex range (e.g., Figure 5 & 7 of Wechsler & Tinker 2018). Therefore it is essential to cover a large range in $\sigma_{M|O}$ values.

We use the `mean_delta_sigma` function from `halotools` (Hearin et al. 2017)⁸ to calculate the stacked $\Delta\Sigma$ profiles based on the algorithm described in the Appendix B of Lange et al. (2019) in comoving coordinates. We then convert them into physical coordinates before comparing to observations. We use 50 (10) millions down-sampled particles from the MDPL2 (SMDPL) simulations for the calculation and choose the Z direction as the line-of-sight. The MDPL2 simulation has a large box size of 1 Gpc/h that helps sample the very high- M_{vir} end of HMF. However, its particle mass resolution ($1.51 \times 10^9 M_{\odot}/h$) is not sufficient to resolve the $< 10^{12.5} M_{\odot}/h$ halos presented in samples with large $\sigma_{M|O}$ values. In contrast, the SMDPL simulation has a much better mass resolution ($9.63 \times 10^7 M_{\odot}/h$) for calculating accurate $\Delta\Sigma$ profiles for less massive halos but does not have sufficient volume (box size = 0.4 Gpc/h) to sample the very high- M_{vir} end. Therefore, we combine the predictions from the MDPL2 and SMDPL simulations. We use the MDPL2 simulation to cover the $0.00 < \sigma_{M|O} < 0.65$ dex range with a 0.01 dex grid, and use SMDPL to cover the $0.65 < \sigma_{M|O} < 1.0$ dex range with a 0.05 dex grid size. Using the overlapping $\sigma_{M|O}$ range, we confirm the two simulations provide $\Delta\Sigma$ profiles that are consistent within their statistical uncertainties. We use the $z = 0.364$ snapshot from MDPL2 and the $z = 0.404$ snapshot from SMDPL, which are the closest ones to the mean redshift (~ 0.4) of the HSC sample.

Figure 2 shows the predicted $\Delta\Sigma$ profiles as a function of $\sigma_{M|O}$ in two number density bins. In addition to the expected decreasing $\Delta\Sigma$ amplitudes with increasing $\sigma_{M|O}$ values, we also see scale dependent differences in the ratios of the predicted $\Delta\Sigma$ profiles. We highlight the $\Delta\Sigma$ profiles with $\sigma_{M|O} = 0.4$ and 0.6 dex along with their M_{vir} distributions.

We estimate $\sigma_{M|O}$ by matching the observed $\Delta\Sigma$ profiles to the model predictions. For an observed lensing profile ($\Delta\Sigma_{\text{O}}$) and its covariance matrix (\mathbf{C}), we use the χ^2 statistic to evaluate how well a given model profile ($\Delta\Sigma_{\text{M}}$) describes the observations:

$$\chi^2 = (\Delta\Sigma_{\text{M}} - \Delta\Sigma_{\text{O}})^{\text{T}} \mathbf{C}^{-1} (\Delta\Sigma_{\text{M}} - \Delta\Sigma_{\text{O}}). \quad (7)$$

This ignores the uncertainties in the theoretical $\Delta\Sigma$ profiles (e.g., due to the stochasticity when populating halos or sample variance) which are negligible compared to the observed uncertainties. Appendix B includes further details about the fitting process. In this remainder of this paper, we will use $\sigma_{M_{\text{vir}}} \equiv \sigma_{\log M_{\text{vir}}} \equiv \sigma_{M|O}$ to refer to the scatter of halo mass at given observable.

This model only focuses on the underlying distribution of M_{vir} which is *not* the only factor that determines the $\Delta\Sigma$ profile. For example, our model does not account for mis-centering or baryonic physics – these and other effects will be discussed in later sections. To evaluate the impact of satellite galaxies on $\Delta\Sigma$ profile, we also provide a special version of the model that can match the observed stellar mass function (SMF) and clustering signals of HSC massive

galaxies. We provide more details of this model in Appendix C.

We include massive satellite galaxies in our model when comparing to HSC massive galaxies since they should present in the observed sample. For richness-selected clusters, we remove the satellite galaxies from the model before calculating the $\Delta\Sigma$ profiles. We assume the cluster finders identify the correct central galaxies even though that is not always the case. However, including satellites or not in our models does not have any impact on our results.

3 DATA

In this section, we introduce the imaging data (§ 3.1), the HSC massive galaxy sample (§ 3.2), and the richness-selected galaxy cluster catalogues (§ 3.3)

3.1 Hyper Suprime-Cam Survey Subaru Strategic Program

In this work, we use $\sim 137 \text{ deg}^2$ of deep optical images from the WIDE layer of the S16A release of the Hyper Suprime-Cam Subaru Strategic Program (HSC-SSP, or HSC survey; e.g. Aihara et al. 2017a,b, 2019)⁹ – an ambitious cosmology survey using the 8.2-m Subaru Telescope. HSC multi-band (*grizY*) images have impressive depth (~ 3 – 4 mag deeper than SDSS), superb seeing conditions (the mean *i*-band seeing has a ~ 0.58 arcsec Full-Width Half-Maximum, or FWHM), and fine pixel resolution (0.168 arcsec), all making it ideal for studying galaxy structure and performing galaxy-galaxy lensing measurements.

We use the coadd images produced by `hscPipe` 4.0.2. `hscPipe` is a specifically modified version of the Large Synoptic Survey Telescope (LSST) pipeline (e.g. Jurić et al. 2015; Axelrod et al. 2010¹⁰ for HSC¹¹). Please see Bosch et al. (2017) for more details about the data reduction process and Huang et al. (2018b) for its photometric performance. We also make use of the photometric redshift (photo-*z*) measurements of HSC galaxies from the `frankenz` (Speagle et al. 2019) algorithm. Please see Tanaka et al. (2018) for a summary of its performance. For galaxy-galaxy lensing measurements, we use the public shape catalogue for S16A¹² based on the *i*-band images and the re-Gaussianization algorithm (Hirata & Seljak 2003). HSC Y1 cosmology (e.g., Hikage et al. 2019; Hamana et al. 2020) and other cluster lensing analyses (e.g., Umetsu et al. 2020) used the same catalogue. Please see Bosch et al. (2017), Mandelbaum et al. (2018), and Mandelbaum et al. (2017) for details about the shape measurements and lensing calibration. All galaxies and clusters used in this work are filtered through the bright star masks (see Coupon et al. 2017 for details) used in the HSC S18A or PDR2 data release to avoid the contamination from saturated stars. Please refer to Huang et al. (2018c,a, 2020) for further details about the HSC data. All imaging data,

⁹ <https://hsc.mtk.nao.ac.jp/ssp/>

¹⁰ <https://pipelines.lsst.io>

¹¹ The most recent version of `hscPipe` can be found here: https://hsc.mtk.nao.ac.jp/pipedoc_e/.

¹² The S16A weak lensing shape catalogue is released here: <https://hsc-release.mtk.nao.ac.jp/doc/index.php/s16a-shape-catalog-pdr2/>

⁸ <https://github.com/astrophy/halotools>

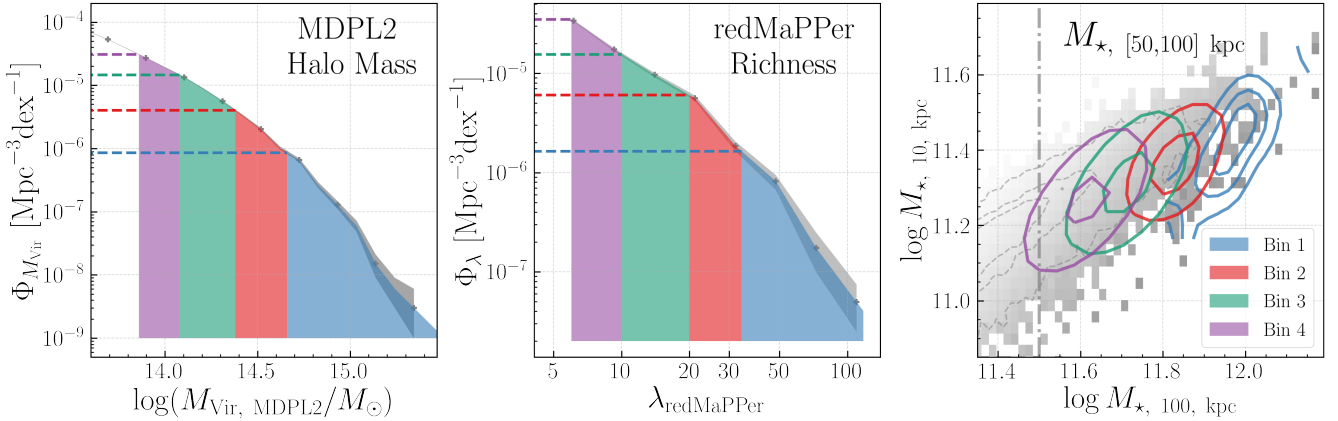


Figure 3. **Left:** the HMF of the MDPL2 simulation and the M_{vir} range of our Top- N tests for an “ideal” (zero scatter) Top- N selection. The four coloured regions highlight the M_{vir} ranges of the four Top- N bins. Dashed lines with corresponding colours label the number density boundaries of each bin. **Middle:** the richness function of the S16A redMaPPer clusters used in this work. Coloured regions reflect the λ ranges of the four bins. We describe the choice of these bins in § 5.2 and list their properties in Table 1. **Right:** The grey shaded region and the dashed-line contours show the distribution of HSC massive galaxies over the $M_{\star,100 \text{ kpc}}-M_{\star,10 \text{ kpc}}$ plane. The dot-dash line highlights $\log_{10}(M_{\star,\text{max}}/M_{\odot})=11.5$, a conservative $M_{\star,100 \text{ kpc}}$ completeness limit. The four solid-line contours with corresponding colours highlight the distributions of $M_{\star,[50,100]}$ -selected galaxies in the four Top- N bins. The Jupyter notebook for reproducing this figure can be found here: [🔗](#).

along with the photometric and the photo- z catalogues, have been released to the public¹³.

3.2 HSC Massive Galaxy Sample

Using the S16A data, we select a sample of massive galaxies at $0.19 < z < 0.52$. In this redshift range, we can resolve their inner light profile ($r < 10 \text{ kpc}$) but also have the depth to explore the faint outskirts ($r \sim 100 \text{ kpc}$). This is the same sample used in Huang et al. (2020). Please refer to Huang et al. (2020) for a detailed description of the sample, here we only provide a brief summary.

The sample contains 24926 massive galaxies selected using a cut on the CModel-based M_{\star} , $M_{\star,\text{cmod}} \geq 10^{11.2} M_{\odot}$. The $M_{\star,\text{cmod}}$ is based on the M_{\star}/L_{\star} estimated by five-band SED fitting using iSEDfit (see Moustakas et al. 2013). All galaxies have valid 1-D surface brightness profiles measured in i -band with empirical background correction that enables non-parametric M_{\star} measurements out to $> 100 \text{ kpc}$. During the extraction of the 1-D profiles, $\sim 9\%$ of the original sample was excluded due to contamination by nearby objects. We treat this as a small decrease of the effective survey area in this work. Among all 24051 galaxies, 15558 have useful spec- z . However, when making a cut using the 100 kpc aperture M_{\star} , at $M_{\star,100 \text{ kpc}} \geq 10^{11.5} M_{\odot}$, 4429 of the 4848 galaxies ($\sim 91\%$) have spec- z . And 2190 of the 2299 galaxies ($\sim 95\%$) with $M_{\star,100 \text{ kpc}} \geq 10^{11.6} M_{\odot}$ have spec- z .

Using this sample, we have uncovered remarkable structural diversity in the outer stellar halo (Huang et al. 2018c) and shown that the stellar mass distribution has a connection with M_{vir} (Huang et al. 2018a, 2020). We have also compared these observed 1-D stellar mass density profiles with those from state-of-the-art hydro-simulations to gain insights into their assembly history (Ardila et al. 2021). We release the catalogue of this massive galaxy sample here: [🔗](#).

3.3 Red Sequence Cluster catalogues

Taking advantage of the well-defined “red-sequence” of low- z galaxy clusters and the potential low-scatter nature of the M_{vir} -richness scaling relation (e.g., Rozo et al. 2009; Rykoff et al. 2012), richness-based cluster finders provide a promising way to identify massive halos in imaging data. Here we will evaluate two cluster catalogues based on red-sequence algorithms using the Top- N test by estimating the $\sigma_{M_{\text{vir}}}$ values of these two cluster samples and directly comparing their $\Delta\Sigma$ profiles to those from M_{\star} -based M_{vir} proxies. The massive galaxy sample and the cluster samples are independently selected from the same HSC footprint but there is no one-to-one correspondence between the two catalogues. For example, there are massive galaxies not contained in either cluster catalogues. We will briefly discuss this in § 7.

3.3.1 redMaPPer Clusters

redMaPPer (Rykoff et al. 2014; Rozo & Rykoff 2014; Rozo et al. 2015a,b)¹⁴ is a popular cluster finding algorithm based on the richness of red-sequence galaxies. It has been applied to several large imaging surveys including SDSS (e.g., Rykoff et al. 2014), DES (Rykoff et al. 2016; McClintock et al. 2019), and HSC. The M_{vir} -richness relation of redMaPPer clusters has been investigated in multiple works (e.g., Saro et al. 2015; Farahi et al. 2016; Simet et al. 2017; Melchior et al. 2017; Baxter et al. 2018; Murata et al. 2018; McClintock et al. 2019).

We use an internal version of the redMaPPer cluster catalogue for S16A data (Kawinwanichakij & Rykoff, private communication) based on the updated Python version of redMaPPer¹⁵. The algorithm is similar to that used in Rykoff et al. (2016) with minor modifications. At $0.19 <$

¹³ <https://hsc.mtk.nao.ac.jp/ssp/data-release>

¹⁴ <http://risa.stanford.edu/redmapper/>

¹⁵ <https://github.com/erykoff/redmapper>

$z < 0.52$, it contains 2409 clusters with $\lambda \geq 5$ and 227 with $\lambda \geq 20$. Of these clusters, 1623 have spec- z (from a variety of sources) and the rest have a high-quality photo- z from their red-sequence. The sample has a median photo- z bias of $\delta_z \sim 0.0012$ (0.0008), a scatter of $\sigma_z/(1+z) \sim 0.011$ (0.007), and a $4\text{-}\sigma$ outlier fraction of $\sim 0.7\%$ (0.5%) for $\lambda \geq 5$ (≥ 20) clusters, showing performance consistent with that of the DES catalogue (McClintock et al. 2019). We confirm that only using the photo- z from redMaPPer does not affect relevant conclusions. Regarding the completeness of the cluster sample, McClintock et al. (2019) estimates that the DES limiting magnitude is deep enough for $0.2L_*$ galaxies at $z \sim 0.7$, and that the galaxy sample for redMaPPer is $> 90\text{-}95\%$ complete. Given the deeper imaging in HSC, it is safe to expect even better completeness at $z < 0.52$.

In addition to the richness, redMaPPer provides a list of candidates of the central galaxy along with their central probability (P_{cen}). We choose the galaxy with the highest P_{cen} as the centre of the cluster. Using a sub-sample of X-ray detected clusters, Zhang et al. (2019a) analyses redMaPPer mis-centring in DES for clusters with $\lambda > 20$. They find $\sim 83\%$ of the clusters are well-centred. In the HSC redMaPPer sample, 66% (77%) of clusters have central galaxies with $P_{\text{cen}} > 0.8$ (0.7).

We also use the 364 SDSS DR8 redMaPPer clusters (Rykoff et al. 2014) with $\lambda_{\text{SDSS}} \geq 20$ in the S16A footprint to show that the results found for the HSC redMaPPer clusters also hold for SDSS redMaPPer catalogue (see Appendix § F). The SDSS sample is only complete at $z < 0.33$. In Appendix § G, we compare the stacked $\Delta\Sigma$ profiles of HSC and DES redMaPPer (e.g., Chang et al. 2018; McClintock et al. 2019) clusters in the same redshift ($0.2 < z < 0.5$) and richness ($20 \leq \lambda < 100$) bins and show they are consistent with each other.

3.3.2 CAMIRA Clusters

CAMIRA¹⁶ is a red-sequence cluster finding algorithm developed by Oguri (2014). It has been applied to SDSS (Oguri 2014) and HSC (Oguri et al. 2018) data. Unlike redMaPPer, CAMIRA does not have a richness-dependent radius, and instead counts red galaxies with $L \geq 0.2L_*$ within a fixed $R \leq 1h^{-1}$ Mpc. Its M_{vir} -richness relation has been calibrated using a variety of methods (Murata et al. 2019; Chiu et al. 2020b,a).

Here we use the public S16A CAMIRA catalogue that contains 998 (263) clusters with $N_{\text{Mem}} \geq 10$ (≥ 20) for $0.19 < z < 0.52$. Among them, 725 clusters have spec- z measurements for their central galaxies. Our CAMIRA sample has a median photo- z bias of $\delta_z \sim -0.0042$ (-0.0036), a scatter of $\sigma_z/(1+z) \sim 0.013$ (0.009), and a $4\text{-}\sigma$ outlier fraction of $\sim 1.4\%$ (0.9%) for the $N_{\text{Mem}} \geq 10$ (≥ 20) clusters. Similar to redMaPPer, only using the photo- z has no impact on any key results. The CAMIRA catalogues shows excellent completeness when compared to X-ray clusters ($\gtrsim 0.8$; see Oguri et al. 2018 § 5.3) or mock galaxy catalogues (> 0.8 for $M_{200c} > 5 \times 10^{13}h^{-1}M_{\odot}$ clusters at $0.3 < z < 0.6$; see Oguri et al. 2018 § 6).

CAMIRA assigns a central galaxy to each cluster without providing a central probability. Oguri et al. (2018) investigated the off-centre distance (R_{off}) distribution using matched X-ray clusters. While the distribution centred at $R_{\text{off}} \approx 0.0$ Mpc, $\sim 30\%$ of the clusters are offset from the X-ray peak with their R_{off} distribution described by a $\sigma = 0.26 \pm 0.04h^{-1}$ Mpc Gaussian component.

We also test the internal S18A, S19A, and S20A CAMIRA catalogues within the S16A footprint. Differences in the data reduction process (e.g., background subtraction, deblending) cause subtle differences in the cluster detection and richness measurements. However, we verify that these updates do not change any conclusions.

4 MEASUREMENTS

Here we briefly introduce the methodologies behind the key measurements used in the Top- N tests: the 1-D surface stellar mass density profiles (μ_* , § 4.1) and the galaxy-galaxy lensing $\Delta\Sigma$ profiles (§ 4.2).

4.1 1-D Surface Mass Density Profiles

Our method for extracting 1-D μ_* profiles is presented in previous work (Huang et al. 2018c,a; Ardila et al. 2021). We refer readers to these papers for full technical details and only provide a brief summary here.

Using the Ellipse isophotal analysis function from IRAF, we extract 1-D i -band surface brightness profiles after aggressively masking out nearby contamination and empirically correcting for the local background. In addition to the mask, the strategy of taking the median of flux density values along the isophote after $3\text{-}\sigma$ clipping makes our 1-D profile robust against the high density of faint objects around massive galaxies (Ardila et al. 2021). With background subtraction, the 1-D profile is stable above ~ 28 mag arcsec⁻², roughly corresponding to $r \sim 100$ kpc for our sample. The inner $\sim 5\text{-}6$ kpc of the profile is smeared by the seeing.

We then convert the i -band surface brightness profile to the μ_* profile using the average i -band M_*/L_* derived from SED fitting after applying corrections for galactic extinction and cosmological dimming. We ignore the M_*/L_* gradient in this work. Low- z massive galaxies have shallow but negative colour gradients (e.g., Huang et al. 2018c; Wang et al. 2019; Montes et al. 2021), which suggests the average M_*/L_* will underestimate the M_* in the central region and overestimate it in the outskirts. However, the lack of clear dependence of colour gradients on M_* (Huang et al. 2018c) suggests this systematic will not influence the conclusions of this work. We release the massive galaxy catalogue along with the 1-D μ_* profiles here: .

4.2 Galaxy-Galaxy Lensing Measurements

The galaxy-galaxy (g-g) lensing measurements done here follow almost exactly those in Speagle et al. (2019) and Huang et al. (2020), which are themselves based on the methodology presented in Leauthaud et al. (2017). This method subtracts lensing signals around a large number of random positions to achieve unbiased measurements (Singh et al. 2017). The equations used to derive the $\Delta\Sigma$ profile are given in

¹⁶ <https://www.slac.stanford.edu/~oguri/cluster/>

Appendix A. Compared to these earlier works, we provide a new recipe for the f_{bias} factor that more accurately accounts for the photo- z dilution effect (see Equation A7)¹⁷.

We measure $\Delta\Sigma$ in 11 physical logarithmic radial bins from 200 kpc to 10 Mpc using the S16A weak lensing shape catalogue (Mandelbaum et al. 2018, 2017). We adopt the frankenz¹⁸ photo- z for source galaxies. For the photo- z quality cut, we use the “basic” cut ($\chi_5^2 < 6$) in Speagle et al. (2019) that removes about 5% of source galaxies with unreliable photo- z . Most of them are at very low redshift so will not contribute to the lensing signals in this work. The lens-source separation criteria are: $z_s - z_L \geq 0.1$ and $z_s > z_L + \sigma_{s,68}$, where $\sigma_{s,68}$ is the 1σ uncertainty of the source photo- z . We confirm that other photo- z quality cuts and slightly different lens-source separation criteria do not affect any results.

We use both jackknife resampling in 40 pre-defined sub-regions and bootstrap resampling with 2000 iterations to estimate the covariance matrix and the uncertainties of the $\Delta\Sigma$ profiles. The two methods lead to fully consistent results.

We use v0.2 of the Python g-g lensing code dsigma¹⁹ to calculate $\Delta\Sigma$ profiles, and we release the $\Delta\Sigma$ measurements for our massive galaxies and clusters here: .

5 HALO MASS PROXIES AND BINS

This section introduces different M_{vir} proxies in our Top- N tests. We broadly grouped these observables into M_* - and richness-based categories. For M_* -based proxies, we include M_* based on the default HSC photometry for extended objects (§ 5.1.1), a series of M_* measures from the 1-D μ_* profiles (§ 5.1.2 & § 5.1.3), and a linear combination of different aperture M_* measures (§ 5.1.4). And for richness-based methods, we include clusters from both redMaPPer and CAMIRA. We also describe our number density bins and show the estimated scatter by comparing to the model described in § 2.2.2.

5.1 Proxies

5.1.1 CModel stellar mass

CModel is the default photometric model for extended objects in both the SDSS and HSC surveys, and will continue to be used in future imaging surveys. CModel attempts to describe the 2-D flux distribution of all extended objects using a combination of an exponential and a de Vacouleurs component (e.g., Bosch et al. 2017). It is an efficient and flexible model and can provide statistically robust colour measurements down to very faint magnitudes (e.g., Huang et al. 2018b). However, CModel does not always provide accurate total flux measurements, especially for massive galaxies whose surface brightness profiles can not be described with the underlying assumptions. In both the SDSS and HSC surveys, CModel photometry significantly underestimates the

flux in the extended outskirts of massive, early-type galaxies (e.g., Bernardi et al. 2013; Huang et al. 2018c). In addition to the intrinsic limitations associated with the assumed model, systematics in critical steps in the data reduction process such as background subtraction and object deblending often interfere with CModel fitting, making it even more challenging to accurately recover the total flux. These issues becomes especially pronounced with deep imaging surveys such as HSC.

Because CModel is the default photometry provided for extended objects in many imaging surveys, it is worth testing using the Top- N methodology. We will quantify the impact of CModel photometry errors on the use of CModel masses as a halo mass proxy. The CModel stellar mass will be labelled as $M_{*,\text{cmoD}}$.

We note that the CModel photometry used here is from HSC S16A and an old version of hscPipe (v4). Although the updated hscPipe includes multiple improvements and modifications, they do not solve the aforementioned issues for bright galaxies. We compare the CModel magnitudes of our sample using S16A, S18A, and S20A data release²⁰. We find no systematic difference between these measurements, hence our results about $M_{*,\text{cmoD}}$ should apply to all HSC data release.

5.1.2 Aperture M_* From 1-D Profiles

In Huang et al. (2018c), we showed that the M_* within a 100 kpc aperture is a better estimate of the “total” M_* of massive galaxies than $M_{*,\text{cmoD}}$. We also demonstrated in Huang et al. (2018a, 2020) that changing the aperture used to measure M_* changes the M_*-M_{vir} relation. Here, we measure M_* in apertures of 10, 30, 50, 75, 100, and 150 kpc in our Top- N tests, and we evaluate how each performs as a proxy for M_{vir} . Throughout the paper, we will label these “aperture M_* ” measurements with $M_{*,10 \text{ kpc}}$, $M_{*,100 \text{ kpc}}$, etc.

In practice, we integrate the 1-D μ_* profile after accounting for the isophotal shape of the galaxy to get the “curve-of-growth” (CoG) of M_* , which describes the relation between the semi-major axis length of an elliptical aperture and the enclosed M_* . Interpolation of the CoG provides the measurements of different aperture M_* . We note that the μ_* profile outside 100 kpc becomes less reliable due to background subtraction issues which affects the accuracy of aperture M_* using larger radii. Given the imaging depth of HSC data, we do not recover substantial amount of M_* beyond 100 kpc. The mean difference between $M_{*,150 \text{ kpc}}$ and $M_{*,100 \text{ kpc}}$ is only ~ 0.02 dex, while the maximum difference is ~ 0.15 dex.

The intrinsic μ_* of massive galaxies certainly extends beyond the HSC surface brightness limit for individual galaxies (e.g., Wang et al. 2019; Zhang et al. 2019b; Montes et al. 2021; Kluge et al. 2021), hence the true total M_* is beyond the reach of our current aperture M_* measurements.

¹⁷ The typical f_{bias} factor value is at the ~ 1 -2% level, and has no impact on the results of this work.

¹⁸ <https://github.com/joshspeagle/frankenz>

¹⁹ <https://github.com/johannesulf/dsigma>

²⁰ The S18A release applies a much improved background subtraction around bright object. But the well preserved low surface brightness envelopes around massive galaxies make object deblending more challenging. This global background correction algorithm was then turned off in the following release S20A.

We attempt to account for the “missing M_* ” by fitting a 1-D Sérsic model to the μ_* profile between 50 and 100 kpc. We use this model to predict the mass beyond the regime in which it can be measured with HSC. This model (assuming it correctly predicts the true profile) confirms that there is little M_* beyond 100 kpc. Using this technique, the predicted average difference between $M_{*,300 \text{ kpc}}$ and $M_{*,100 \text{ kpc}}$ is only ~ 0.05 dex.

Using the CoG, we also measure the radius that contains 50%, 80%, and 90% of the maximum M_* measured by the 1-D profile ($M_{*,\text{max}}$). We denote these radii as R_{50}, R_{80}, R_{90} . The “half-mass”, or effective radius (R_{50}), provides another way to define apertures. For example, we can measure M_* out to $2 \times R_{50}$ or $4 \times R_{50}$. Aperture masses using R_{50} will be labelled as $M_{*,2R_{50}}, M_{*,4R_{50}}$, etc. We briefly explore the result of using these radii-based proxies in Appendix E.

5.1.3 Stellar Mass of the Outer Envelope

In Bradshaw et al. (2020), by studying simulated data the authors noticed that the “*ex situ*” component (the stellar mass that formed outside the halo of the main progenitor) of massive galaxies seems to have a tighter relation with M_{vir} than either the “*in situ*” component or the total M_* . This is also consistent with the modelling results from Huang et al. (2020).

While we cannot separate the *ex situ* component from the M_* distribution directly when using observational data alone, recent simulations and observations suggest that the *ex situ* stars dominate the outskirts of massive galaxies (e.g., Lackner et al. 2012; Rodríguez-Gomez et al. 2016; Pulsoni et al. 2021). It is therefore interesting to test whether the stellar mass in the outer envelope is a useful M_{vir} proxy using the Top- N tests.

Here we simply define this “outer envelope” (or outskirt) M_* as the difference between two aperture M_* . For example, we will use $M_{*,[50,100]}$ to denote the stellar mass between 50 and 100 kpc, and $M_{*,[2,4]R_{50}}$ to denote the stellar mass between $2 \times R_{50}$ and $4 \times R_{50}$. It is not obvious a priori which combination of radial boundaries will provide the best *ex situ* M_* proxy, and so we will explore a range of different definitions of the outer envelope.

Many of the massive galaxies in Huang et al. (2020) are the central galaxies (or the brightest cluster galaxy, BCG) of a galaxy cluster. Their “outer envelope” is also sometimes called the ICL. We avoid this terminology because: 1) the photometric definition of ICL is often ambiguous and arbitrary (e.g., Kluge et al. 2021), and 2) not all massive galaxies in our sample live in clusters (i.e., $M_{\text{vir}} \geq 10^{14} M_{\odot}$). Therefore we prefer to use the more general term – outer envelope – to describe the outer structure of all massive galaxies.

To estimate the outer envelope M_* from the 1-D surface brightness profile, we assume a fixed M_*/L_* value and isophotal shape that represents the inner region. These low- z massive galaxies on average show shallow negative optical colour (hence M_*/L_*) and axis ratio gradients. In our case, the colour gradient means we could slightly over-estimate the outer envelope stellar mass while the axis ratio gradient could lead to an under-estimation. We ignore these minor systematics here and will look into more accurate outer envelope M_* measurement in future work. We have performed

Top- N tests using the luminosity of the outskirts and this does not impact any of our main conclusions.

5.1.4 ASAP model

In Huang et al. (2020), we presented a phenomenological model (ASAP) that connects a linear combination of $M_{*,10 \text{ kpc}}$ and $M_{*,100 \text{ kpc}}$ to the M_{vir} of the host halo of massive galaxies ($M_{*,100 \text{ kpc}} \geq 10^{11.5} M_{\odot}$). We constrained this model using the SMFs for $M_{*,10 \text{ kpc}}$ and $M_{*,100 \text{ kpc}}$ along with the $\Delta\Sigma$ profiles of galaxies in twelve 2-D bins over the $M_{*,100 \text{ kpc}} - M_{*,10 \text{ kpc}}$ plane²¹. In Ardila et al. (2021), we provided an updated ASAP recipe to predict the M_{vir} of a massive galaxy based on its $M_{*,100 \text{ kpc}}$ and $M_{*,10 \text{ kpc}}$:

$$\begin{aligned} \log M_{\text{vir}} = & 3.26 \times (\log M_*^{100} - 11.72) \\ & - 2.46 \times (\log M_*^{10} - 11.34) \\ & + 13.69. \end{aligned} \quad (8)$$

In Huang et al. 2020, we showed that the ASAP model scaling relation summarized by Eq. 8 can predict the *average* M_{vir} of massive halos better than $M_{*,100 \text{ kpc}}$. Throughout this paper, we will use the label $M_{\text{vir, ASAP}}$ to refer to the left-hand side of Eq. 8, and we will investigate the scatter exhibited by individual galaxies for this ASAP prediction.

5.1.5 Richness

We compare these M_* -based proxies to the cluster richness by two popular red-sequence cluster finders: redMaPPer and CAMIRA (introduced in § 3.3.1 and § 3.3.2). Calibrations of the M_{vir} -richness relations suggest that the richness of red-sequence galaxies is a very promising M_{vir} proxy (e.g., Melchior et al. 2017; Murata et al. 2018; McClintock et al. 2019).

Theoretically speaking, richness measurements should outperform M_* -based M_{vir} proxies for massive halos if the majority of their satellites have not merged onto the central galaxies. The log-linear slopes of M_{vir} -richness relations are typically > 1.0 (e.g., Saro et al. 2015; Mantz et al. 2016; Farahi et al. 2016; Simet et al. 2017; Baxter et al. 2018; Melchior et al. 2017; McClintock et al. 2019), while the slopes of $M_{\text{vir}} - M_*$ relations are usually around 0.3-0.5 at $z < 0.5$ (e.g., Rodríguez-Puebla et al. 2017; Tinker et al. 2017; Moster et al. 2018; Kravtsov et al. 2018; Huang et al. 2020). Recent calibrations of M_{vir} -richness relations also suggest modest intrinsic scatter values at the high- M_{vir} end (at $\sim 25\%$ or 0.1-0.2 dex level; e.g., Rykoff et al. 2014; Saro et al. 2015; Simet et al. 2017). Both of these observations support the idea that richness should be a superior M_{vir} proxy to the M_* of the central galaxy. Therefore a Top- N comparison between M_* - and richness-based proxies can help confirm this expectation, or reveal new insights.

For redMaPPer, we denote its richness as $\lambda_{\text{redMaPPer}}$. For CAMIRA, we use N_{CAMIRA} to represent its richness measurement.

²¹ Note that Huang et al. (2020) used the notation $M_{*,\text{max}}$ to refer to $M_{*,100 \text{ kpc}}$.

Property	Bin 1	Bin 2	Bin 3	Bin 4
N_{Sample}	50	197	662	1165
$\log_{10} M_{\text{vir, MDPL2}}$	[14.66, 15.55]	[14.38, 14.66]	[14.08, 14.38]	[13.86, 14.08]
$n(> M_{\text{vir}})$	5.11×10^{-7}	2.52×10^{-6}	9.29×10^{-6}	2.12×10^{-5}
$\lambda_{\text{redMaPPer}}$	[35, 120]	[20, 35]	[10, 20]	[6, 10]
$\sigma_{M_{\text{vir}}}$	0.27 ± 0.02	0.38 ± 0.02	0.39 ± 0.02	0.58 ± 0.02
N_{CAMIRA}	[35, 75]	[21, 35]	[12, 21]	
$\sigma_{M_{\text{vir}}}$	0.30 ± 0.03	0.36 ± 0.01	0.50 ± 0.02	
$\log_{10} M_{\star, \text{CModel}}$	[11.88, 12.19]	[11.77, 11.88]	[11.67, 11.77]	[11.60, 11.67]
$\sigma_{M_{\text{vir}}}$	0.60 ± 0.04	0.64 ± 0.04	0.87 ± 0.06	0.82 ± 0.03
$\log_{10} M_{\star, 30 \text{ kpc}}$	[11.77, 12.00]	[11.69, 11.77]	[11.61, 11.70]	[11.53, 11.61]
$\sigma_{M_{\text{vir}}}$	0.52 ± 0.04	0.57 ± 0.03	0.61 ± 0.03	0.61 ± 0.02
$\log_{10} M_{\star, 50 \text{ kpc}}$	[11.86, 12.10]	[11.76, 11.86]	[11.66, 11.76]	[11.58, 11.66]
$\sigma_{M_{\text{vir}}}$	0.46 ± 0.04	0.53 ± 0.03	0.59 ± 0.02	0.61 ± 0.02
$\log_{10} M_{\star, 100 \text{ kpc}}$	[11.93, 12.18]	[11.83, 11.93]	[11.71, 11.83]	[11.63, 11.71]
$\sigma_{M_{\text{vir}}}$	0.38 ± 0.02	0.51 ± 0.02	0.56 ± 0.02	0.60 ± 0.02
$\log_{10} M_{\star, 150 \text{ kpc}}$	[11.96, 12.21]	[11.85, 11.96]	[11.73, 11.85]	[11.64, 11.73]
$\sigma_{M_{\text{vir}}}$	0.37 ± 0.03	0.47 ± 0.03	0.56 ± 0.02	0.57 ± 0.03
$\log_{10} M_{\star, [50, 100]}$	[11.20, 11.60]	[11.00, 11.20]	[10.80, 11.00]	[10.63, 11.00]
$\sigma_{M_{\text{vir}}}$	0.36 ± 0.02	0.43 ± 0.02	0.44 ± 0.02	0.48 ± 0.02
$\log_{10} M_{\text{vir, ASAP}}$	[14.45, 15.28]	[14.09, 14.45]	[13.80, 14.11]	[13.60, 13.80]
$\sigma_{M_{\text{vir}}}$	0.38 ± 0.03	0.44 ± 0.02	0.48 ± 0.02	0.56 ± 0.02

Table 1. Summary of results from the Top- N test results in four number density bins. The first three rows summarize the basic properties of each bin. N_{sample} is the number of HSC galaxies in each bin. $\log_{10} M_{\text{vir, MDPL2}}$ shows the corresponding halo mass range in this number density bin based on the MDPL2 simulation. This is the M_{vir} range for an ideal (zero scatter) Top- N selection. $n(> M_{\text{vir}})$ is the volume number density of halos above the lower- M_{vir} threshold. Subsequent rows contain the key results for different halo mass proxies. The first row shows the range of the observed properties in the four bins. The second row shows the best-fit scatter of M_{vir} at fixed observable ($\sigma_{\mathcal{M}|\mathcal{O}}$) of M_{vir} in each bin along with its uncertainty. For a complete summary table of all the properties we tested, please see this [Jupyter notebook](#) 

5.2 Number Density Bins

To perform the Top- N tests using the previously mentioned proxies, we design four number density bins based on the richness of HSC **redMaPPer** clusters ($\lambda_{\text{redMaPPer}}$). These four bins correspond to the $\lambda_{\text{redMaPPer}}$ ranges of [35, 100], [20, 35], [10, 20], [6, 10] and have 50, 197, 662, & 1165 objects in each bin. We refer to these bins as Bin 1 (richest clusters or highest average M_{vir}) through to Bin 4 (least rich clusters or lowest average M_{vir}). The total number (2074) of objects is slightly smaller than the number of $\log(M_{\star, 100 \text{ kpc}}/M_{\odot}) \geq 11.6$ galaxies (2247), which defines a M_{\star} -complete sample. The area of the **S16A** data means that we do not have enough massive clusters to sample the high $\lambda_{\text{redMaPPer}}$ range. Hence, Bin 1 covers a fairly wide richness range.

Figure 3 illustrates how these bins in $\lambda_{\text{redMaPPer}}$ correspond to bins in number density (top-left panel) and M_{vir} using the HMF from MDPL2 (top-right panel). Assuming an ideal tracer with zero scatter, Bin 1, 2, & 3 are well above the conventional standard for “galaxy cluster” ($\log_{10} M_{\text{vir}} \geq 14.0$) while the mean M_{vir} of Bin 4 is on the boundary between a cluster and a “massive group”. In reality, the M_{vir} distributions will shift to lower values due to the scatter of the M_{vir} – observable relation.

The $N_{\text{Mem}} > 10$ threshold for the **CAMIRA** clusters means it does not have enough objects for Bin 4, therefore we only consider the first three bins. Similarly, for the SDSS **redMaPPer** catalogue, we only include Bins 1 & 2, and we note that the richness range for Bin 4 is challenging even for deep HSC images. We must therefore take the results for **redMaPPer** in Bin 4 with some caution.

We were unable to measure M_{\star} for $\sim 9\%$ of galaxies due to excessive blending which prevented the extraction of a 1-D profile. This reduces the effective area and volume of this sample. We do not correct for this when selecting the Top- N galaxies. The effect of this can only reduce the $\Delta\Sigma$ amplitude, but we verify it does not affect our results. We summarize the key properties of these four bins in Table 1.

6 RESULTS

In this section we present our main results. We begin in § 6.1 with a qualitative evaluation of how satellite contamination impacts measurements of $\Delta\Sigma$ for M_{\star} -selected samples. We then summarize the key findings from the Top- N tests in § 6.2. First, we show how $\sigma_{\mathcal{M}|\mathcal{O}}$ scales with number density for samples selected according to different choices of aperture mass (§ 6.2.1) and outskirts mass (§ 6.2.2). We also compare the $\Delta\Sigma$ profiles of samples selected by $M_{\star, 100 \text{ kpc}}$ relative to samples selected by $M_{\star, [50, 100]}$ (§ 6.2.2) and $M_{\star, \text{cmod}}$ (§ 6.2.3). We summarize results related to $M_{\text{vir, ASAP}}$ in § 6.2.4. In § 6.2.5, we examine the Top- N results of richness-based cluster finders. We then show the behavior of $\sigma_{\mathcal{M}|\mathcal{O}}$ for a series of different M_{vir} proxies (§ 6.2.6). Finally, in § 6.3, we compare the *shape* of the $\Delta\Sigma$ profiles of M_{\star} - and richness-selected massive halos, and we assess the level of consistency of these profiles with theoretical expectations based on simulated halos that have been selected based on true halo mass. The results shown in § 6 focus on the most interesting cases, but the Top- N results for all proxies are made publicly available here: [GitHub](#) 

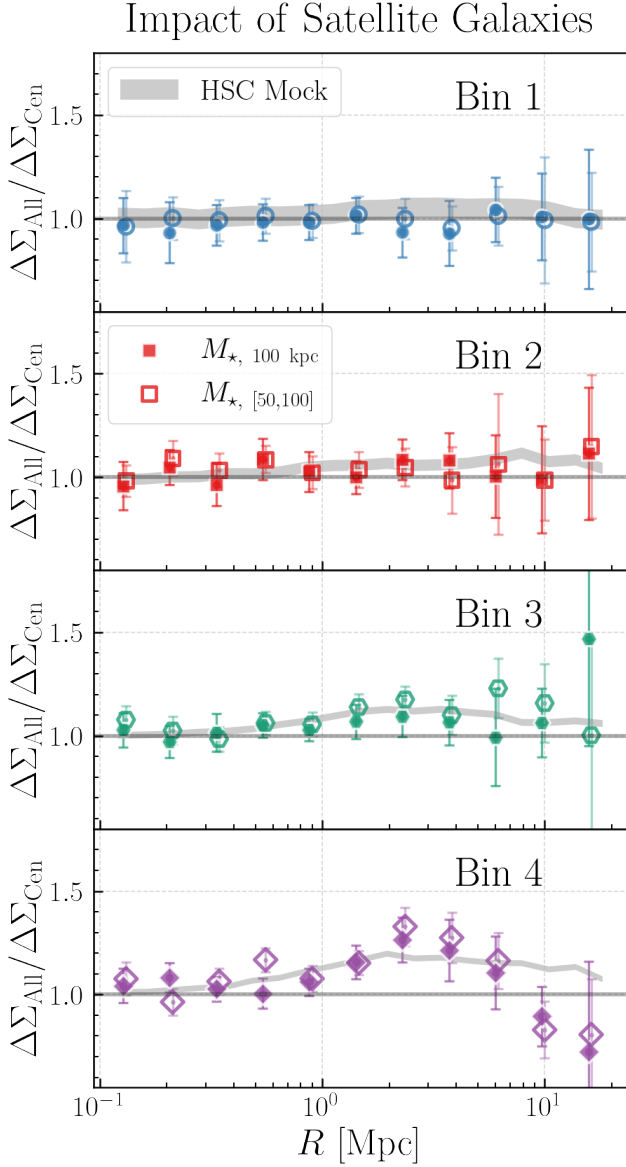


Figure 4. Ratio of $\Delta\Sigma$ profiles for all galaxies (central & satellite; $\Delta\Sigma_{\text{All}}$) compared to central galaxies only ($\Delta\Sigma_{\text{Cen}}$). Grey shaded regions show results from our fiducial HSC mock catalogue. Data points show results from HSC data where satellites are removed using a simple cylinder based technique. Solid symbols correspond to galaxies selected by $M_{\star,100 \text{ kpc}}$. Open symbols correspond to galaxies selected by $M_{\star,[50,100]}$ (data points are slightly offset along the X-axis). Satellites have almost no impact in the first two bins (corresponding to $M_{\star,100 \text{ kpc}} > 10^{11.8} M_{\odot}$ and $M_{\star,[50,100]} > 10^{11.1} M_{\odot}$). The HSC mock suggests that satellites have a maximum impact of $\sim 15\%$ ($\sim 20\%$) in Bin 3 (4) at $R \sim 2-4$ Mpc. The `Jupyter` notebook for reproducing this figure can be found here: [🔗](#).

6.1 Impact of Satellite Contamination on $\Delta\Sigma$

Although satellite galaxies only make up a small fraction of $\log(M_{\star,100 \text{ kpc}}/M_{\odot}) > 11.5$ galaxies (e.g., Reid et al. 2014; Saito et al. 2016; van Uitert et al. 2016; Huang et al. 2020), they could affect our evaluation of the performance of M_{\star} -based M_{vir} proxies. The $\Delta\Sigma$ profiles of satellite galaxies show a unique “bump”-like features at around $R \sim 1$ Mpc (e.g., Li

et al. 2014, 2016a; Sifón et al. 2015, 2018) which corresponds to the offset profile of the main parent halo. Here, we evaluate the impact of satellites on M_{\star} -based proxies and $\sigma_{M_{\text{vir}}}$ estimates by comparing the $\Delta\Sigma$ profiles of a pure central sample to that of a central+satellites sample in the same Top- N bin. We use two methods: One based on a realistic mock catalogue with central/satellite assignments and one using satellites identification in real HSC data.

We use a mock catalogue (see Appendix C, DiMartino et al in prep) that was specifically designed to have realistic values for both $\sigma_{M_{\text{vir}}}$ and for the satellite fractions of massive galaxies. This mock was constrained using the SMF and the two-point correlation functions (2PCF) of HSC massive galaxies. Using this mock, we select the pure central and the central+satellites samples based on the model M_{\star} and the four number density bins defined in § 5.2. In the four Top- N bins, the HSC mock yields satellite fractions of [5.0%, 6.9%, 8.9%, & 10.0%], which are consistent with the expectation of low satellite fractions among massive galaxies.

Next, we attempt to classify massive satellite galaxies in our HSC sample directly by recursively identifying less massive galaxies around more massive ones. We start with the galaxy with the largest M_{\star} value and label all the other galaxies within a cylindrical region with a 1.0 physical Mpc radius in projection and a 30 comoving Mpc length in the line-of-sight (LOS) direction as satellites. We then turn to the next most massive galaxy and repeat this exercise. Using this simple strategy, the observed satellite fractions are [0.0%, 3.6%, 4.7%, & 8.8%] in the four Top- N bins. These observed fraction values are slightly lower than when we use the mock catalogue but these differences are not large enough to affect any of our results. Small variations of the radius and length of the cylinder do not change any results.

Figure 4 shows the ratio of $\Delta\Sigma$ profiles of the central+satellite ($\Delta\Sigma_{\text{All}}$) and the pure central ($\Delta\Sigma_{\text{Cen}}$) samples using both the mock catalogue and the HSC data. For HSC data, we test both the $M_{\star,100 \text{ kpc}}$ and the $M_{\star,[50,100]}$ sample. In Bin 1 & 2, the satellite fractions are low enough that there is no discernible impact on $\Delta\Sigma$. In Bin 3 & 4, massive satellites lead to a small enhancement in the $\Delta\Sigma$ profile at $R > 500$ kpc. In Bin 3 (4), the mock catalogue predicts a maximum $\sim 10\%$ ($\sim 20\%$) enhancement at $R \sim 2-3$ Mpc. Both M_{\star} -based proxies demonstrate behaviors that are statistically consistent with the mock catalogue despite our naive central/satellite classification scheme. The details of the fiducial mock catalogue do not affect this conclusion. Even the simple $\alpha = 1$ model with varying scatter values used for estimating $\sigma_{M_{\text{vir}}}$ can also lead to the same results²²

In the rest of this paper, we include massive satellite galaxies both in our HSC samples and in the models that we draw from the mock catalogues. Due to the low satellite fraction, the inclusion of satellite galaxies does not affect any of our conclusions²³. The impact of satellites is further discussed in Appendix D.

²² See the additional figure in this `Jupyter` notebook: [🔗](#).

²³ The removal of massive satellite candidates usually only leads to 0.01-0.02 dex variation in $\sigma_{M_{\text{vir}}}$ values.

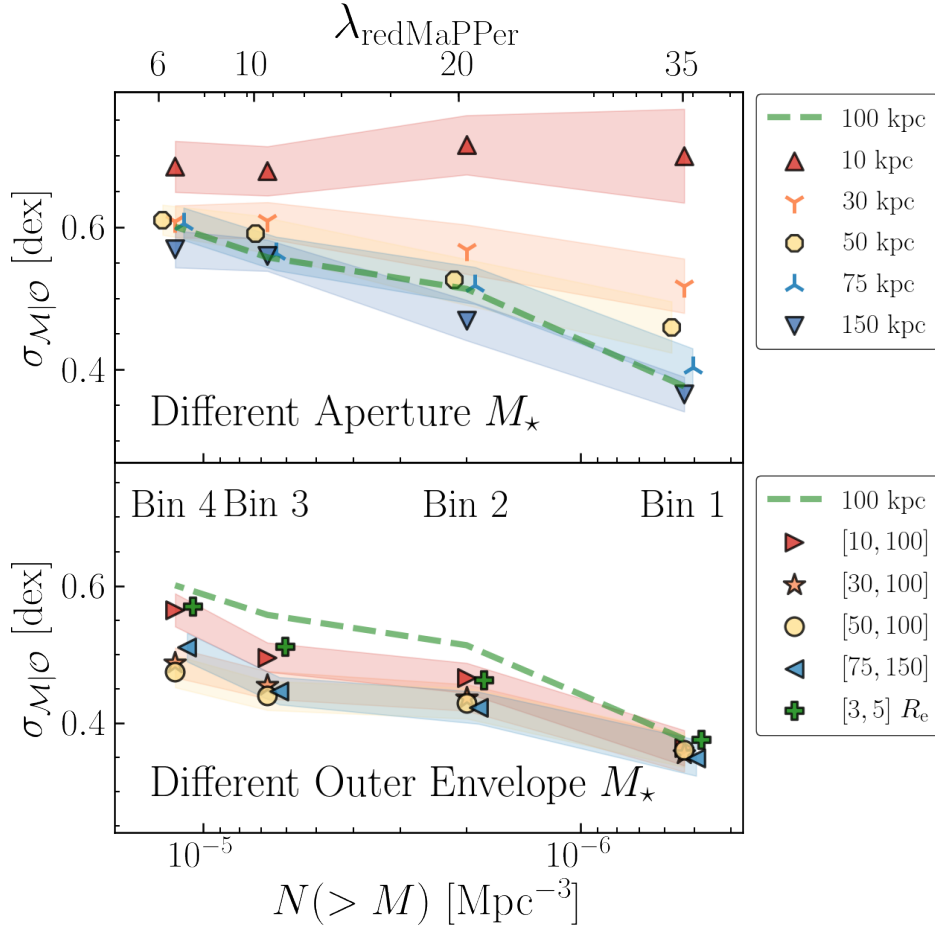


Figure 5. Scatter in M_{vir} at fixed observable versus number density bins. Aperture masses (the mass within the indicated radius) are shown in the top panel and and outskirts M_* is shown in the bottom panel. The Y-axis shows the best-fit values of $\sigma_{M|O}$ (data points) with uncertainties (shaded regions). The X-axis labels on the top indicate the HSC S16A redMaPPer richness thresholds corresponding to the four number density bins. The $M_{*,100 \text{ kpc}}$ trend (green dashed-line) is used as a reference. We also slightly shift the symbols along the X-axis for visibility. This figure shows that the outer mass is an excellent M_{vir} proxy. In contrast, inner stellar mass is a very poor tracer of present day M_{vir} . The *Jupyter* notebook for reproducing this figure can be found here: [🔗](#).

6.2 Amplitude of $\Delta\Sigma$ and Inferred $\sigma_{M_{\text{vir}}}$ Values

We now present the Top- N results with a focus on the overall amplitude of $\Delta\Sigma$ for the M_{vir} proxies introduced in § 5. We first describe the three proxies which yield the most interesting results: aperture M_* , outskirts M_* , and the $M_{*,\text{comod}}$. Then we compare all the M_{vir} proxies and present the inferred $\sigma_{M_{\text{vir}}}$ values.

6.2.1 Aperture Stellar Masses

We start by exploring the performance of aperture M_* . The upper panel of Figure 5 shows the $\sigma_{M_{\text{vir}}}$ for various apertures. It is clear that the $\sigma_{M_{\text{vir}}}$ decreases with increasing aperture size. This decrease is particularly obvious in Bins 1 & 2 (the most massive halos). In Bin 1 (2), $\sigma_{M_{\text{vir}}}$ decreases from 0.70 (0.72) dex for $M_{*,10 \text{ kpc}}$, to 0.52 (0.57) dex for $M_{*,30 \text{ kpc}}$, to 0.38 (0.51) dex for $M_{*,100 \text{ kpc}}$. Figure 5 shows that the aperture size used to estimate M_* has significant impact on how well different samples trace M_{vir} . More importantly, Figure 5 shows that the inner regions of massive galaxies (10 to 30 kpc) is a very poor tracer of present day

halo mass. This is consistent with the SHMR constraints in Golden-Marx & Miller (2019) where the authors focused more on the slope of the SHMR using different aperture M_* (see their Figure 2). Using a sample of massive BCGs at $0.0 < z < 0.3$ in $M_{\text{vir}} > 10^{14.0} M_{\odot}$ clusters, the authors find the slope of the SHMR increases from $\alpha \sim 0.1$ for $M_{*,10 \text{ kpc}}$ to $\alpha \sim 0.4$ for $M_{*,100 \text{ kpc}}$. Assuming a constant $\sigma_{M_*} \sim 0.2$ dex value for the SHMR, such variation of slopes correspond to $\sigma_{M_{\text{vir}}} \sim 0.6$ dex for $M_{*,10 \text{ kpc}}$ and ~ 0.4 dex for $M_{*,100 \text{ kpc}}$, broadly consistent with the Top- N results in Bin 1.

Further enlarging the aperture size to 150 kpc does not result in much improved $\sigma_{M_{\text{vir}}}$ in any of the bins (see Table 1). It is unclear whether the lack of improvement with apertures larger than 100 kpc reflects the intrinsic limitation of large aperture M_* as a M_{vir} proxy or the statistical uncertainty of the current imaging data in the low surface brightness regime. In the remainder of this paper, we use $M_{*,100 \text{ kpc}}$ as the benchmark against which we will compare other M_{vir} proxies. In the Appendix E, we also explore other definitions of aperture M_* based on R_{50} but do not find any that has better performance.

6.2.2 Outer Envelope Mass

Figure 5 suggests that removing the inner portion of the galaxy and using only the outskirts could yield an improved M_{vir} proxy. From hydro-simulations or semi-empirical modelling of massive galaxy formation, we know that the accreted stellar component (or the *ex situ* stars) dominates the M_* budget, especially in the outskirts (e.g., Rodriguez-Gomez et al. 2016). We will discuss this further in § 7.3, but if the *ex situ* stars have a tighter relation with M_{vir} , we should expect outskirts M_* to be a better M_{vir} proxy. We test this hypothesis here.

Since there is no preference a priori for an optimal definition of what constitutes the “outskirts” of a massive galaxy, we empirically study a number of different values. The bottom panel of Figure 5 shows one of the main findings of this paper. Namely, **the M_* in the outskirts of massive galaxies is an excellent proxy of halo mass, and largely outperforms any form of aperture mass, especially relative to masses defined by the inner regions of the galaxy.** Figure 5 shows that $M_{*,[50,100]}$ is the best M_{vir} proxy among the outer masses that we tested, and that $M_{*,[30,100]}$ also displays comparable performance. This figure also helps inform our understanding of the trade-off between retaining enough light to achieve a high S/N measurement, while at the same time removing the *in situ* stars that lie preferentially within the inner region. For example, in Bins 2, 3, and 4, we can see that the performance of $M_{*,[10,100]}$ is slightly worse than either $M_{*,[30,100]}$ or $M_{*,[50,100]}$. This result taken together with the results shown in the top panel of Figure 5 indicates that the stellar mass located within the inner 10-20 kpc does not correlate well with M_{vir} , and so should be excluded. Additionally, we can see from Figure 5 that using outskirts masses that extend beyond 100 kpc (e.g., $M_{*,[75,150]}$) does not improve the performance of the halo mass proxy.

We have also explored outskirts M_* defined using R_{50} , but fail to find one whose performance is as good as $M_{*,[50,100]}$. These alternate definitions are discussed in Appendix E.

We now compare the $\Delta\Sigma$ profiles of the $M_{*,[50,100]}$ Top- N samples to that of $M_{*,100 \text{ kpc}}$ in Figure 6. In general, the overall amplitudes confirm that $M_{*,[50,100]}$ performs better than $M_{*,100 \text{ kpc}}$ as a M_{vir} proxy. With the exception of Bin 1, the $\Delta\Sigma$ profiles of the $M_{*,[50,100]}$ samples show statistically higher amplitudes at $R < 2$ Mpc than the $M_{*,100 \text{ kpc}}$ ones. The difference is more pronounced for lower mass bins. The average $\Delta\Sigma_{100 \text{ kpc}}/\Delta\Sigma_{[50,100]}$ ratios are $[0.90 \pm 0.17, 0.85 \pm 0.13, 0.82 \pm 0.09, 0.80 \pm 0.09]$ for Bin 1-4. As a result, $M_{*,[50,100]}$ also has lower $\sigma_{M_{\text{vir}}}$ values than $M_{*,100 \text{ kpc}}$: $\sigma_{M_{\text{vir}}} = [0.36, 0.43, 0.44, 0.48]$ for $M_{*,[50,100]}$ and $\sigma_{M_{\text{vir}}} = [0.38, 0.51, 0.56, 0.60]$ for $M_{*,100 \text{ kpc}}$ in Bin 1-4. The right column of Figure 6 shows the M_{vir} distributions of these two samples. The $M_{*,[50,100]}$ samples have higher mean M_{vir} ($\log_{10} M_{\text{vir}} = [14.39, 14.04, 13.76, 13.52]$) values compared to $M_{*,100 \text{ kpc}}$ samples ($\log_{10} M_{\text{vir}} = [14.36, 13.86, 13.54, 13.32]$) too. These conclusions also qualitatively apply to $M_{*,[50,150]}$, and do not change if we switch $M_{*,100 \text{ kpc}}$ with $M_{*,150 \text{ kpc}}$, or $M_{*,\text{max}}$.

We emphasize that both $M_{*,100 \text{ kpc}}$ and $M_{*,[50,100]}$ based selections yield $\Delta\Sigma$ profiles that are statistically consistent with predictions based on our simple “pure scatter” model (§ 2.2.2). We can qualitatively confirm this conclusion using the

left columns of Figure 6 and Figure 6 as there is no systematic deviations from the predicted $\Delta\Sigma$ profiles (grey shaded regions). As for goodness-of-fit statistics, the χ^2 values of $M_{*,100 \text{ kpc}}$ samples are $[6.47, 9.56, 14.92, 9.60]^{24}$ and the values for $M_{*,[50,100]}$ samples are $[6.15, 11.23, 11.94, 5.99]$. This conclusion is not only true for $M_{*,[50,100]}$ and $M_{*,100 \text{ kpc}}$, but also valid for the majority of M_* -based M_{vir} proxies with similar $\sigma_{M_{\text{vir}}}$ values. Removing candidates of massive satellites using the method described in § 6.1 can lead to marginal improvements of χ^2 values, but does not change any conclusions.

It is important to remember that a log-normal M_{vir} -observable relation with *just* a Gaussian scatter can already describe the $\Delta\Sigma$ profiles of some promising M_* -based M_{vir} proxies at the current S/N. We will come back to this point when comparing with Top- N results of richness-based clusters (§ 6.3). And we discuss the origin and the implications of this result in § 7.3.

6.2.3 The Case of $M_{*,\text{cmod}}$

Since CModel is still widely used for galaxy luminosities and masses, it is of great interest to evaluate its performance as M_{vir} proxy.

Figure 7 compares the Top- N results of the benchmark aperture stellar mass $M_{*,100 \text{ kpc}}$ to that of $M_{*,\text{cmod}}$. The $\Delta\Sigma$ profiles of $M_{*,\text{cmod}}$ selected samples have significantly lower lensing amplitudes (on average by 20-50%) in all four bins over the entire radial range (left and middle panels of Figure 7). The best-fit $\sigma_{M_{\text{vir}}}$ values for the $M_{*,\text{cmod}}$ samples are $[0.61, 0.71, 0.87, 0.85]$ and are much worse than those of the $M_{*,100 \text{ kpc}}$ samples. Such large $\sigma_{M_{\text{vir}}}$ values also mean significantly lower M_{vir} values. As shown in the right panels of Figure 7, the mean M_{vir} of the $M_{*,\text{cmod}}$ Top- N samples are $[0.52, 0.17, 0.79, 0.53]$ dex lower than that of the $M_{*, \text{kpc}}$ ones. All these results make it obvious that CModel is not a good M_{vir} proxy.

The χ^2 values of the $M_{*,\text{cmod}}$ -based $\Delta\Sigma$ profiles are $[7.88, 8.76, 15.27, 15.87]$. These values are statistically similar to those of $M_{*,100 \text{ kpc}}$ samples in Bin 1-3, indicating they are still broadly consistent with the “pure scatter” model. Note that the $\sigma_{M_{\text{vir}}}$ values for Bin 2-4 are so large that it includes halos with $\log_{10} M_{\text{vir}} \leq 12.0$ which are unlikely to host real massive galaxies with $\log_{10}(M_{*,\text{CModel}}/M_{\odot}) \geq 11.0$. Given this, we suggest not taking the $\sigma_{M_{\text{vir}}}$ values for $M_{*,\text{cmod}}$ too literally. Instead, the main point here is that M_* based on CModel photometry is not a promising M_{vir} proxy and the $\sigma_{M_{\text{vir}}}$ values associated with $M_{*,\text{cmod}}$ are much larger than other proxies.

²⁴ Each $\Delta\Sigma$ profile has 11 data points and the scatter of $\log_{10} M_{\text{vir}}$ is the only “free parameter” in our model. Therefore one can roughly estimate a reduced χ^2 value using degree-of-freedom $\nu = 10$. However, given the small sample size in our Top- N bins, the simple resampling method used to estimate covariance matrix, we do not recommend to take the reduced χ^2 values too literally. Relative comparison is a more meaningful way to use these χ^2 values.

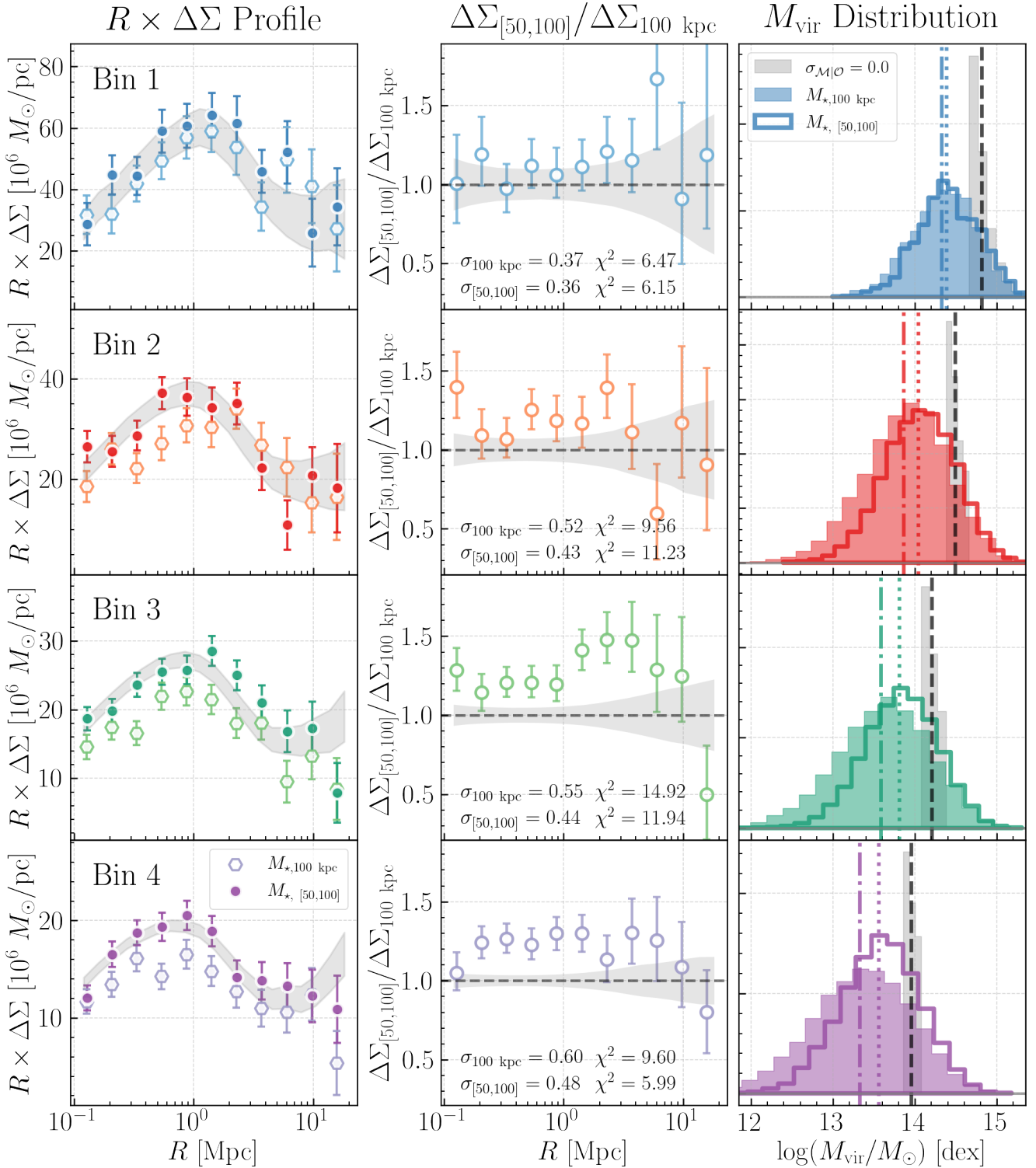


Figure 6. Comparison of the Top- N results for $M_{*,100 \text{ kpc}}$ and $M_{*,[50,100]}$. Rows correspond to number density bins (see § 5.2). **Left** column: $R \times \Delta\Sigma$ profiles of $M_{*,[50,100]}$ -selected (circles) and $M_{*,100 \text{ kpc}}$ -selected (hexagons) samples. Grey shaded regions show the best-fit profiles and their associated uncertainties. The overall amplitude of $\Delta\Sigma$ profiles are similar in Bin 1. But $M_{*,[50,100]}$ samples have consistently higher lensing amplitudes in the three other bins compared to the $M_{*,100 \text{ kpc}}$ samples. **Middle** column: ratio of $\Delta\Sigma$ profiles. Samples selected by $M_{*,[50,100]}$ in Bin 2-4 show $\sim 20\text{--}30\%$ higher $\Delta\Sigma$ amplitudes at $R < 2$ Mpc than the $M_{*,100 \text{ kpc}}$ samples. **Right** column: inferred M_{vir} distributions for the two samples using the model described in § 2.2.2. Grey histograms indicate the M_{vir} distributions of an ideal tracer with $\sigma_{M|O} = 0$. Vertical lines indicate the average M_{vir} . For Bins 2-4, $M_{*,[50,100]}$ yield an average halo mass that is ~ 0.2 dex higher than for $M_{*,100 \text{ kpc}}$. The *Jupyter* notebook for reproducing this figure can be found here: [🔗](#)

6.2.4 The Case of $M_{\text{vir, ASAP}}$

As mentioned in § 5.1.4, in Huang et al. (2020), we proposed the ASAP model that can use a linear combination of $M_{\star, 10 \text{ kpc}}$ and $M_{\star, 100 \text{ kpc}}$ (or $M_{\star, \text{max}}$) to improve the prediction of M_{vir} for massive galaxies. Here we briefly summarize the results.

In Figure 8, we compare the $\sigma_{M_{\text{vir}}}$ trends with number density for a few important M_{\star} -based M_{vir} proxies including the $M_{\text{vir, ASAP}}$. As expected, $M_{\text{vir, ASAP}}$ shows improvement in $\sigma_{M_{\text{vir}}}$ values when compared to large aperture M_{\star} such as $M_{\star, 100 \text{ kpc}}$. Meanwhile, in Bin 2-4, outskirts M_{\star} like $M_{\star, [50, 100]}$ still displays small advantage in $\sigma_{M_{\text{vir}}}$ over $M_{\text{vir, ASAP}}$, especially in Bin 4. We notice that the $\sigma_{M_{\text{vir}}} = [0.38 \pm 0.03, 0.44 \pm 0.02, 0.48 \pm 0.02, 0.56 \pm 0.02]$ of $M_{\text{vir, ASAP}}$ are very similar to the results of $M_{\star, [10, 100]}$: $\sigma_{M_{\text{vir}}} = [0.36 \pm 0.03, 0.47 \pm 0.02, 0.50 \pm 0.02, 0.56 \pm 0.02]$. This shows that the ASAP model, which uses a linear combination of $M_{\star, 10 \text{ kpc}}$ and $M_{\star, 100 \text{ kpc}}$, has minimal improvements over the one which just uses the difference between those masses. This, along with the fact that the preferred definition of outskirts is between 50 and 100 kpc, strongly suggests that it is very difficult to gain additional information about M_{vir} using the inner regions ($R < 30 \text{ kpc}$) of massive galaxies.

We should note that the $\Delta\Sigma$ profiles of $M_{\text{vir, ASAP}}$ samples are also well described by the simple “pure scatter” model.

6.2.5 Comparison with Richness-based Proxies

We now compare the M_{\star} -based proxies with richness-based ones. Figure 8 compares the number density– $\sigma_{M_{\text{vir}}}$ trends for a representative set of M_{vir} proxies in this work, including $M_{\star, \text{cmod}}$ (default survey photometry), $M_{\star, 100 \text{ kpc}}$ (large aperture M_{\star}), $M_{\star, [50, 100]}$ (the best outer envelope mass), $M_{\text{vir, ASAP}}$ (a combination of the inner and large aperture mass), and $\lambda_{\text{redM, HSC}}$ and $\lambda_{\text{CAMIRA, HSC}}$ (richness of red-sequence galaxies). We summarize the $\sigma_{M_{\text{vir}}}$ values, along with the precise cuts that define the bins for each M_{vir} proxy, in Table 1. We remind readers that the M_{\star} -based samples and the two richness-based cluster catalogues are independently selected from the HSC S16A dataset. While there is a considerable overlap, not all the M_{\star} -selected massive galaxies in the Top- N samples belong to identified clusters, and not all cluster centrals are included in the parent sample of massive galaxies. We will briefly discuss this in § 7.5.

For M_{\star} -based proxies, we *do not exclude* massive satellite galaxies from both observations and mock catalogues. For richness-selected clusters, we use a central-only mock catalogue to calculate their $\Delta\Sigma$ profiles and estimate their $\sigma_{M_{\text{vir}}}$ values. This assumes the cluster finders identify the correct central galaxies, which is not always the case, but as we showed in §6.1, satellite contamination is not likely to affect any of the key results shown here.

Judged solely by the $\sigma_{M_{\text{vir}}}$ values, the richness of red-sequence galaxies is an excellent M_{vir} proxy for massive halos. Both richness-based cluster finders show lower $\sigma_{M_{\text{vir}}}$ values in Bin 1 & 2 than any of the M_{\star} -based M_{vir} proxies: $\sigma_{M_{\text{vir}}} = [0.27, 0.38]$ for HSC redMaPPer clusters (red diamonds in figure 8), $[0.30, 0.36]$ dex for the CAMIRA S16A catalogues (red open squares). These two bins have redMaPPer $\lambda > 20$ and CAMIRA $N_{\text{mem}} > 21$, corresponding to

$M_{\text{vir}} \geq 2 \times 10^{14} M_{\odot}$. In this M_{vir} range for typical galaxy clusters, such low values of $\sigma_{M_{\text{vir}}}$ computed with our simple model qualitatively agree with previous calibrations (e.g., Murata et al. 2018, 2019).

The $\sigma_{M_{\text{vir}}}$ increases slightly for richness-based proxies towards the lower- M_{vir} end. The $\sigma_{M_{\text{vir}}}$ values for HSC redMaPPer clusters are $[0.44, 0.62]$ dex in Bin 3 & 4 and 0.52 dex in Bin 3 for CAMIRA clusters. This trend with richness (or number density) is also qualitatively consistent with the results from Murata et al. (2018, 2019). Taken at face value, the performance of the two richness-based proxies becomes comparable with the outskirts M_{\star} in Bin 3 & 4. Note that the λ_{HSC} range in Bin 4 ($6 \leq \lambda_{\text{HSC}} < 10$) is very low and is challenging for any richness-based cluster finder. More importantly, we underscore the fact that the shapes of the $\Delta\Sigma$ profiles of richness-selected clusters show systematic deviations from the pure scatter model. This means that the inferred $\sigma_{M_{\text{vir}}}$ values for richness based selections could be underestimated. We will return to this question in detail in § 6.3.

6.2.6 Summary of $\sigma_{M_{\text{vir}}}$ Trends for Different M_{vir} Proxies

We briefly summarize the number density - $\sigma_{M_{\text{vir}}}$ trends for different M_{vir} proxies. Note that not all $\Delta\Sigma$ profiles are equally well described by the “pure scatter” model, but we only focus on the best-fit $\sigma_{M_{\text{vir}}}$ values here.

- The outer mass of massive galaxies is a promising M_{vir} proxy. The $M_{\star, [50, 100]}$ mass out-performs large aperture M_{\star} such as $M_{\star, 100 \text{ kpc}}$.
- Outer stellar mass is a competitive proxy with richness and may outperform richness in the low- M_{vir} regime (e.g. $\lambda \leq 20$, or $N_{\text{Mem}} \leq 20$).
- Galaxy inner mass ($r < 10\text{-}30 \text{ kpc}$) is a poor tracer of present day halo mass. For this reason, only the outskirts M_{\star} that excludes the inner 30 kpc demonstrates clear improvement over large aperture M_{\star} (see Figure 5).
- Empirical model such as ASAP that attempt to take advantages of more than one aperture M_{\star} do show smaller $\sigma_{M_{\text{vir}}}$ values compared to single large aperture M_{\star} . However, the decision to use $M_{\star, 10 \text{ kpc}}$ (which we now know only adds noise) in Huang et al. (2020) limits the level of improvement.
- Stellar masses derived from default survey photometry pipelines are likely to yield poor M_{vir} proxies as $M_{\star, \text{cmod}}$ has the worst overall performance. This not only applies to CModel, but could be also true for the small aperture photometry, SourceExtractor MAG_AUTO, or even single-Sérsic 2-D models.

6.3 Information Contained in the the Shape of $\Delta\Sigma$

In the previous section we focused on the overall amplitude of $\Delta\Sigma$ and the inferred $\sigma_{M_{\text{vir}}}$ values. Now we consider the shape of the $\Delta\Sigma$ profiles. We focus in particular on two questions:

- Are there differences in the shape of the $\Delta\Sigma$ profiles for samples selected by M_{\star} -based M_{vir} proxies and the clusters selected by richness?

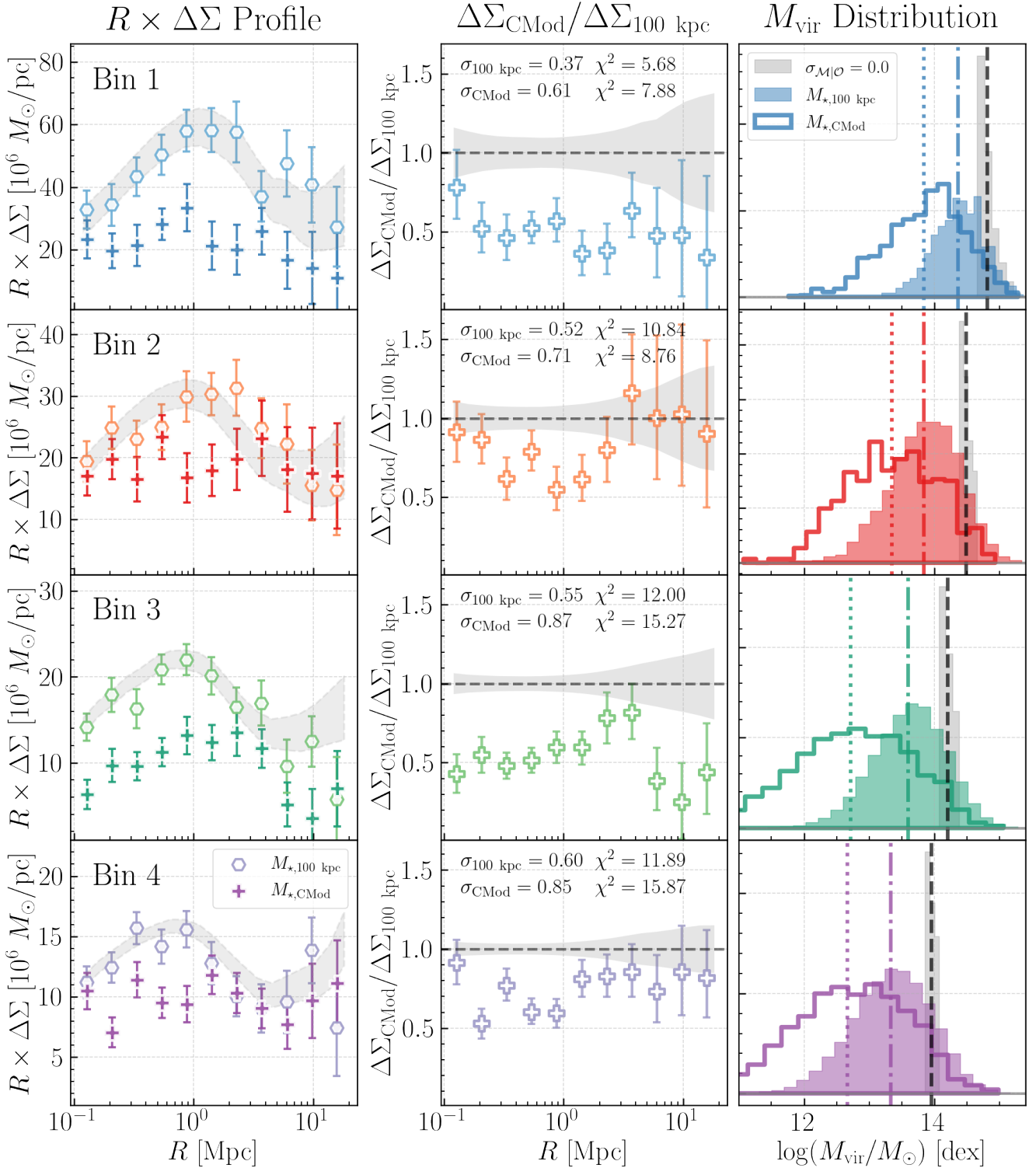


Figure 7. Top- N results for $M_{*,100 \text{ kpc}}$ and $M_{*,\text{cmod}}$. The format of this figure is the same as Figure 6. **Left** column: the $R \times \Delta\Sigma$ profiles for the $M_{*,100 \text{ kpc}}$ - (circles) and $M_{*,\text{cmod}}$ -selected (crosses) samples. The lensing amplitude for $M_{*,100 \text{ kpc}}$ is significantly higher than for $M_{*,\text{cmod}}$ in all four bins. Even without fitting a model, it is obvious that $M_{*,100 \text{ kpc}}$ is a much better tracer of M_{vir} than $M_{*,\text{cmod}}$. **Middle** column: the ratio of $\Delta\Sigma$ profiles. Samples selected by $M_{*,\text{cmod}}$ have lensing amplitudes $\sim 30\text{-}50\%$ lower than $M_{*,100 \text{ kpc}}$ selected samples. **Right** column: the inferred M_{vir} distributions for the two samples using the model described in § 2.2.2. Grey shaded regions indicate the M_{vir} distributions of an ideal tracer with $\sigma_{M_{\text{vir}}} = 0$. Vertical lines indicate mean M_{vir} . The differences of the mean M_{vir} between $M_{*,\text{cmod}}$ and $M_{*,100 \text{ kpc}}$ based selections range from 0.2-0.4 dex in Bin 1 & 2 to 0.6-0.8 dex in Bin 3 & 4. The *Jupyter* notebook for reproducing this figure can be found here: [🔗](#)

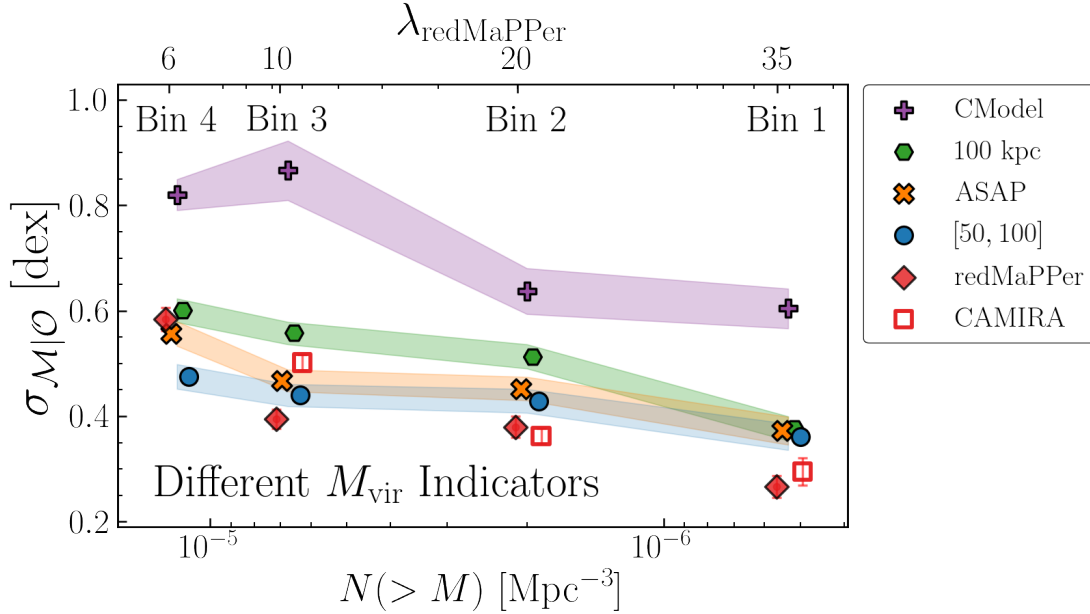


Figure 8. Number density– $\sigma_{M_{\text{vir}}}$ relation for six key M_{vir} proxies (similar format as Figure 5). For CAMIRA, we only show $\sigma_{M_{\text{vir}}}$ in the first three bins since the cluster sample size is not large enough to include Bin 4. $M_{\star,[50,100]}$ shows performance comparable to richness-based proxies with lower $\sigma_{M_{\text{vir}}}$ values at the low- M_{vir} end. While the formal values of $\sigma_{M_{\text{vir}}}$ are better for richness-based estimators for Bin 1, the quality of the fits for richness-based estimators is not as good as for $M_{\star,[50,100]}$. The Jupyter notebook for reproducing this figure can be found here: [🔗](#).

(ii) Which type of M_{vir} proxy can yield $\Delta\Sigma$ profiles whose shapes are consistent with a “clean selection” (we also use the term “pure scatter”) of massive halos? “Clean selection” here means a selection based on a simple log-linear M_{vir} -proxy relation with Gaussian scatter.

Figure 9 compares the $\Delta\Sigma$ profiles of HSC redMaPPer, CAMIRA clusters (first three bins only), and $M_{\star,[50,100]}$ -selected massive halos. In Bin 1 to 3, both the redMaPPer and CAMIRA $\Delta\Sigma$ profiles show similar systematic differences in shape compared to the $M_{\star,[50,100]}$ profiles. The most prominent difference is that, between $1 < R < 3$ Mpc, the richness-based $\Delta\Sigma$ profiles demonstrate significantly enhanced ($\sim 30\text{--}40\%$) $\Delta\Sigma$ amplitudes. On the other hand, at $R < 1$ Mpc, the $\Delta\Sigma$ profiles of redMaPPer and CAMIRA samples are $\sim 20\text{--}40\%$ lower than the outer envelope M_{\star} ones. At larger scale ($R > 5$ Mpc), we find that the richness-based and $M_{\star,[50,100]}$ $\Delta\Sigma$ profiles become statistically similar but we are also limited by the low S/N of the current profiles. Other M_{\star} -based proxies with similar $\sigma_{M_{\text{vir}}}$ values (e.g., $M_{\star,100\text{ kpc}}$, M_{vir} , ASAP, $M_{\star,[50,150]}$) can also yield qualitatively same conclusions. In Appendix F, we show that the SDSS redMaPPer clusters in the HSC S16A footprint display similar systematics in their $\Delta\Sigma$ profiles using HSC lensing data. In appendix G, we show that the DES redMaPPer clusters in the same redshift and richness bins show consistent shape in their lensing profile with the HSC one. The DES sample is not only based on a different imaging dataset, its lensing profile is from an independent shear catalogue with different strategies for shape measurements and lensing calibration. Both of these comparisons demonstrate the robustness of our result. The shape of $\Delta\Sigma$ profiles robustly show that the $\sigma_{M_{\text{vir}}}$ values alone cannot fully explain the difference between M_{\star} - and richness-based M_{vir} proxies. Instead

of the overall higher lensing amplitude expected from the lower $\sigma_{M_{\text{vir}}}$ values for redMaPPer and CAMIRA clusters, we see a “bump”-like feature at $R \sim 1\text{--}2$ Mpc.

In Bin 4, the $\Delta\Sigma$ profile of redMaPPer clusters shows lower amplitude than that of $M_{\star,[50,100]}$ sample, consistent with its higher $\sigma_{M_{\text{vir}}}$ value in this bin. The $\Delta\Sigma$ profile in Bin 4 also does not show a clear 1 Mpc “bump” as in the other three bins.

These results make question (ii) more interesting: are these richness-selected clusters consistent with a selection from a log-linear M_{vir} -richness relation with Gaussian scatter? To address this question, Figure 10 compares the observed $\Delta\Sigma$ profiles of redMaPPer, CAMIRA clusters, and $M_{\star,[50,100]}$ -selected sample to each of their best-fit profiles using our “pure scatter” model (§ 2.2.2). In the larger, left-hand part of Figure 10, each column shows results for a different Top- N selection method, with results from different bins shown in different rows. Within each panel, comparing the points with error bars to the shaded gray band allows us to assess how the *shape* of the $\Delta\Sigma$ profiles compare to theoretical expectations based on an unbiased selection of clusters based on true M_{vir} (i.e., the “pure scatter” model). In the single vertical column on the right-hand side of Figure 10, we show the ratio of the observed $\Delta\Sigma$ to the corresponding profile based on the “pure scatter” model; on the right-hand side, different symbols correspond to results based on different cluster-selection methods.²⁵

From Figure 10 it is visually apparent that clusters selected according to $M_{\star,[50,100]}$ exhibit a $\Delta\Sigma$ profile that

²⁵ We remind the reader that for the case of $M_{\star,[50,100]}$, we remove the possible massive satellites using the procedure described in § 6.1.

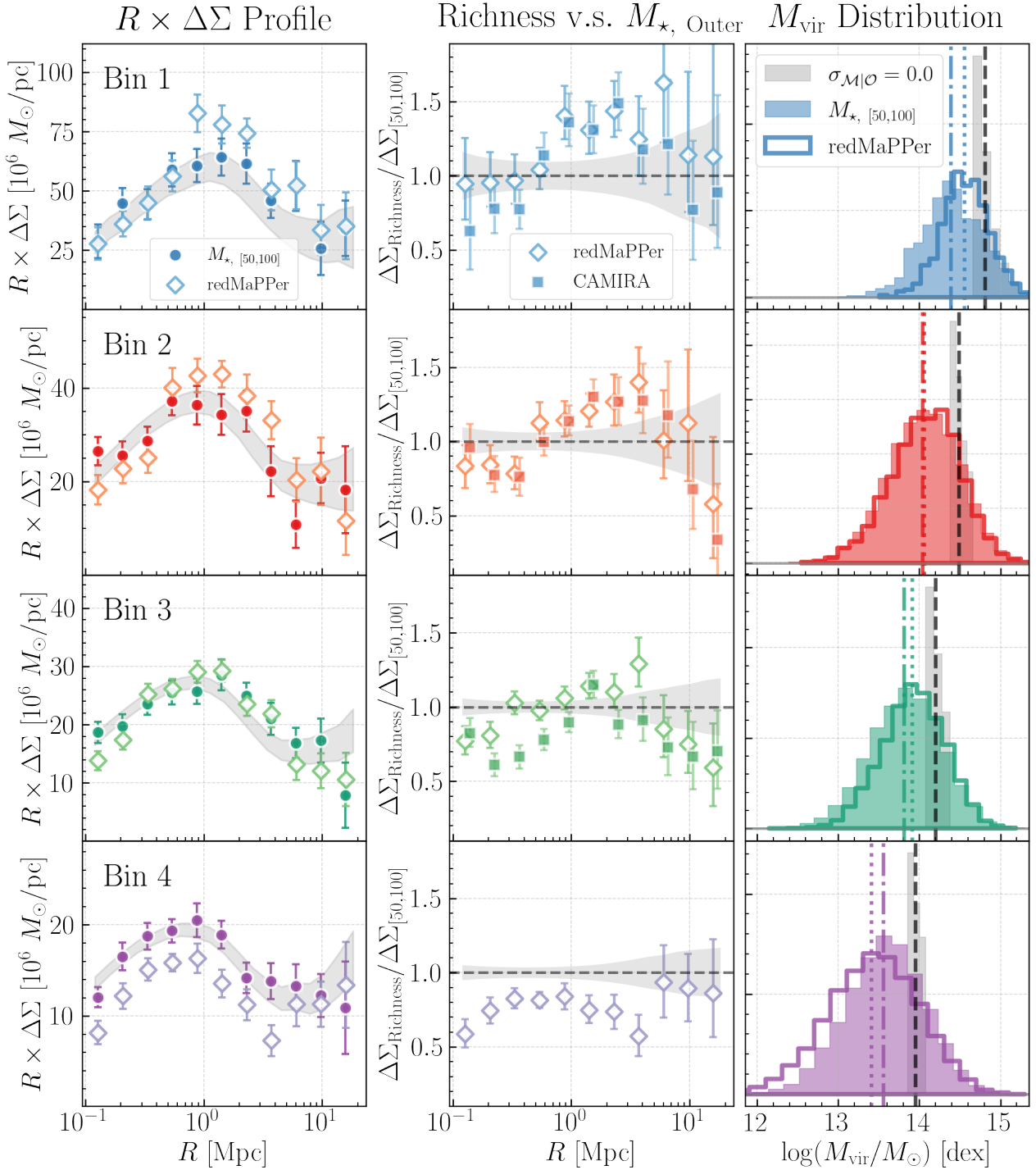


Figure 9. Top- N comparisons between the richness-based optical clusters (**redMaPPer** and **CAMIRA**) and the massive galaxies selected using outer envelope stellar mass ($M_{\star, [50,100]}$). The layout is very similar to Figure 7 and Figure 6. **Left** column compares the $R \times \Delta\Sigma$ profiles of the HSC **redMaPPer** clusters (open diamond) and the $M_{\star, [50,100]}$ (solid circle) selected samples. The grey shaded region shows the best-fit profile of the $M_{\star, [50,100]}$ samples. In Bin 1-3, while the overall lensing amplitudes are similar, there are interesting scale-dependent differences that become more clear using the ratio of the $\Delta\Sigma$ profiles (**middle** column): The lensing amplitudes of **redMaPPer** clusters are systematically higher than the $M_{\star, [50,100]}$ samples around ~ 1 -3 Mpc by ~ 20 -40%. Meanwhile, the amplitudes of **redMaPPer** $\Delta\Sigma$ profiles are slightly lower than or similar to the $M_{\star, [50,100]}$ ones in the central ($R < 0.5$ Mpc) and outer ($R > 6$ -8 Mpc) regions. We also show the ratio of lensing profiles using the HSC **CAMIRA** cluster samples (square filled with grey colour) to highlight the similar behaviour of these two richness-based cluster finders. In Bin 4, the **redMaPPer** sample displays a ~ 20 -50% lower lensing amplitudes than the corresponding $M_{\star, [50,100]}$ sample. In the **right** column, we visualize the trend of the average M_{vir} in each bin: while the **redMaPPer** samples show ~ 0.2 dex higher average M_{vir} value in Bin 1, the differences become smaller in Bin 2 & 3. In Bin 4, the $M_{\star, [50,100]}$ selected sample shows a ~ 0.2 dex higher average M_{vir} values than the **redMaPPer** one instead. The **Jupyter** notebook for reproducing this figure can be found here: [\[link\]](#).

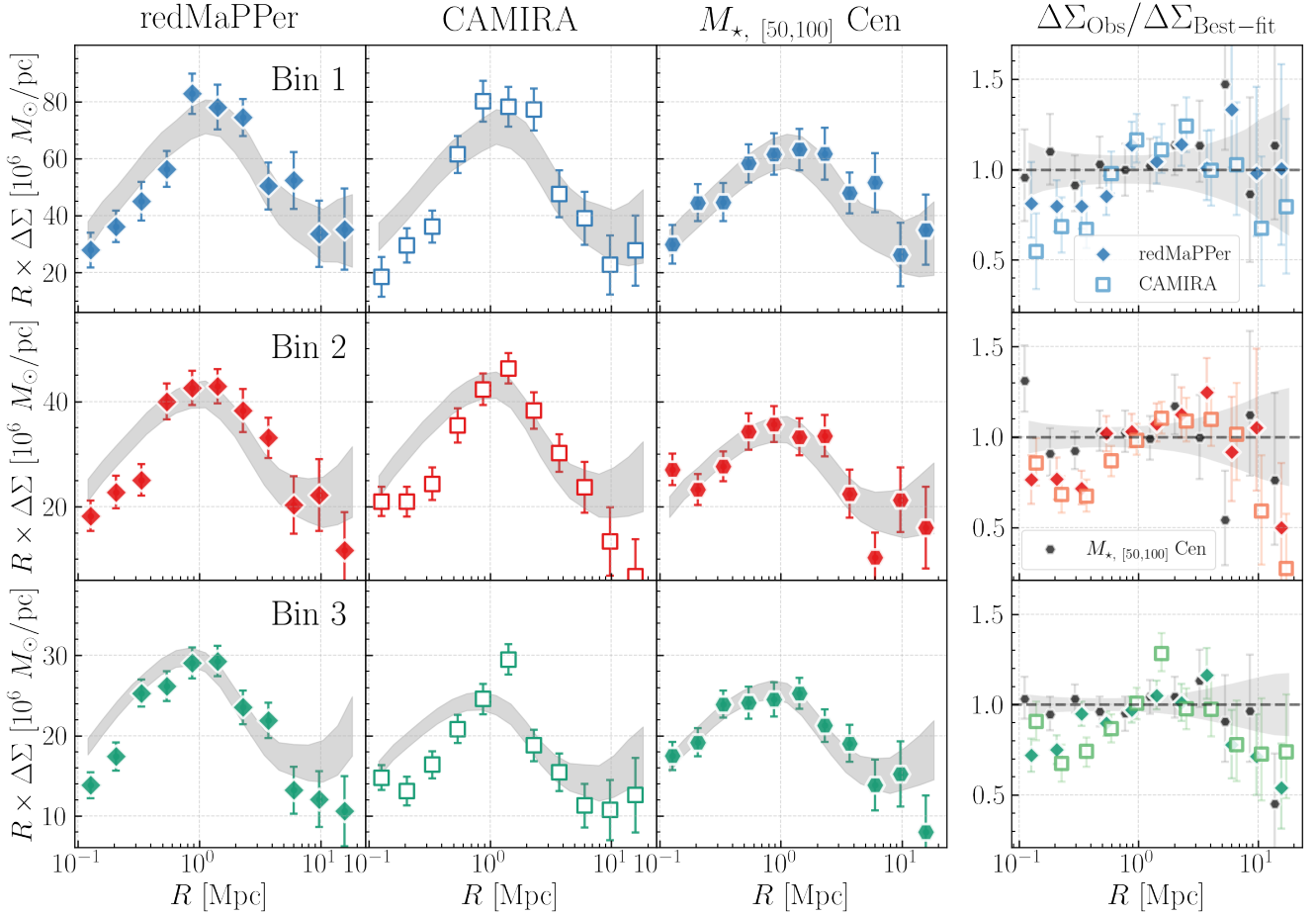


Figure 10. The comparisons between the shape of $R \times \Delta\Sigma$ profiles and the best fit “pure-scatter” model for richness based cluster finders. **Left two columns:** the observed $R \times \Delta\Sigma$ profiles (symbols) and their best-fit models (grey shaded regions) for **redMaPPer** (left; filled diamonds) and **CAMIRA** (middle; open squares) clusters in Bins 1-3. We ignore Bin 4 because the cuts applied to the **CAMIRA** catalogue preclude using this bin. **The third column from the left:** same as the left two columns, but for $M_{\star, [50,100]}$ as a reference for M_{\star} -based M_{vir} proxy (filled hexagons) as reference. **Right column:** ratio of the observed $\Delta\Sigma$ profiles to their best-fit model. We also show the ratio for $M_{\star, [50,100]}$ (grey circles). The simple “pure-scatter” model is not a good fit and scale-dependent “residuals” are clearly visible for richness-based M_{vir} proxies when compared to $M_{\star, [50,100]}$. While the exact values of the ratios are different, the two richness-based cluster finders display qualitatively similar behavior: the observed $\Delta\Sigma$ profiles are lower than the best-fit models at $R < 1$ Mpc by $\sim 30\%$ but show higher amplitudes at 1 – 3 Mpc. This shape of $R \times \Delta\Sigma$ may be a generic “feature” of richness-based cluster selections and could be due to mis-centering or projection effects. The **Jupyter** notebook for reproducing this figure can be found here: [🔗](#)

closely mimics the profile of cluster samples that have been selected according to M_{vir} in an unbiased fashion. Relative to $M_{\star, [50,100]}$ -selected clusters, we can see that neither **redMaPPer** nor **CAMIRA** clusters have $\Delta\Sigma$ profiles that are as well-described by the “pure scatter” model. For both **redMaPPer** and **CAMIRA**, the most prominent residual is the steep drop in the profile in the $R < 1$ Mpc region (by up to $\sim 50\%$) relative to the profile of the corresponding best-fit “pure scatter” model. In addition to this steep drop, the $\Delta\Sigma$ profile of **redMaPPer** and **CAMIRA** clusters presents a distinct “bump-like” feature around 1-2 Mpc in Bin 1 & 2, with profiles that have a visibly larger lensing amplitude relative to the “pure scatter” model at this spatial scale. Using χ^2 to quantify the quality of the fits of the “pure scatter” model, we find that the HSC **redMaPPer** clusters have values of [15.36, 55.92, 46.23] for Bins 1, 2, and 3, respectively; the **CAMIRA S16A** samples have values of [34.51, 35.65, 62.11]; the quality of these fits is thus significantly poorer relative

to $M_{\star, [50,100]}$ -selected clusters. This exercise indicates that the $M_{\star, [50,100]}$ -based selection function closely resembles an unbiased selection of clusters based on M_{vir} with simple, Gaussian scatter, whereas the cluster selection function defined by **redMaPPer** or **CAMIRA** cannot be as well-described by such a simple model.

7 DISCUSSION

We now discuss the implications of the results presented in the previous section. We first discuss the connection between our findings based on the Top- N tests and the **ASAP** model in §7.1. In §7.3, we focus on the potential of the outer envelope mass as a tool for identifying dark matter halos. §7.5 discusses the possibility of using the techniques developed in this paper to search for even better M_{vir} proxies.

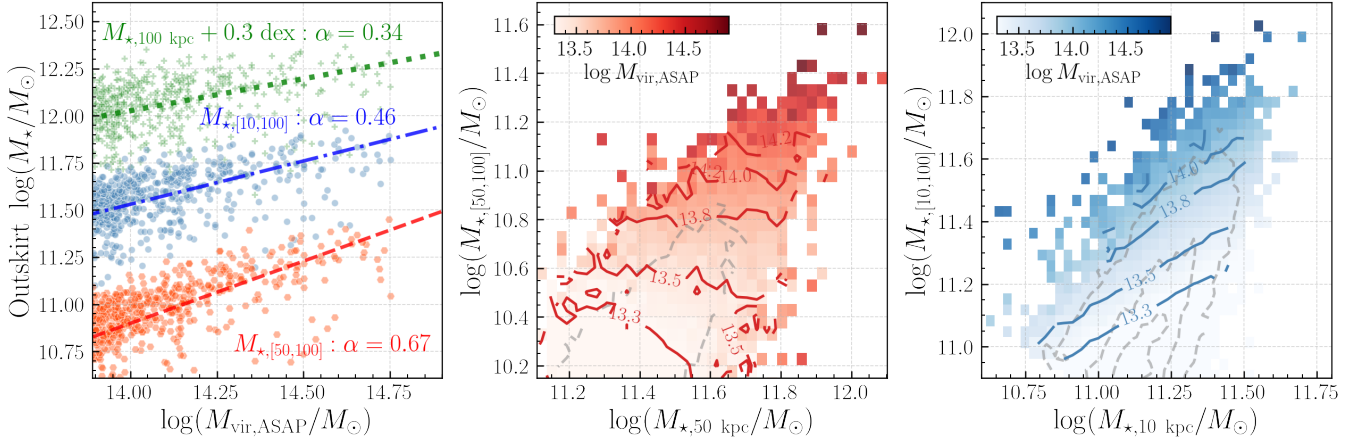


Figure 11. We explore the connections between the ASAP-predicted M_{vir} and the outskirts M_{\star} used in the Top- N test. **Left:** relations between the ASAP-predicted M_{vir} and different stellar mass measurements, including $M_{\star,100 \text{ kpc}}$ (green; shifted up by 0.3 dex for better visibility), $M_{\star,[10,100]}$ (blue), and $M_{\star,[50,100]}$ (red). To help visualize these scaling relations, we highlight the best-fit log-linear relations at $M_{\text{vir, ASAP}} > 10^{13.6} M_{\odot}$. $M_{\star,[50,100]}$ displays steeper slopes than both $M_{\star,100 \text{ kpc}}$ and $M_{\star,[10,100]}$. **Middle:** the 2-D plane of $M_{\star,50 \text{ kpc}}$ v.s. $M_{\star,[50,100]}$ colour coded by the ASAP-predicted M_{vir} . Several iso- M_{vir} contours are used to highlight the relation between M_{vir} and $M_{\star,[50,100]}$. **Right:** similar to the middle panel, here we show the $M_{\star,10 \text{ kpc}}$ and $M_{\star,[10,100]}$ 2-D plane colour-coded by the ASAP-predicted M_{vir} . Same set of iso- M_{vir} contours are used to compare with the middle panel. The **Jupyter** notebook for reproducing this figure can be found here: [🔗](#).

7.1 Relationship with Previous Work and the ASAP model

Using the Top- N tests, we confirm that the ASAP empirical model (Huang et al. 2020) has a lower $\sigma_{M_{\text{vir}}}$ value than large aperture stellar masses such as $M_{\star,100 \text{ kpc}}$ (see Figure 8). However, we also find that ASAP is outperformed by outer mass measured such as $M_{\star,[30,100]}$ and $M_{\star,[50,100]}$.

The ASAP model uses $M_{\star,10 \text{ kpc}}$ and $M_{\star,100 \text{ kpc}}$ as rough proxies of the *in situ* and “total” M_{\star} to take advantage of the additional M_{vir} -dependence of the stellar mass profiles of massive galaxies. However, the Top- N test clearly shows that $M_{\star,10 \text{ kpc}}$ alone is a very poor M_{vir} proxy with $\sigma_{M_{\text{vir}}} \sim 0.8$ in all four bins (see Figure 5). Therefore, the better performance of $M_{\text{vir, ASAP}}$ must be driven by a tighter $M_{\text{vir}}-M_{\star,[10,100]}$ relation than $M_{\text{vir}}-M_{\star,100 \text{ kpc}}$.

Figure 11 shows the $M_{\text{vir, ASAP}}$ -observable relations for $M_{\star,100 \text{ kpc}}$, $M_{\star,[10,100]}$, and $M_{\star,[50,100]}$ with their best-fit log-linear relations at $M_{\text{vir, ASAP}} \geq 10^{13.6} M_{\odot}$ ²⁶. Although $M_{\text{vir, ASAP}}$ is not the true M_{vir} , it can be used to illustrate the underlying average SHMRs. The slope of the $M_{\text{vir, ASAP}}-M_{\star,[10,100]}$ relation is $\alpha = 0.47$, steeper than that of the $M_{\text{vir, ASAP}}-M_{\star,100 \text{ kpc}}$ relation $\alpha = 0.34$. Both relations have similar scatter values $\sigma_{M_{\star}} \sim 0.15$ dex at the high- $M_{\text{vir, ASAP}}$ end. Hence, the ASAP model predictions also suggest that outer mass $M_{\star,[10,100]}$ is a better M_{vir} proxy than $M_{\star,100 \text{ kpc}}$.

Figure 11 also compares the $M_{\text{vir, ASAP}}-M_{\star,[10,100]}$ and the $M_{\star,[50,100]}$ relations. Although ASAP does not explicitly use $M_{\star,[50,100]}$, it shows that $M_{\star,[50,100]}$ is a better M_{vir} proxy than $M_{\star,[10,100]}$ because the $M_{\text{vir, ASAP}}-M_{\star,[50,100]}$ relation has a steeper slope ($\alpha = 0.67$) and slightly smaller $\sigma_{M_{\star}} \sim 0.11$ dex at $M_{\text{vir, ASAP}} \geq 10^{13.6} M_{\odot}$. To further highlight this point, we also show the $M_{\star,50 \text{ kpc}}-M_{\star,[50,100]}$ and $M_{\star,10 \text{ kpc}}-M_{\star,[10,100]}$ 2-D planes. At $M_{\text{vir, ASAP}} > 10^{13.5} M_{\odot}$,

the iso- $M_{\text{vir, ASAP}}$ curves runs almost parallel to $M_{\star,[50,100]}$. When compared to the $M_{\star,10 \text{ kpc}}-M_{\star,[10,100]}$ distributions in the right panel, it becomes clear that at fixed outskirts M_{\star} value, $M_{\star,[50,100]}$ will yield smaller scatter of $M_{\text{vir, ASAP}}$. This comparison reaffirms the finding that the $R > 30-50$ kpc outer mass is an excellent M_{vir} proxy and that adding M_{\star} from inner regions actually degrades the scatter. This also suggests that ASAP-like models could be improved using an optimized choice for the outer mass tracer.

The idea behind the original ASAP model was to use two different radii of tracer regions dominated by *in situ* and *ex situ* stars. Our Top- N tests suggest the the *in situ* may actually contain very little information about present day halo mass. A next key step will be understanding the different SHMRs of *in situ* and *ex situ* stars better in the near future.

7.2 Scatter in Stellar Mass at Fixed Halo mass

In this work, we focus on the $\sigma_{M_{\text{vir}}}$ values and their trends with number density. Meanwhile, works about SHMR often focus on the $\sigma_{M_{\star}}$ values. For $M_{\star,100 \text{ kpc}}$, assuming a SHMR with $\alpha \sim 0.35$ slope (e.g., Golden-Marx & Miller 2019; Huang et al. 2020), a $\sigma_{M_{\star}} \sim 0.2$ dex scatter at high- M_{vir} end corresponds to a $\sigma_{M_{\text{vir}}} \sim 0.4$ dex scatter according to Equation 6. This is consistent with our results at high- M_{vir} end and with some recent modelling constraints (e.g., Kravtsov et al. 2018; Behroozi et al. 2018). Meanwhile, the $\sigma_{M_{\text{vir}}}$ values in lower- M_{vir} bins require $\sigma_{M_{\star}} > 0.3$ dex under the same slope. For the CAMIRA clusters, if we adopt the M_{vir} -richness relation calibrated by Murata et al. (2019) with a $\alpha = 0.6$ slope, the inferred $\sigma_{M_{\star}}$ values are around 0.25 to 0.35 dex. For $M_{\star,[50,100]}$, assuming the $\alpha \sim 0.67$ slope from the ASAP model shown in § 7.1, we derive a larger $\sigma_{M_{\star}}$ value (~ 0.4 dex) for this outskirts M_{\star} than $M_{\star,100 \text{ kpc}}$ and richness measurements. As the $\sigma_{M_{\star}}$ value inferred here is *not* the intrinsic scatter value, this result may reflect the noisier

²⁶ We use the Python implementation of the Least Trimmed Squares (LTS) algorithm (**ltsfit**) by Cappellari et al. (2013) for the fitting.

measurements of outer light profile. Since we do not directly constrain the SHMRs, the inferred σ_{M_\star} values here depend on the assumed slope values and other systematics. They should be only used for relative comparisons within the Top- N results. We will look into the constraint of SHMRs for different M_{vir} proxies in future works.

7.3 Physical Insight: Why might the Outer Stellar Halo Trace Halo Mass Better than the Inner Mass or the Total Mass?

Our Top- N tests show that the outer mass of $z < 0.5$ massive galaxies are promising halo mass proxies with superior performance compared to “total” M_\star measurements using large apertures. This result may be explained via the “two-phase” formation scenario of massive galaxies (e.g., Oser et al. 2010; van Dokkum et al. 2010; Moster et al. 2020). According to this picture, a massive galaxy consists of stars formed within the halo of its main progenitor at high redshift (*in situ* component) and accreted stars from repeated mergers (*ex situ* component). In Bradshaw et al. (2020), the authors explored the SHMRs of both components using the UniverseMachine semi-empirical model (e.g., Behroozi et al. 2018). They showed that the *ex situ* component displays a much tighter correlation with the current M_{vir} relative to either the *in situ* component (see their Figure 9), or relative to the total M_\star . In the UniverseMachine model, the average *in situ* M_\star at $z \sim 0.4$ is almost constant over a wide range of M_{vir} ($\sim 10^{10.9} M_\odot$), whereas the SHMR of *ex situ* component shows a steep slope. In a recent analysis of the TNG-300 simulation, it was found that at fixed M_{vir} , both cluster richness and BCG M_\star exhibit residual correlations with halo assembly history (Anbajagane et al. 2020); our results provide motivation to consider whether such correlations persist for true *ex situ* M_\star , and for M_\star estimations of the BCG that exclude the inner regions. Although different models and simulations display different scaling relations between M_{vir} and *ex situ* M_\star , there is nonetheless compelling theoretical support for the idea that the scatter of SHMRs at high- M_{vir} end is closely tied to the assembly of the *ex situ* component (see, e.g., Gu et al. 2016).

Whereas massive galaxies at high redshift grow primarily by *in situ* mass buildup, these galaxies are predominantly quenched at lower redshift, implying that massive galaxies grow primarily via merging at late times. Under this picture, the *ex situ* M_\star should scale with the number of accreted satellites, and can be considered as a measure of “historical richness” of the halo. In simulations, the *ex situ* component dominates the outskirts of massive galaxies, and its fraction increases with both stellar and halo mass (e.g., Lackner et al. 2012; Rodriguez-Gomez et al. 2016; Pulsoni et al. 2021; Pillepich et al. 2018). For this reason, outer mass measures such as $M_{\star,[50,100]}$ are likely to scale better with the true *ex situ* M_\star relative to mass estimates that include stars from the inner 30 kpc, and so M_\star measurements defined by the outskirts of a galaxy may be proxies of the “historical richness” of a parent halo.

For low- z galaxy clusters, multiple studies have explored the connection between halo properties and the flux, shape, and radial profile of the ICL – essentially the extended outer envelope around the central galaxy (or the BCG) of the cluster (e.g., Montes & Trujillo 2018, 2019;

Zhang et al. 2019a; Furnell et al. 2021; Kluge et al. 2021; Sampaio-Santos et al. 2021). While several of these studies demonstrate the tight correlation between the M_{vir} and the stellar mass/luminosity of the BCG+ICL component²⁷ (e.g., Zhang et al. (2019a); Kluge et al. (2021); Sampaio-Santos et al. (2021)), whether the ICL alone is a promising M_{vir} proxy is still under debate (e.g., Furnell et al. 2021). As discussed in Huang et al. (2018c) and Kluge et al. (2020), the definition of ICL is often ambiguous and somewhat arbitrary, but the light between 50 to 100 kpc around a BCG is often considered part of the ICL. Our results support the idea that the ICL correlates with halo mass, but we also generalize this finding to all massive galaxies.

7.4 On the Possibility of Building Even Better Halo Mass Proxies

Our work shows that a better understanding of the formation process of massive galaxies, together with high quality imaging data, offers the exciting prospect of developing better proxies of halo mass. This work is only a first step in this direction and follow-up work may yield even better proxies than $M_{\star,[50,100]}$. Here we discuss possible improvements to the outskirts M_\star -based M_{vir} proxy.

First, the outer stellar mass is estimated using the portion of the light profile that has low S/N, which can potentially be affected by issues related to background subtraction, by contamination from other objects, and by galactic cirrus (e.g., Román et al. 2020). Deeper images and improved data-reduction strategies should help improve the accuracy of measurements of outer mass. Second, we have ignored the radial variation of M_\star/L_\star , and also the fact that galaxies are three-dimensional in nature.

More importantly, our results provide motivation for the quest for better proxies of *ex situ* M_\star . For example, it could prove fruitful to explore improved definitions of outer stellar mass based on physical radial boundaries. In this work, we have explored boundaries based on R_{50} (Appendix E) and found no substantial improvement beyond results based on $M_{\star,[50,100]}$, but scaling boundaries according to the total M_\star might still be an interesting idea. This research direction is also motivated by recent simulations which are able to reproduce HSC light profiles fairly well (e.g., Ardila et al. 2021). Ideally, we would like to be able to physically decompose massive galaxies into their *in situ* and *ex situ* components using real data. More careful approaches towards this decomposition that take these additional effects into account is worthy of exploration in future work and are well-motivated by our results.

7.5 Implications for Optical Cluster Finding

Our results have profound implications for cluster finding with optical surveys including the Vera Rubin Observatory’s Legacy Survey of Space and Time (LSST)²⁸, the *Euclid*

²⁷ This is sometimes referred as the “diffuse stellar light” component following the definition in the Illustris-TNG simulation (e.g., Zhang et al. 2019a; Sampaio-Santos et al. 2021).

²⁸ <https://www.lsst.org>

satellite²⁹, and the Nancy Grace Roman space telescope (*Roman*)³⁰. These results potentially open up a new way of approaching the problem of identifying massive halos from imaging surveys.

Traditionally, optical/NIR cluster finders are mostly based on the relation between M_{vir} and some estimate of cluster richness. The **redMaPPer** and **CAMIRA** cluster finders rely on the number of quenched member galaxies on the red-sequence, while others use the over-density of galaxies within a narrow photo- z range (e.g., [Wen & Han 2021](#); [Zou et al. 2021](#)). The prevalence of richness-based cluster identification reflects the widely-held expectation that the M_{vir} -richness relation has lower scatter than the SHMR. However, in this work we have shown that this comparative assessment has overlooked two critical aspects of the M_* estimation of massive galaxies. 1) Default photometry from data reduction pipelines often provide poor fits to the light profiles of massive galaxies, and can be significantly impacted by issues related to background subtraction and deblending. Such photometry is a source of both bias and additional scatter in the M_* estimates (see Figure 8 and § 6.2.3). 2) Inner stellar mass is an *intrinsically* poor proxy of M_{vir} (see Figure 5 and § 6.2.1). Yet, commonly adopted photometry measures for massive galaxies focus on the bright, inner “core” region where the signal-to-noise is high. Our Top- N tests demonstrate that both of these issues have a strong influence on the level of scatter in the SHMR. We have furthermore shown that through careful consideration of how the M_* -based proxy is measured and defined, cluster samples selected by M_* exhibit scatter in M_{vir} that is both tighter and simpler relative to richness-selected clusters. Finally, it is important to note that customized estimates of the outer light profiles of massive galaxies are necessary to build M_{vir} proxies with comparable $\sigma_{M_{\text{vir}}}$ values with richness (at least with current versions of data reduction pipeline).

Outer galaxy mass may offer distinct advantages over richness-based cluster finders with respect to two key systematics: mis-centering and projection effects. Mis-centering bias occurs when the cluster finder identifies the wrong central galaxy, or when the central galaxy is not at the true center of the dark matter halo. Projection effects have a variety of origins, such as the anisotropic distribution of satellite galaxies within the halo, and the presence of large-scale structure along the line-of-sight to the cluster. While the calibration of the M_{vir} -richness relation now routinely includes mis-centering effects when modelling cluster $\Delta\Sigma$ profiles (e.g., [Murata et al. 2018, 2019](#); [McClintock et al. 2019](#)), projection bias is still a major issue (e.g., [Costanzi et al. 2019](#); [Sunayama et al. 2020](#); [Abbott et al. 2020b](#); [To et al. 2021a](#)). In this paper, we show that M_* -based proxies using both larger apertures or outer mass display stacked $\Delta\Sigma$ profiles that are consistent with having negligible mis-centering effect and projection bias (see Figure 9 and § 6.3) – this is very exciting as it suggests that outer mass measures such as $M_{*,[50,100]}$ directly trace central galaxies and could yield a more simple selection function than richness-based methods.

We have not identified the exact causes of the systematic differences in the $\Delta\Sigma$ profiles between M_* - and richness-

selected samples (§ 6.3). Recently, [Sunayama et al. \(2020\)](#) explored the impact of projection bias on cluster $\Delta\Sigma$ profiles using mock catalogues based on N-body simulations. They show that projection effects can boost the stacked $\Delta\Sigma$ profiles of clusters at $R > 2$ Mpc by up to 20%. Also, this “bump” in the the outer $\Delta\Sigma$ profile seems to increase with the intrinsic richness. While there are qualitative similarities between their Figure 4 and the middle panels of Figure 9, the [Sunayama et al. \(2020\)](#) model cannot not fully explain the differences we see, and so a sophisticated modelling effort will be required in order to fully understand the origin of this feature in the lensing profiles of richness-selected clusters.

Another key limitation of richness-based cluster finders stems from the difficulty of generating realistic mock catalogues of galaxies. Such mocks are essential for the calibration of the M_{vir} -richness relation and for understanding the selection biases. However, considerable sophistication is required to produce these mock catalogues, since red-sequence richness estimation fundamentally requires that the mock galaxies have multi-wavelength properties such as a tight red-sequence and colour bimodality for *all* galaxies down to $\sim 0.1L_*$, and moreover that these features are realistically connected to the cosmic density field across a wide range of halo mass, redshift and larger-scale environment; thus the mocks used for cluster analysis by cosmological surveys have historically struggled to meet these challenges at the required levels of quantitative detail (e.g., [Trayford et al. 2015, 2017](#); [Nelson et al. 2018](#); [DeRose et al. 2019](#), although see [Hearin et al. 2020](#); [DeRose et al. 2021](#) for recent progress). It is also difficult to take systematics in colour measurements into account when building mocks.

On the other hand, it is easier to calibrate M_* estimates using the same definition of stellar mass (e.g., [Ardila et al. 2021](#)) and to account for uncertainties in M_* . It is also easier to reproduce the observed properties of galaxy samples composed primarily of centrals (e.g., [Moster et al. 2020](#)). To utilise a M_* -based “cluster finder”, we would nonetheless need to account for contamination from massive satellite galaxies (see 6.1), but generating the required mock catalogues for this purpose is far simpler in comparison to the multi-wavelength needs of richness-based methods.

Lastly, the combination of M_* together with richness-based cluster finders could help unveil more insight into the assembly history of massive dark matter halos. Measures of “historical” and “current” richness might have different selection effects with regards to secondary properties (e.g., concentration, merging history) at similar M_{vir} . As mentioned previously, the M_* and richness-selected samples do not fully overlap. Among the top 50 galaxies selected by $M_{*,[50,100]}$, 7 of them are not identified as the central of any **redMaPPer** and **CAMIRA** cluster. The non-overlap fraction increases with decreasing M_* limits: among the top 200 (1000) $M_{*,[50,100]}$ -selected galaxies, 49 (467) are not considered cluster centrals by **redMaPPer** or **CAMIRA**. If we limit the samples to the same Top- N bin, the overlap fraction is even lower: within the top 50 (500) $M_{*,[50,100]}$ galaxies, only 9 (158) of them are also included in the top 50 (500) richest clusters selected by **redMaPPer**. This suggests that the richness- M_* relation for central galaxies has considerable scatter that would be worth exploring in further detail. The numerous advantages discussed above suggest that M_* -based cluster finders could not only help us to understand

²⁹ <https://sci.esa.int/web/euclid>

³⁰ <https://roman.gsfc.nasa.gov>

the systematics of richness-based cluster finders, but that they may also yield competitive constraints on the growth of structure and on galaxy-halo connection models.

8 SUMMARY AND CONCLUSIONS

Taking advantage of the deep images and unprecedented lensing capabilities of the HSC survey (§ 3.1), we show that the outer envelope of low-redshift massive galaxies is a promising M_{vir} proxy with scatter comparable to richness. We further show that this proxy is less affected by systematics such as projection bias and mis-centering effects. The outskirts of massive galaxies are dominated by *ex situ* stars – the stellar content accreted from previous satellites galaxies within the halo – and thus the outer envelope M_* provides an estimate of the “historical richness” of massive halos. This opens up new possibilities for tracing massive halos, studying their galaxy-halo connection, and investigating the assembly histories of massive galaxies.

We have conducted our study by comparing the stacked $\Delta\Sigma$ profiles (§ 4.2 and Appendix A) of massive halos selected by different M_{vir} proxies (§ 2.1 and § 2.2.1) in four volume number density bins (§ 5.2). Assuming a simple log-linear M_{vir} -observable relation model with Gaussian scatter, we estimate the scatter in M_{vir} in each bin by matching the observed $\Delta\Sigma$ profiles to models generated from N-body simulations (§ 2.2.2). Using this Top- N methodology, we evaluate different M_* -based and richness-based M_{vir} proxies for massive galaxies and halos at $0.2 < z < 0.5$ (§ 5). These proxies include M_* based on the default survey photometry (CModel), large aperture M_* (§ 5.1.2) and outer envelope M_* (§ 5.1.3) based on deep 1-D surface mass density profiles (§ 4.1). We also include richness estimates from the redMaPPer (§ 3.3.1) and CAMIRA cluster (§ 3.3.2) catalogues. The main results of this work are:

- Outer galaxy mass is an excellent tracer of halo mass (§ 6.2.2; Figure 5). The performance of $M_{*,[50,100]}$ and other similar outer envelope measures are competitive with red-sequence cluster finders at the high-richness end (e.g. $\lambda > 20$) and may outperform redMaPPer or CAMIRA at the low-richness regime (see Figure 8). Since the outer envelope is likely to have been built from merging processes, we suggest that the outer envelope mass serves as an estimate of the “historical richness” of a cluster, and so could serve as a proxy for M_{vir} that is complementary to the “current richness” measurements used by contemporary cluster finders.

- While both richness-based M_{vir} proxies (redMaPPer and CAMIRA) have impressively low inferred $\sigma_{M_{\text{vir}}}$ values, they result in stacked $\Delta\Sigma$ profiles that are not consistent with predictions based on a “pure scatter” model (see Figure 9). Instead, the $\Delta\Sigma$ profiles of richness-selected clusters have enhanced amplitudes around $R \sim 1\text{--}2$ Mpc and suppressed inner profiles at $R < 1$ Mpc when compared to “pure scatter” models (§ 6.3 and Figure 10). These results indicate that the richness-based M_{vir} proxies have additional systematics (e.g., mis-centering, projection effect) that need to be accounted for. In contrast, the $\Delta\Sigma$ profiles of galaxies selected according to their outer mass are very well described by a “pure scatter” model, suggesting that cluster samples selected by stellar mass of the outer envelope suffer from little to no mis-centering effects or projection effects.

- Inner galaxy mass (e.g. M_* within 10 to 30 kpc) is a very poor tracer of halo mass (Figure 5). The total M_* enclosed within a large aperture such as $M_{*,100 \text{ kpc}}$ shows much better performance, but is still not as effective as the outer envelope mass in terms of its ability to serve as a proxy for M_{vir} (Figure 6). This indicates that there is a comparatively weak physical correlation between the stars in the inner region of massive galaxies and the total mass of their dark matter halos.

- Stellar masses based on CModel or any other default photometry from a generic data reduction pipeline do not yield good halo mass proxies (see § 6.2.3 and Figure 7). CModel does not accurately account for the flux in the extended stellar halo of massive galaxies, which is the specific region of the galaxy that has the tightest connection with the underlying M_{vir} . We therefore caution against the use of CModel-like photometry in studies of the galaxy-halo connection. LSST will eventually be even deeper than HSC and currently shares a very similar data reduction pipeline. In order to realise the scientific potential afforded by accurate measurements of the masses and profiles of massive galaxies, it will be critical to improve the image deblending and galaxy modelling algorithms in lsstPipe. It would highly beneficial to the wider cosmology community if lsstPipe could accurately perform the required measurements without the need for the custom pipelines that were needed for the present work.

- We have shown that satellite galaxies do not have a strong impact on the stacked $\Delta\Sigma$ profile of the highest M_* samples (due to low satellite fraction). Satellites do impart a mild effect on $\Delta\Sigma$ towards the lower- M_* end (§6.1) – further work will be required in order to model this effect for cosmological applications.

Motivated by these results, we plan to further explore M_* -based M_{vir} proxies for studies of the galaxy-halo connection and for cosmology. Recent HSC data releases (S20A or PDR3 in 2021) have increased sky coverage to $> 600 \text{ deg}^2$, four times larger than the current sample. Not only would these larger samples improve the statistical uncertainty of the Top- N tests, they would also enable us to explore the high- M_{vir} regime in much finer detail than is permitted by the broad richness bins used here. Moreover, the new data releases come with improved background subtraction that will improve measurements of the outer profile of massive galaxies. We are also working on an improved outer envelope M_* measurement using a more accurate M_*/L_* and a more sophisticated modelling approach. On the theoretical side, we will use state-of-the-art hydro-simulations and semi-empirical models to investigate the connection between the outer envelope of massive galaxies and the assembly history of their dark matter halo. It would also be interesting to compare cluster samples selected by richness- and M_* -based methods. In addition to the selection biases of different methods, this could yield further insight into the distribution of halo properties at the high- M_{vir} end. Finally, for purposes of developing an M_* -based cluster finder, it will also be fruitful to compare the properties of M_* -selected clusters to samples identified by other multi-wavelength methods that are less sensitive to projection effect (e.g., samples identified in X-ray or microwave bands).

As outlined in Bradshaw et al. (2020), we also suggest

that a “hybrid” cluster finder that combines the advantages of richness- and M_* -based M_{vir} proxies may be possible by simply combining the M_* of the central galaxy and a few (e.g., top 2 or 3) massive satellite galaxies. Such a “Cen+ N ” method could be an excellent M_{vir} proxy, with low $\sigma_{M_{\text{vir}}}$ values in a given number density bin, while also being minimally impacted by projection effects.

Both the M_* -based and the “Cen+ N ” methods require accurate identification of massive satellite galaxies. This is a challenging task when using photometric redshift from imaging surveys. Spectroscopic surveys such as DESI (e.g., [DESI Collaboration et al. 2016](#)) will greatly improve the situation. Using images from the DECam Legacy Survey (DECaLS, e.g., [Dey et al. 2019](#))³¹, we will measure large aperture and outer envelope M_* of $z < 0.5$ massive galaxies out to ~ 100 kpc (e.g., Li et al. in prep.). When combined with their DESI spec- z in the next few years, this much larger DECaLS ($\sim 9000 \text{ deg}^2$) survey will provide us an ideal sample to constrain galaxy-halo connection models. We will extend our Top- N tests to include group/cluster catalogues for DECaLS (e.g., [Yang et al. 2020](#); [Zou et al. 2021](#)), and apply our “Cen+ N ” method to define a sample of massive halos that are suitable for unbiased cosmological analysis.

DATA AVAILABILITY STATEMENTS

The data underlying this article are available in Zenodo at <https://doi.org/10.5281/zenodo.5259075>. The Python code, Jupyter notebooks, and the data files for reproducing the results and figures of this work can be found on Github at <https://github.com/dr-guangtou/jianbing>. The Hyper Suprime-Cam Subaru Strategi Program data used in this work are included in the Public Data Release 2 at <https://hsc-release.mtk.nao.ac.jp/doc/>.

ACKNOWLEDGEMENTS

The authors would like to thank Benedikt Diemer and Matthew Becker for useful discussions and suggestions.

This material is based upon work supported by the National Science Foundation under Grant No. 1714610.

The authors acknowledge support from the Kavli Institute for Theoretical Physics. This research was also supported in part by National Science Foundation under Grant No. NSF PHY11-25915 and Grant No. NSF PHY17-48958

We acknowledge use of the lux supercomputer at UC Santa Cruz, funded by NSF MRI grant AST 1828315. AL is supported by the U.D Department of Energy, Office of Science, Office of High Energy Physics under Award Number DE-SC0019301. AL acknowledges support from the David and Lucille Packard foundation, and from the Alfred .P Sloan foundation.

JD is supported by the Chamberlain Fellowship at Lawrence Berkeley National Laboratory.

The Hyper Suprime-Cam (HSC) collaboration includes the astronomical communities of Japan and Taiwan, and

Princeton University. The HSC instrumentation and software were developed by National Astronomical Observatory of Japan (NAOJ), Kavli Institute for the Physics and Mathematics of the Universe (Kavli IPMU), University of Tokyo, High Energy Accelerator Research Organization (KEK), Academia Sinica Institute for Astronomy and Astrophysics in Taiwan (ASIAA), and Princeton University. Funding was contributed by the FIRST program from Japanese Cabinet Office, Ministry of Education, Culture, Sports, Science and Technology (MEXT), Japan Society for the Promotion of Science (JSPS), Japan Science and Technology Agency (JST), Toray Science Foundation, NAOJ, Kavli IPMU, KEK, ASIAA, and Princeton University.

Funding for SDSS-III has been provided by Alfred P. Sloan Foundation, the Participating Institutions, National Science Foundation, and U.S. Department of Energy. The SDSS-III website is <http://www.sdss3.org>. SDSS-III is managed by the Astrophysical Research Consortium for the Participating Institutions of the SDSS-III Collaboration, including University of Arizona, the Brazilian Participation Group, Brookhaven National Laboratory, University of Cambridge, University of Florida, the French Participation Group, the German Participation Group, Instituto de Astrofísica de Canarias, the Michigan State/Notre Dame/JINA Participation Group, Johns Hopkins University, Lawrence Berkeley National Laboratory, Max Planck Institute for Astrophysics, New Mexico State University, New York University, Ohio State University, Pennsylvania State University, University of Portsmouth, Princeton University, the Spanish Participation Group, University of Tokyo, University of Utah, Vanderbilt University, University of Virginia, University of Washington, and Yale University.

The Pan-STARRS1 surveys (PS1) have been made possible through contributions of Institute for Astronomy; University of Hawaii; the Pan-STARRS Project Office; the Max-Planck Society and its participating institutes: the Max Planck Institute for Astronomy, Heidelberg, and the Max Planck Institute for Extraterrestrial Physics, Garching; Johns Hopkins University; Durham University; University of Edinburgh; Queen’s University Belfast; Harvard-Smithsonian Center for Astrophysics; Las Cumbres Observatory Global Telescope Network Incorporated; National Central University of Taiwan; Space Telescope Science Institute; National Aeronautics and Space Administration under Grant No. NNX08AR22G issued through the Planetary Science Division of the NASA Science Mission Directorate; National Science Foundation under Grant No. AST-1238877; University of Maryland, and Eotvos Lorand University.

This research makes use of software developed for the Large Synoptic Survey Telescope. We thank the LSST project for making their code available as free software at <http://dm.lsstcorp.org>.

The CosmoSim database used in this research is a service by the Leibniz-Institute for Astrophysics Potsdam (AIP). The MultiDark database was developed in cooperation with the Spanish MultiDark Consolider Project CSD2009-00064.

This research made use of: [STSCI_PYTHON](#), a general astronomical data analysis infrastructure in Python. [STSCI_PYTHON](#) is a product of the Space Telescope Science Institute, which is operated by Association of Universities for Research in Astronomy (AURA) for NASA; [SciPy](#), an

³¹ <https://www.legacysurvey.org/>

open source scientific tool for Python (Jones et al. 2001); **NumPy**, a fundamental package for scientific computing with Python (Walt et al. 2011); **Matplotlib**, a 2-D plotting library for Python (Hunter 2007); **Astropy**, a community-developed core Python package for astronomy (Astropy Collaboration et al. 2013); **scikit-learn**, a machine-learning library in Python (Pedregosa et al. 2011); **IPython**, an interactive computing system for Python (Pérez & Granger 2007); **sep** Source Extraction and Photometry in Python (Barbary et al. 2015); **palettable**, colour palettes for Python; **emcee**, Seriously Kick-Ass MCMC in Python; **Colossus**, COsmology, haLO and large-Scale StrUcture toolS (Diemer 2015).

REFERENCES

- Abazajian K. N., et al., 2009, *ApJS*, **182**, 543
- Abbott T. M. C., et al., 2018, *ApJS*, **239**, 18
- Abbott T. M. C., et al., 2020a, *Phys. Rev. D*, **102**, 023509
- Abbott T. M. C., et al., 2020b, *Phys. Rev. D*, **102**, 023509
- Aguena M., et al., 2021, *MNRAS*, **502**, 4435
- Ahumada R., et al., 2020, *ApJS*, **249**, 3
- Aihara H., et al., 2017b, preprint, ([arXiv:1702.08449](https://arxiv.org/abs/1702.08449))
- Aihara H., et al., 2017a, preprint, ([arXiv:1704.05858](https://arxiv.org/abs/1704.05858))
- Aihara H., et al., 2019, *PASJ*, **71**, 114
- Allen S. W., Evrard A. E., Mantz A. B., 2011, *ARA&A*, **49**, 409
- Anbajagane D., Evrard A. E., Farahi A., Barnes D. J., Dolag K., McCarthy I. G., Nelson D., Pillepich A., 2020, *MNRAS*, **495**, 686
- Applegate D. E., et al., 2014, *MNRAS*, **439**, 48
- Applegate D. E., et al., 2016, *MNRAS*, **457**, 1522
- Ardila F., et al., 2021, *MNRAS*, **500**, 432
- Astropy Collaboration et al., 2013, *A&A*, **558**, A33
- Axelrod T., Kantor J., Lupton R. H., Pierfederici F., 2010, in Software and Cyberinfrastructure for Astronomy. p. 774015, doi:10.1117/12.857297
- Barbary Boone Deil 2015, sep: v0.3.0, doi:10.5281/zenodo.15669, <http://dx.doi.org/10.5281/zenodo.15669>
- Baxter E. J., et al., 2018, *MNRAS*, **476**, 2674
- Becker M. R., Kravtsov A. V., 2011, *ApJ*, **740**, 25
- Behroozi P. S., Wechsler R. H., Conroy C., 2013, *ApJ*, **770**, 57
- Behroozi P., Wechsler R., Hearin A., Conroy C., 2018, preprint, ([arXiv:1806.07893](https://arxiv.org/abs/1806.07893))
- Benson B. A., et al., 2013, *ApJ*, **763**, 147
- Bernardi M., Meert A., Sheth R. K., Vikram V., Huertas-Company M., Mei S., Shankar F., 2013, *MNRAS*, **436**, 697
- Bocquet S., et al., 2019, *ApJ*, **878**, 55
- Bosch J., et al., 2017, preprint, ([arXiv:1705.06766](https://arxiv.org/abs/1705.06766))
- Bradshaw C., Leauthaud A., Hearin A., Huang S., Behroozi P., 2020, *MNRAS*, **493**, 337
- Bryan G. L., Norman M. L., 1998, *ApJ*, **495**, 80
- Busch P., White S. D. M., 2017, *MNRAS*, **470**, 4767
- Cappellari M., et al., 2013, *MNRAS*, **432**, 1862
- Chabrier G., 2003, *PASP*, **115**, 763
- Chang C., et al., 2018, *ApJ*, **864**, 83
- Chiu I.-N., Okumura T., Oguri M., Agrawal A., Umetsu K., Lin Y.-T., 2020a, arXiv e-prints, p. [arXiv:2005.13564](https://arxiv.org/abs/2005.13564)
- Chiu I. N., Umetsu K., Murata R., Medezinski E., Oguri M., 2020b, *MNRAS*, **495**, 428
- Cohn J. D., Evrard A. E., White M., Croton D., Ellingson E., 2007, *MNRAS*, **382**, 1738
- Costanzi M., et al., 2019, *MNRAS*, **482**, 490
- Coupon J., Czakon N., Bosch J., Komiyama Y., Medezinski E., Miyazaki S., Oguri M., 2017, preprint, ([arXiv:1705.00622](https://arxiv.org/abs/1705.00622))
- DES Collaboration et al., 2021, arXiv e-prints, p. [arXiv:2101.05765](https://arxiv.org/abs/2101.05765)
- DESI Collaboration et al., 2016, arXiv e-prints, p. [arXiv:1611.00036](https://arxiv.org/abs/1611.00036)
- Dark Energy Survey Collaboration et al., 2016, *MNRAS*, **460**, 1270
- DeRose J., et al., 2019, arXiv e-prints, p. [arXiv:1901.02401](https://arxiv.org/abs/1901.02401)
- DeRose J., et al., 2021, arXiv e-prints, p. [arXiv:2105.13547](https://arxiv.org/abs/2105.13547)
- Dey A., et al., 2019, *AJ*, **157**, 168
- Diemer B., 2015, Colossus: COsmology, haLO, and large-Scale StrUcture toolS, Astrophysics Source Code Library (ascl:1501.016)
- Diemer B., Kravtsov A. V., 2014, *ApJ*, **789**, 1
- Dietrich J. P., et al., 2014, *MNRAS*, **443**, 1713
- Dvornik A., et al., 2020, *A&A*, **642**, A83
- Erickson B. M. S., Cunha C. E., Evrard A. E., 2011, *Phys. Rev. D*, **84**, 103506
- Evrard A. E., 1989, *ApJ*, **341**, L71
- Evrard A. E., Arnault P., Huterer D., Farahi A., 2014, *MNRAS*, **441**, 3562–3569
- Farahi A., Evrard A. E., Rozo E., Rykoff E. S., Wechsler R. H., 2016, *MNRAS*, **460**, 3900
- Farahi A., Evrard A. E., McCarthy I., Barnes D. J., Kay S. T., 2018, *Monthly Notices of the Royal Astronomical Society*, **478**, 2618–2632
- Furnell K. E., et al., 2021, *MNRAS*, **502**, 2419
- Gladders M. D., Yee H. K. C., 2000, *AJ*, **120**, 2148
- Golden-Marx J. B., Miller C. J., 2019, *ApJ*, **878**, 14
- Grandis S., Mohr J. J., Dietrich J. P., Bocquet S., Saro A., Klein M., Paulus M., Capasso R., 2019, *MNRAS*, **488**, 2041
- Gu M., Conroy C., Behroozi P., 2016, *ApJ*, **833**, 2
- Haiman Z., Mohr J. J., Holder G. P., 2001, *ApJ*, **553**, 545
- Hamana T., et al., 2020, *PASJ*, **72**, 16
- Hao J., et al., 2010, *ApJS*, **191**, 254
- Hearin A. P., et al., 2017, *AJ*, **154**, 190
- Hearin A., Korytov D., Kovacs E., Benson A., Aung H., Bradshaw C., Campbell D., LSST Dark Energy Science Collaboration 2020, *MNRAS*, **495**, 5040
- Herbonnet R., von der Linden A., Allen S. W., Mantz A. B., Modumudi P., Morris R. G., Kelly P. L., 2019, *MNRAS*, **490**, 4889
- Hikage C., et al., 2019, *PASJ*, **71**, 43
- Hirata C., Seljak U., 2003, *MNRAS*, **343**, 459
- Holder G., Haiman Z., Mohr J. J., 2001, *ApJ*, **560**, L111
- Huang S., et al., 2018a, preprint, ([arXiv:1803.02824](https://arxiv.org/abs/1803.02824))
- Huang S., et al., 2018b, *PASJ*, **70**, S6
- Huang S., Leauthaud A., Greene J. E., Bundy K., Lin Y.-T., Tanaka M., Miyazaki S., Komiyama Y., 2018c, *MNRAS*, **475**, 3348
- Huang S., et al., 2020, *MNRAS*, **492**, 3685
- Hunter J. D., 2007, *Computing In Science & Engineering*, **9**, 90
- Jones E., Oliphant T., Peterson P., et al., 2001, SciPy: Open source scientific tools for Python, <http://www.scipy.org/>
- Jurić M., et al., 2015, preprint, ([arXiv:1512.07914](https://arxiv.org/abs/1512.07914))
- Kepner J., Fan X., Bahcall N., Gunn J., Lupton R., Xu G., 1999, *ApJ*, **517**, 78
- Kluge M., et al., 2020, *ApJS*, **247**, 43
- Kluge M., Bender R., Riffeser A., Goessl C., Hopp U., Schmidt M., Ries C., 2021, *ApJS*, **252**, 27
- Klypin A., Yepes G., Gottlöber S., Prada F., Heß S., 2016, *MNRAS*, **457**, 4340
- Koester B. P., et al., 2007, *ApJ*, **660**, 239
- Korytov D., et al., 2019, *ApJS*, **245**, 26
- Kravtsov A. V., Borgani S., 2012, *ARA&A*, **50**, 353
- Kravtsov A. V., Vikhlinin A. A., Meshcheryakov A. V., 2018, *Astronomy Letters*, **44**, 8
- Lackner C. N., Cen R., Ostriker J. P., Joung M. R., 2012, *MNRAS*, **425**, 641
- Lange J. U., Yang X., Guo H., Luo W., van den Bosch F. C., 2019, *MNRAS*, **488**, 5771

- Leauthaud A., et al., 2010, *ApJ*, 709, 97
- Leauthaud A., et al., 2012, *ApJ*, 744, 159
- Leauthaud A., et al., 2017, *MNRAS*, 467, 3024
- Lehmann B. V., Mao Y.-Y., Becker M. R., Skillman S. W., Wechsler R. H., 2017, *ApJ*, 834, 37
- Li R., et al., 2014, *MNRAS*, 438, 2864
- Li R., et al., 2016a, *MNRAS*, 458, 2573
- Li R., et al., 2016b, *MNRAS*, 458, 2573
- Lieu M., et al., 2016, *A&A*, 592, A4
- Mandelbaum R., et al., 2008, *MNRAS*, 386, 781
- Mandelbaum R., et al., 2017, preprint, ([arXiv:1710.00885](https://arxiv.org/abs/1710.00885))
- Mandelbaum R., et al., 2018, *PASJ*, 70, S25
- Mantz A. B., Allen S. W., Morris R. G., Rapetti D. A., Applegate D. E., Kelly P. L., von der Linden A., Schmidt R. W., 2014, *MNRAS*, 440, 2077
- Mantz A. B., et al., 2016, *MNRAS*, 463, 3582
- Matthee J., Schaye J., Crain R. A., Schaller M., Bower R., Theuns T., 2017, *MNRAS*, 465, 2381
- McClintock T., et al., 2019, *MNRAS*, 482, 1352
- Melchior P., et al., 2017, *MNRAS*, 469, 4899
- Miyatake H., More S., Takada M., Spergel D. N., Mandelbaum R., Rykoff E. S., Rozo E., 2016, *Phys. Rev. Lett.*, 116, 041301
- Miyazaki S., et al., 2012, in *Ground-based and Airborne Instrumentation for Astronomy IV*. p. 84460Z, [doi:10.1117/12.926844](https://doi.org/10.1117/12.926844)
- Montes M., Trujillo I., 2018, *MNRAS*, 474, 917
- Montes M., Trujillo I., 2019, *MNRAS*, 482, 2838
- Montes M., Brough S., Owers M. S., Santucci G., 2021, arXiv e-prints, p. [arXiv:2101.08290](https://arxiv.org/abs/2101.08290)
- More S., van den Bosch F. C., Cacciato M., Mo H. J., Yang X., Li R., 2009, *MNRAS*, 392, 801
- More S., van den Bosch F. C., Cacciato M., Skibba R., Mo H. J., Yang X., 2011, *MNRAS*, 410, 210
- More S., Diemer B., Kravtsov A. V., 2015, *ApJ*, 810, 36
- More S., et al., 2016, *ApJ*, 825, 39
- Moster B. P., Naab T., White S. D. M., 2018, *MNRAS*, 477, 1822
- Moster B. P., Naab T., White S. D. M., 2020, *MNRAS*, 499, 4748
- Moustakas J., et al., 2013, *ApJ*, 767, 50
- Murata R., Nishimichi T., Takada M., Miyatake H., Shirasaki M., More S., Takahashi R., Osato K., 2018, *ApJ*, 854, 120
- Murata R., et al., 2019, *PASJ*, 71, 107
- Nakajima R., Mandelbaum R., Seljak U., Cohn J. D., Reyes R., Cool R., 2012, *MNRAS*, 420, 3240
- Nelson D., et al., 2018, *MNRAS*, 475, 624
- Noh Y., Cohn J. D., 2012, *MNRAS*, 426, 1829
- Oguri M., 2014, *MNRAS*, 444, 147
- Oguri M., et al., 2018, *PASJ*, 70, S20
- Okabe N., Smith G. P., 2016, *MNRAS*, 461, 3794
- Osato K., Nishimichi T., Oguri M., Takada M., Okumura T., 2018, *MNRAS*, 477, 2141
- Oser L., Ostriker J. P., Naab T., Johansson P. H., Burkert A., 2010, *ApJ*, 725, 2312
- Pedregosa F., et al., 2011, *Journal of Machine Learning Research*, 12, 2825
- Peebles P. J. E., Daly R. A., Juszkwieicz R., 1989, *ApJ*, 347, 563
- Pérez F., Granger B. E., 2007, *Computing in Science and Engineering*, 9, 21
- Pillepich A., et al., 2018, *MNRAS*, 475, 648
- Planck Collaboration et al., 2020, *A&A*, 641, A6
- Pulsoni C., Gerhard O., Arnaboldi M., Pillepich A., Rodríguez-Gomez V., Nelson D., Hernquist L., Springel V., 2021, *A&A*, 647, A95
- Reddick R. M., Wechsler R. H., Tinker J. L., Behroozi P. S., 2013, *ApJ*, 771, 30
- Reid B. A., Seo H.-J., Leauthaud A., Tinker J. L., White M., 2014, *MNRAS*, 444, 476
- Reyes R., Mandelbaum R., Hirata C., Bahcall N., Seljak U., 2008, *MNRAS*, 390, 1157
- Rodríguez-Gomez V., et al., 2016, *MNRAS*, 458, 2371
- Rodríguez-Puebla A., Primack J. R., Avila-Reese V., Faber S. M., 2017, *MNRAS*, 470, 651
- Román J., Trujillo I., Montes M., 2020, *A&A*, 644, A42
- Rozo E., Rykoff E. S., 2014, *ApJ*, 783, 80
- Rozo E., et al., 2009, *ApJ*, 703, 601
- Rozo E., et al., 2010, *ApJ*, 708, 645
- Rozo E., Rykoff E. S., Bartlett J. G., Melin J.-B., 2015a, *MNRAS*, 450, 592
- Rozo E., Rykoff E. S., Becker M., Reddick R. M., Wechsler R. H., 2015b, *MNRAS*, 453, 38
- Rykoff E. S., et al., 2012, *ApJ*, 746, 178
- Rykoff E. S., et al., 2014, *ApJ*, 785, 104
- Rykoff E. S., et al., 2016, *ApJS*, 224, 1
- Saito S., et al., 2016, *MNRAS*, 460, 1457
- Sampaio-Santos H., et al., 2021, *MNRAS*, 501, 1300
- Saro A., et al., 2015, *MNRAS*, 454, 2305
- Shin T., et al., 2019, *MNRAS*, 487, 2900
- Sifón C., et al., 2015, *MNRAS*, 454, 3938
- Sifón C., Herbonnet R., Hoekstra H., van der Burg R. F. J., Viola M., 2018, *MNRAS*, 478, 1244
- Simet M., McClintock T., Mandelbaum R., Rozo E., Rykoff E., Sheldon E., Wechsler R. H., 2017, *MNRAS*, 466, 3103
- Singh S., Mandelbaum R., Seljak U., Slosar A., Vazquez Gonzalez J., 2017, *MNRAS*, 471, 3827
- Speagle J. S., et al., 2019, *MNRAS*, 490, 5658
- Sunayama T., More S., 2019, *MNRAS*, 490, 4945
- Sunayama T., et al., 2020, *MNRAS*, 496, 4468
- Tanaka M., et al., 2018, *PASJ*, 70, S9
- Tinker J. L., 2017, *MNRAS*, 467, 3533
- Tinker J., Kravtsov A. V., Klypin A., Abazajian K., Warren M., Yepes G., Gottlöber S., Holz D. E., 2008, *ApJ*, 688, 709–728
- Tinker J. L., George M. R., Leauthaud A., Bundy K., Finoguenov A., Massey R., Rhodes J., Wechsler R. H., 2012, *ApJ*, 755, L5
- Tinker J. L., et al., 2017, *ApJ*, 839, 121
- To C., et al., 2021a, *Phys. Rev. Lett.*, 126, 141301
- To C.-H., et al., 2021b, *MNRAS*, 502, 4093
- Tomooka P., Rozo E., Wagoner E. L., Aung H., Nagai D., Saionova S., 2020, *MNRAS*, 499, 1291
- Trayford J. W., et al., 2015, *MNRAS*, 452, 2879
- Trayford J. W., et al., 2017, *MNRAS*, 470, 771
- Umetsu K., 2020, *A&ARv*, 28, 7
- Umetsu K., et al., 2020, *ApJ*, 890, 148
- Viana P. T. P., Liddle A. R., 1996, *MNRAS*, 281, 323
- Vikhlinin A., et al., 2009, *ApJ*, 692, 1060
- Wagoner E. L., Rozo E., Aung H., Nagai D., 2021, *MNRAS*, 504, 1619
- Walt S. v. d., Colbert S. C., Varoquaux G., 2011, *Computing in Science and Engg.*, 13, 22
- Wang L., Steinhardt P. J., 1998, *ApJ*, 508, 483
- Wang W., et al., 2019, *MNRAS*, 487, 1580
- Wechsler R. H., Tinker J. L., 2018, preprint, ([arXiv:1804.03097](https://arxiv.org/abs/1804.03097))
- Weinberg D. H., Mortonson M. J., Eisenstein D. J., Hirata C., Riess A. G., Rozo E., 2013, *Phys. Rep.*, 530, 87
- Wen Z. L., Han J. L., 2021, *MNRAS*, 500, 1003
- Wen Z. L., Han J. L., Liu F. S., 2012, *ApJS*, 199, 34
- White S. D. M., Efstathiou G., Frenk C. S., 1993, *MNRAS*, 262, 1023
- Wu H.-Y., Weinberg D. H., Salcedo A. N., Wibking B. D., 2021, *ApJ*, 910, 28
- Khakaj E., Diemer B., Leauthaud A., Wasserman A., Huang S., Luo Y., Adhikari S., Singh S., 2020, *MNRAS*, 499, 3534
- Yang X., et al., 2020, arXiv e-prints, p. [arXiv:2012.14998](https://arxiv.org/abs/2012.14998)
- York D. G., et al., 2000, *AJ*, 120, 1579
- Zhang Y., et al., 2019a, *MNRAS*, 487, 2578
- Zhang Y., et al., 2019b, *ApJ*, 874, 165
- Ziparo F., et al., 2016, *A&A*, 592, A9
- Zou H., et al., 2021, arXiv e-prints, p. [arXiv:2101.12340](https://arxiv.org/abs/2101.12340)

- Zu Y., Mandelbaum R., 2015, *MNRAS*, **454**, 1161
 Zu Y., Mandelbaum R., Simet M., Rozo E., Rykoff E. S., 2017, *MNRAS*, **470**, 551
 Zürcher D., More S., 2019, *ApJ*, **874**, 184
 van Dokkum P. G., et al., 2010, *ApJ*, **709**, 1018
 van Uitert E., et al., 2016, *MNRAS*, **459**, 3251
 von der Linden A., et al., 2014, *MNRAS*, **439**, 2

APPENDIX A: DERIVATION OF THE GALAXY–GALAXY LENSING PROFILES

Here we walk through the derivation of the final $\Delta\Sigma$ profile used in the Top- N test. As mentioned in § 4.2, we adopt a slightly modified version of the methodology from Singh et al. (2017) to measure the excess surface mass density (ESD or $\Delta\Sigma$) profiles around massive galaxies or clusters. This method emphasises the importance of subtracting lensing signals around large number of random positions from the signals for real lenses to achieve unbiased measurement. The $\Delta\Sigma$ signal at a physical radius R is:

$$\Delta\Sigma_{LR}(R) = f_{\text{bias}}(\Delta\Sigma_L(R) - \Delta\Sigma_R(R)) \quad (\text{A1})$$

Here, L indicates measurements for the lens galaxies while R is for random positions. For each $\Delta\Sigma$ profile, we use a set of 1.5×10^5 random points whose redshift distribution is matched to the lenses. The number of random points is at least 100 time larger than the largest Top- N sample. The $\Delta\Sigma$ profile around lenses is:

$$\Delta\Sigma_L(R) = \frac{1}{2\mathcal{R}(R)[1 + \mathcal{K}(R)]} \frac{\sum_{L_s} w_{L_s} \gamma_t^{(L_s)} \Sigma_{\text{crit}}^{(L_s)}}{\sum_{L_s} w_{L_s}} \quad (\text{A2})$$

where γ_t is the tangential shear component, Σ_{crit} is the critical surface density, w_{L_s} is the weight used for each lens-source pair. Following the calibration strategy outlined in Mandelbaum et al. (2017), we also include the shear responsivity factor $\mathcal{R}(R)$ and the correction for the multiplicative shear bias $[1 + \mathcal{K}(R)]$. Here Σ_{L_s} represents the summation over all lens-source pairs. We perform the same measurements for random points, so replacing L with R in Equation A2 will form the estimator for randoms.

The critical surface density is:

$$\Sigma_{\text{crit}} = \frac{c^2}{4\pi G} \frac{D_A(z_s)}{D_A(z_l)D_A(z_l, z_s)(1 + z_l)^2} \quad (\text{A3})$$

where $D_A(z_l)$, $D_A(z_s)$, and $D_A(z_l, z_s)$ represent the angular diameter distances to the lens, source, and the distance between the lens-source pair.

The weight applied to each lens-source pair is described by:

$$w_{L_s} = \frac{\Sigma_{\text{crit}}^{-2}}{\sigma_{e, L_s}^2 + \sigma_{\text{rms}}^2} \equiv \frac{\Sigma_{\text{crit}}^{-2}}{\sigma_{L_s}^2} \quad (\text{A4})$$

where σ_{rms} represents the intrinsic shape dispersion while σ_{e, L_s} is the per-component shape measurement error.

Meanwhile, the shear responsivity factor is defined by:

$$\mathcal{R}(R) = 1 - \frac{\sum_{L_s} w_{L_s} \sigma_{e, L_s}^2}{\sum_{L_s} w_{L_s}} \quad (\text{A5})$$

And the multiplicative shear bias correction is defined as:

$$\mathcal{K}(R) = \frac{\sum_{L_s} w_{L_s} m_s}{\sum_{L_s} w_{L_s}} \quad (\text{A6})$$

where m_s is multiplicative shear bias value for each source. The shape catalogue provides estimates of σ_{rms} , σ_{e, L_s} , and m_s , while Mandelbaum et al. (2017) provides in-depth discussion of these calibration related issues.

In difference with Singh et al. (2017), we do not use boost factor to account for the photo- z dilution effect. Following the strategy in Leauthaud et al. (2017), we develop a correction factor, f_{bias} , to account for it. We define f_{bias} as the ratio between the $\Delta\Sigma$ profile calculated using the real redshift and the one using photo- z from the COSMOS photo- z calibration catalogue³².

In practice, it is estimated based on:

$$f_{\text{bias}} = \frac{\sum_{L_s} w_{L_s} w_{\text{sys}} (\Sigma_{\text{crit, T}} / \Sigma_{\text{crit, P}})}{\sum_{L_s} w_{L_s} w_{\text{sys}}} \quad (\text{A7})$$

based on the photo- z calibration sample in the COSMOS field for such purpose (e.g., Mandelbaum et al. 2008; Nakajima et al. 2012; Leauthaud et al. 2017).

As for the f_{bias} , where $\Sigma_{\text{crit, T}}$ is the critical surface density estimated using the “true” redshift in the calibration catalogue (can be spec- z or COSMOS 30-band photo- z), while $\Sigma_{\text{crit, P}}$ is the one using frankenz photo- z . w_{sys} is the systematic photo- z weight in the calibration catalogue that matches the colour-magnitude distribution of the COSMOS photo- z calibration catalogue to the same distribution of the source catalogue (e.g., Mandelbaum et al. 2008; Nakajima et al. 2012). Note that the estimator shown here is different from the ones in Leauthaud et al. (2017) and Speagle et al. (2019), and it accounts for the photo- z dilution effect more accurately. The f_{bias} level for galaxies in our sample is general very low (~ 1 -2%).

To estimate the covariance matrix of a $\Delta\Sigma$ profile, we use both jackknife and bootstrap resampling method. For the jackknife case, we assign lens and randoms into the same 45 jackknife regions with similar area around 2.5 deg^2 and regular shapes. The covariance matrix from the jackknife resampling is:

$$\text{Var}_{\text{Jk}}(\widehat{\Delta\Sigma}) = \frac{N_{\text{Jk}} - 1}{N_{\text{Jk}}} \sum_{i=1}^{N_{\text{Jk}}} (\Delta\Sigma_i - \overline{\Delta\Sigma})^2 \quad (\text{A8})$$

here $N_{\text{Jk}} = 45$, $\Delta\Sigma_i$ represents the $\Delta\Sigma$ profile from each Jackknife region, and $\overline{\Delta\Sigma}$ is the mean profile of all regions.

For the Top- N test, the small sample size in Bin 1 & 2 sometimes make it difficult to assign jackknife regions. Therefore we also calculate the covariance matrix using bootstrap resampling with $N_{\text{Bt}} = 5000$ iterations:

$$\text{Var}_{\text{Bt}}(\widehat{\Delta\Sigma}) = \frac{1}{N_{\text{Bt}} - 1} \sum_{i=1}^{N_{\text{Bt}}} (\Delta\Sigma_{i, \text{Bt}} - \overline{\Delta\Sigma})^2 \quad (\text{A9})$$

The two methods provide consistent measurements of covariance matrix.

³² <https://hsc-release.mtk.nao.ac.jp/doc/index.php/s17a-wide-cosmos/>

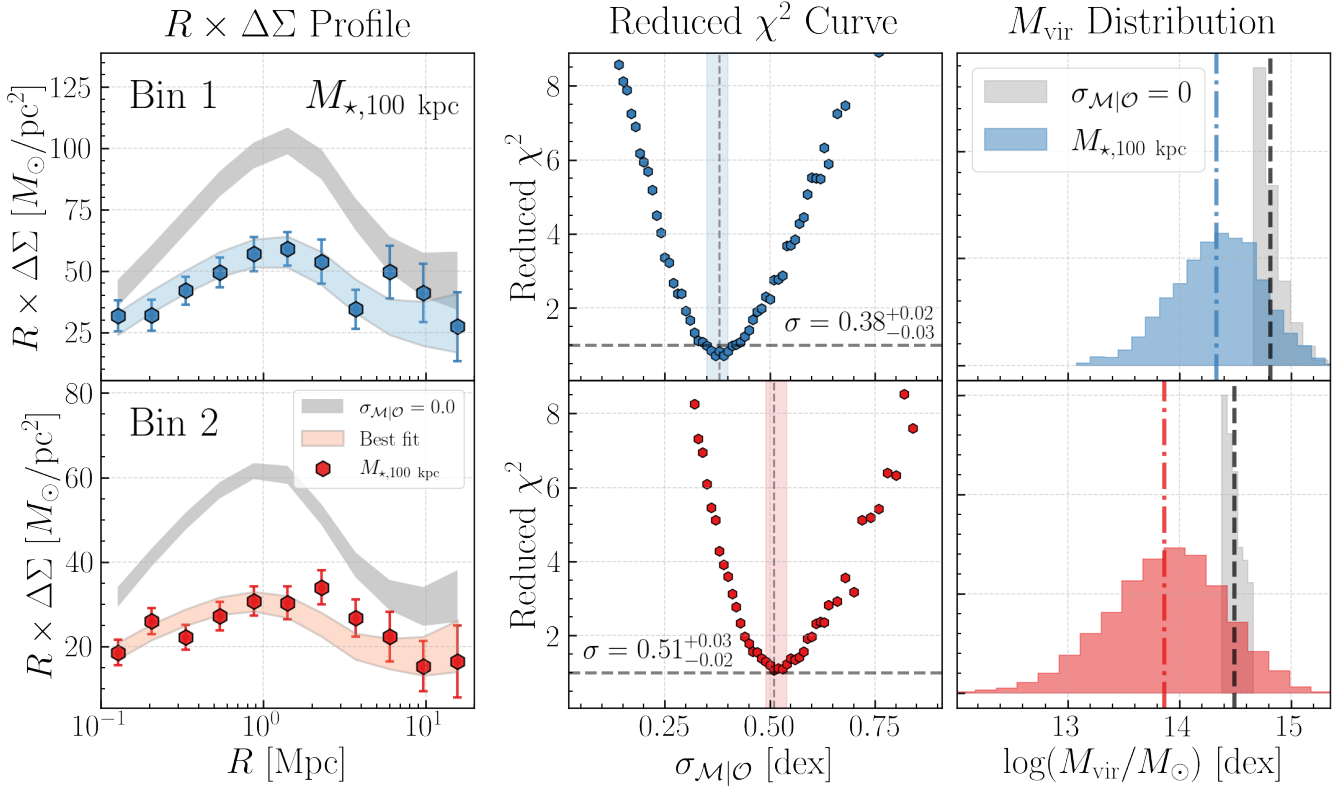


Figure A1. Illustration of the scatter-matching process in the four Top- N bins using the $M_{\star,150 \text{ kpc}}$ as an example. **Left** column shows the observed $R \times \Delta\Sigma$ profiles (solid hexagon), the best-fit profiles using MDPL2 simulation (shaded regions with similar colours), and the lensing profiles of the “perfect” Top- N sample. The uncertainties of the model lensing profiles are inflated to match the expected statistical uncertainties of the volume occupied by the HSC data. **Middle** column shows the reduced χ^2 curve of the fitting process. A horizontal dashed-line highlights where $\chi^2 = 1$. The vertical dashed-line and the shaded region show the best-fit scatter value and the associated uncertainty. We also display these values on the figure. **Right** column shows the best-fit M_{vir} distributions in each bin predicted by the MDPL2 simulation (coloured histograms; dot-dashed lines label the average M_{vir} values). We also compare them with the “true” M_{vir} distributions in each number density bin (grey histograms; grey dashed-lines label the average M_{vir} values). The **Jupyter** notebook for reproducing this figure can be found here: [🔗](#)

APPENDIX B: MATCHING THE LENSING PROFILES

As described in § 2.2.2, we estimate the $\sigma_{M_{\text{vir}}}$ value from an observed $\Delta\Sigma$ profile from the Top- N test through matching it to a densely sampled grid of model $\Delta\Sigma$ profiles that cover a wide range of $\sigma_{M_{\text{vir}}}$ values. For each pair of observed and predicted $\Delta\Sigma$ profiles, we define a simple χ^2 statistic (Equation 7) to describe the “similarity” between them.

In Figure A1, we use the Top- N result for $M_{\star,150 \text{ kpc}}$ stellar mass as example to visualise the “scatter matching” procedure, which produce a well-behaved reduced χ^2 curves with a clear minimum. For $M_{\star,150 \text{ kpc}}$, the reduced χ^2 values in all four Top- N bins are reasonably close to 1.0 ([0.65, 0.88, 1.31, 0.90]). In line with this impression, the left panels show that the best-fit “scatter only” $\Delta\Sigma$ profile is fully consistent with the observed one. As discussed in § 6.3, this is not always the case (see Figure 10). However, even when the best-fit model is not satisfying (e.g., reduced $\chi^2 > 2$), we still estimate the “best-fit” $\sigma_{M_{\text{vir}}}$ value.

Since we only calculate the χ^2 on a grid of $\sigma_{M_{\text{vir}}}$ values and the statistical uncertainties of the predicted $\Delta\Sigma$ profiles cannot be completely ignored, we did not just report the $\sigma_{M_{\text{vir}}}$ value with the lowest χ^2 . Instead, we interpo-

late the normalised cumulative distribution of the likelihood $\equiv \exp(-0.5 \times \chi^2)$ to derive the $\sigma_{M_{\text{vir}}}$ at 50th percentile as the “best-fit” scatter value. We estimate the 1- σ uncertainty range in the same way.

We should note that the choice of covariance matrix (Jackknife v.s. bootstrap) does not affect any results of this work. We also attempted to include the uncertainties of the predicted $\Delta\Sigma$ profile to the covariance matrix as additional diagonal term, and verify it has no impact on any conclusions.

In the figure, we inflate the error bars of the model profiles to reflect the volume difference between the HSC data and the simulation used. For MDPL2 simulation, the volume is about $\sim 25\times$ larger than the HSC volume. We therefore increase the error bar by a factor of 5. However, we did not include the model uncertainty during the fitting process.

APPENDIX C: SCALING RELATION MODEL CALIBRATED TO MATCH HSC OBSERVATIONS

In § 2.2.2, we describe the method to predict the stacked $\Delta\Sigma$ profile of a sample of number density selected halos with

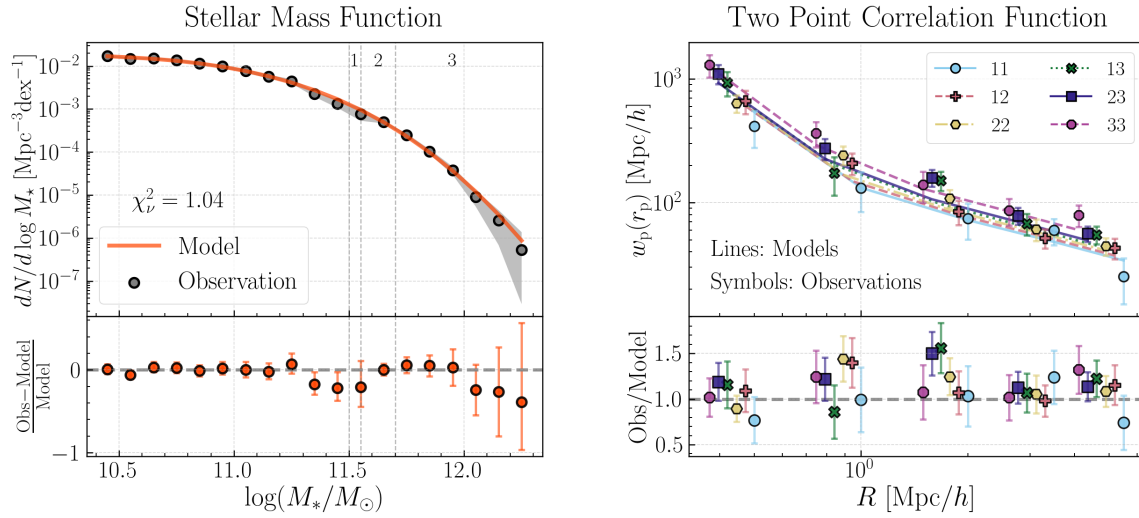


Figure C1. **Left** panels demonstrate how well the model (red line) can fit the observed SMF (grey symbols; shaded regions are uncertainties) that combines data from HSC at high- M_* end and PRIMUS survey at low- M_* end. The bottom sub-panel shows the relative residual of the best-fit SMF. The three vertical dashed-lines highlight the M_* boundaries of the three M_* -bins ($[11.50, 11.55, 11.70]$) used for measuring the two-point correlation functions of massive HSC galaxies. **Right** panels summarise the observed clustering of HSC massive galaxies (symbols) and their best-fit models (lines). [11, 22, 33] are the auto-correlation functions of the three M_* bins, while [12, 13, 23] indicate the cross-correlation functions among the three bins. The bottom sub-panel shows the ratio between the observed and the model clustering signals. The *Jupyter* notebook for reproducing this figure can be found here: [🔗](#).

certain $\sigma_{M|O}$ value based on a log-normal scaling relation with fixed slope ($\alpha = 1$). This simple model helps us predict the stacked $\Delta\Sigma$ profile of a specific Top- N bin (see Figure 2). Meanwhile, to evaluate the impact of satellite galaxies on the Top- N tests, we still need a mock catalogue from simulation that can fit basic HSC observations of massive galaxies and have realistic satellite fraction at high- M_* end.

Taking advantage of the work by (DeMartino et al. in prep.), we create such a mock catalogue that can reproduce the SMF and clustering statistics of HSC massive galaxies using a sub-halo abundance matching model (SHAM) based on peak halo mass (M_{Peak}). We also use this model to constrain the SHMR and its scatter at high- M_{vir} end. In particular, we model the SHMR using the functional form from Behroozi et al. (2013) but fixing the slope at low- M_{vir} end (β). In total, the model has five free parameters: 1. The four parameters that govern the mean SHMR at high- M_{vir} end from Behroozi et al. (2013); 2. And the scatter of M_* at fixed M_{vir} .

As shown in Figure C1, the best-fit model can reproduce the observed mass function and clustering statistics of massive galaxies reasonably well. To ensure the model can fit the SMF beyond just the high- M_* end, we adopt a “hybrid” SMF: we use the complete sample of HSC massive galaxies at $0.2 < z < 0.5$ to cover the $\log_{10}(M_*/M_\odot) > 11.5$ range, and use the PRIMUS $0.3 < z < 0.4$ SMF (Moustakas et al. 2013) for the $10.5 < \log_{10}(M_*/M_\odot) < 11.5$ range. Both the HSC and the PRIMUS M_* are from the *iSedfit* code under very similar assumptions of stellar population properties. The M_* of the HSC sample is based on our customised 1-D profile that capture the luminosity beyond 100 kpc, while the PRIMUS sample is based on small aperture photometry. Using the PRIMUS galaxies that also have the HSC 1-D M_* measurements from Huang et al. (2018c), we derive a simple constant offset term that help us “stitch” the two SMFs to-

gether. We note that this just ensures a smooth SMF for the fitting, and does not affect any results in this work. As for the clustering signals of HSC massive galaxies, we compute the auto- and cross-correlation signals after separating the sample into three M_* bins: $11.50 < \log_{10}(M_*/M_\odot) \leq 11.55$, $11.55 < \log_{10}(M_*/M_\odot) \leq 11.70$, and $\log_{10}(M_*/M_\odot) > 11.70$. The best-fit SHMR is broadly consistent with previous works including the scatter of M_* value (~ 0.2 dex). More importantly, the satellite fraction at high- M_* end is between 5 and 10%, which is also similar to the results of previous works. We also verify that the satellite fraction value is robust to small changes in abundance matching methodology.

APPENDIX D: $\Delta\Sigma$ PROFILES OF MASSIVE SATELLITE GALAXIES

In § 6.1, we introduced our method for identifying candidates of massive satellite galaxies from our sample and investigated their impacts on the stacked $\Delta\Sigma$ profile. In Figure D1, we compare the stacked $\Delta\Sigma$ profiles of massive satellite galaxies within $11.6 < \log(M_{*,100 \text{ kpc}}/M_\odot) < 11.8$ to that of the central galaxies in the same M_* bin. As explained in § 6.1, for massive galaxies in our sample, we iteratively identify satellite galaxies with lower $M_{*,10 \text{ kpc}}$ in a cylinder with radius $R = 1$ Mpc and LOS length of $L = 40$ Mpc. We ignore the redshift and M_* uncertainties during this procedure, so strictly speaking these are just candidates of satellite galaxies. Within the $M_{*,100 \text{ kpc}}$ bin, we find 161 massive satellite galaxies and 1804 central galaxies. The $M_{*,100 \text{ kpc}}$ distribution of satellite clearly skews toward lower values than the one for centrals. To make it a fair comparison, we match the centrals to satellites in the 2-D $M_{*,50 \text{ kpc}} - M_{*,[50,100]}$ plane: using a k-d tree, we search for the nearest 7 centrals around each satellite and keep the unique cen-

trals. This yield 765 central galaxies with similar $M_{\star,100 \text{ kpc}}$ and $M_{\star,50 \text{ kpc}}-M_{\star,[50,100]}$ distributions to the satellites. They also share very similar redshift distributions. In the top panel of Figure D1, we compare their $\Delta\Sigma$ profiles. While the centrals and satellites share similar profiles within inner 500 kpc, the satellites display clearly enhanced $\Delta\Sigma$ signals at $R > 1$ Mpc. We highlight this result in the bottom panel of Figure D1 using the ratio of the satellite $\Delta\Sigma$ profile to that of the centrals. We also show the ratios for satellites selected using different cylinders. This comparison shows that small variation of the radius (from 1.0 to 1.5 Mpc) and length (20 to 40 Mpc) of the cylinders will not affect the results.

Figure D1 shows that, at the same M_{\star} , massive satellite galaxies show very different $\Delta\Sigma$ profiles with centrals due to the strong impact from their host dark matter halos. Despite the small impact on the stacked $\Delta\Sigma$ profiles due to the low satellite fraction value, the $\Delta\Sigma$ profile of massive satellite galaxies alone contains valuable information about the galaxy–halo connection of massive galaxies (*e.g.*, Sifón et al. 2015; Li et al. 2016b; Dvornik et al. 2020). We will aim to understand it more so that we can deal with satellites better when using M_{\star} -based M_{vir} proxies.

APPENDIX E: GALAXY SIZE AS M_{vir} INDICATOR

In this work, we have explored different aperture and outskirts stellar mass defined using fixed physical radius (*e.g.*, 100 kpc, 50 to 100 kpc). They provide unambiguous definitions of apertures, which is important when comparing results from different imaging data or between simulation and observation. But, for galaxies with very different size, M_{\star} defined using fixed radius could have very different physical meanings. For example, while $M_{\star,[50,100]}$ is a good measurement of outer envelope M_{\star} for very massive elliptical galaxies, it is not even practical to apply it to Milky Way-mass galaxies.

The half-light (-mass) radius (R_{50}), or the effective radius (R_e), is a commonly adopted galaxy size measurement. It naturally provides another way to define aperture and outskirts for galaxies. In Figure E1, we summarise the Top- N results for a few different aperture (top panel) and outskirts (bottom panel) M_{\star} . In this work, the R_{50} is measured using the *i*-band integrated 1-D intensity profiles (also known as the curve-of-growth) along the major axis (so it is not “circulized”). It is defined as the radius that contains 50% of light within 100 kpc radius. We choose this definition because the surface brightness profile at $R > 100$ kpc becomes less reliable, but replacing 100 kpc with larger radius such as 150 kpc will not change our results.

Aperture M_{\star} defined using R_{50} show similar performance with $M_{\star,100 \text{ kpc}}$. This is expected for $M_{\star,R_{50}}$ as it represents 50% of $M_{\star,100 \text{ kpc}}$ by definition. Meanwhile, none of the other larger aperture masses using R_{50} show any improvement. Outskirt masses using R_{50} do have lower $\sigma_{M_{\text{vir}}}$ values than $M_{\star,100 \text{ kpc}}$. While this confirms the result using fixed radius, none of the outskirts M_{\star} using R_{50} has performance as good as $M_{\star,[50,100]}$ especially in Bin 3 & 4.

We note that the stellar masses defined by R_{50} directly ties to the measurement of galaxy size, which is not an easy task. Replacing the R_{50} from 1-D curve-of-growth with the R_e from single Sérsic fitting could lead to different results.

Satellites v.s. Centrals

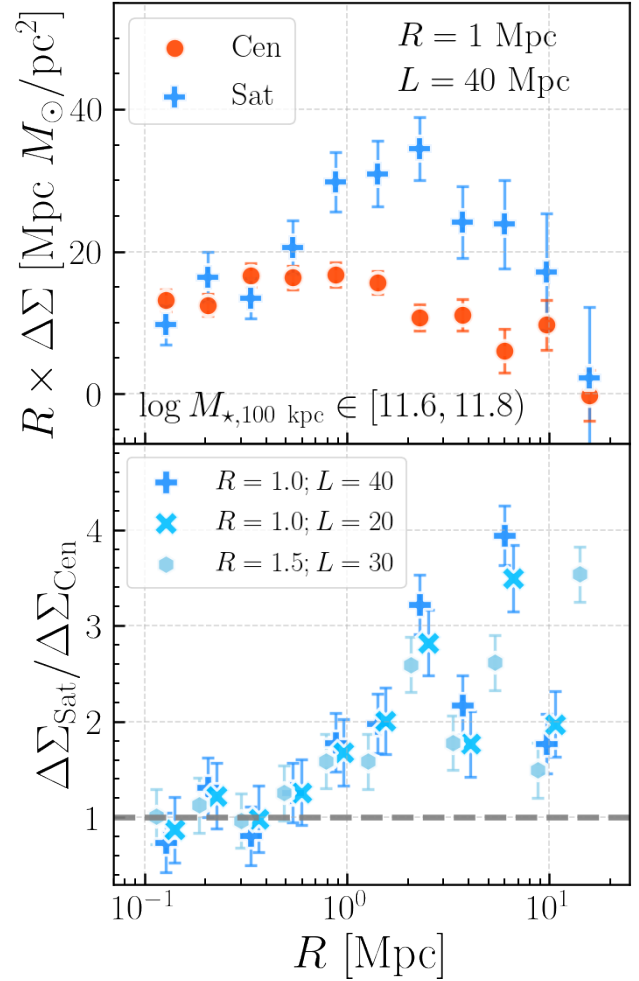


Figure D1. The comparison of $\Delta\Sigma$ profiles of centrals and satellites at similar M_{\star} . **Top panel:** Blue crosses show the $\Delta\Sigma$ profile of satellites within $11.6 < \log(M_{\star,100 \text{ kpc}}/M_{\odot}) < 11.8$ selected using a cylinder with $R = 1$ Mpc and $L = 40$ Mpc. The red circles show the $\Delta\Sigma$ profile for a sample of central galaxies with matched M_{\star} distributions. **Bottom panel** shows the ratios of the stacked $\Delta\Sigma$ profiles for satellites and centrals selected using different definitions of cylinders. The **Jupyter** notebook for reproducing this figure can be found here: [🔗](#).

We will explore more M_{vir} proxies related to galaxy size in future works.

APPENDIX F: THE COMPARISON OF $\Delta\Sigma$ PROFILE BETWEEN THE HSC AND SDSS redMaPPer CLUSTERS

In Figure F1, we compare the $\Delta\Sigma$ profiles of redMaPPer clusters from SDSS survey to those of HSC data, and also to the HSC massive galaxies selected using $M_{\star,[50,100]}$. We are using the **v6.3 catalogue for SDSS DR8**. While the SDSS images are much shallower than HSC, they also suffer less from the over-deblending issue that affects the red–sequence cluster finders using deeper data. The *u*-band image could also help improve the red–sequence redshift of low redshift clusters.

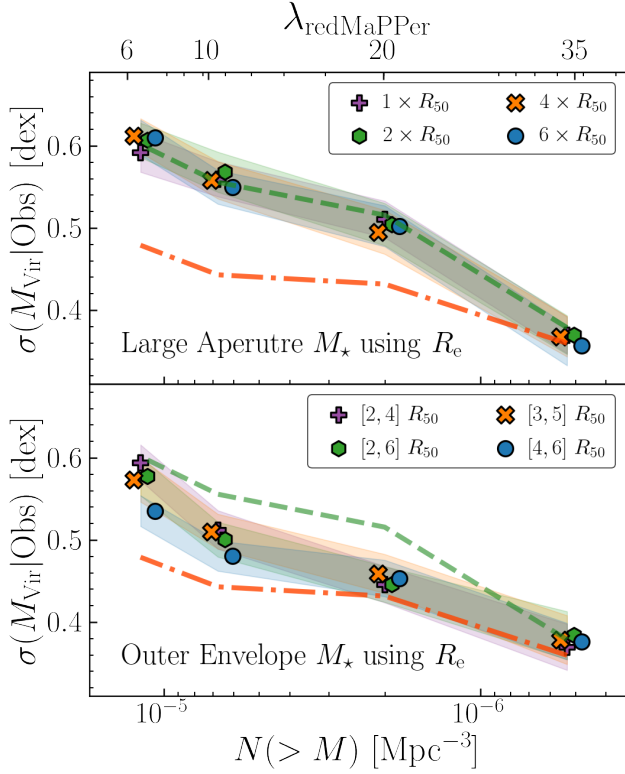


Figure E1. The relations between the cumulative number density of each Top- N bin and $\sigma_{M_{\text{vir}}}$ for M_* -based M_{vir} proxies defined using R_{50} . The format is the same with Figure 8 and Figure 5. **Top** panel shows the Top- N results for different aperture M_* defined using R_{50} while the **bottom** panel is for different outskirts M_* defined using R_{50} . We use the $\sigma_{M_{\text{vir}}}$ trends for $M_{*,100}$ kpc (green dashed line) and $M_{*,[50,100]}$ (red dot-dashed line) as the references. The **Jupyter** notebook for reproducing this figure can be found here: [🔗](#).

Given the redshift coverage and richness completeness of SDSS **redMaPPer**, we do not have enough objects to perform Top- N tests except for Bin 1. We therefore define two SDSS **redMaPPer** samples for our comparison: 1) 55 clusters in $0.19 < z < 0.50$ and $\lambda_{\text{SDSS}} \geq 50$ (top panel of Figure F1; 2) 191 clusters in $0.19 < z < 0.35$ and $\lambda_{\text{SDSS}} \geq 20$ (bottom panel). We then use the same redshift bins and number density to select HSC **redMaPPer** clusters and massive galaxies.

In Figure F1, we show that the $\Delta\Sigma$ profiles of SDSS **redMaPPer** clusters are not only consistent with the HSC **redMaPPer** ones, they also display very similar systematic differences with the $M_{*,[50,100]}$ -selected massive galaxies. This reinforces our conclusions in § 6.3 and § 6.2.5.

APPENDIX G: THE COMPARISON OF $\Delta\Sigma$ PROFILE BETWEEN THE HSC AND DES **redMaPPer** CLUSTER

The Dark Energy Survey (DES) has adopted the **redMaPPer** algorithm for finding galaxy clusters (*e.g.*, Rykoff et al. 2016). It would be interesting to compare the lensing profiles of HSC and DES **redMaPPer** clusters. Since the overlapping area between DES Y1 and HSC S16A is very small, here we directly compare the stacked $\Delta\Sigma$ profile of DES **redMaPPer** clusters at $0.20 \leq z < 0.55$ and $20 \leq \lambda_{\text{DES}} < 100$ presented

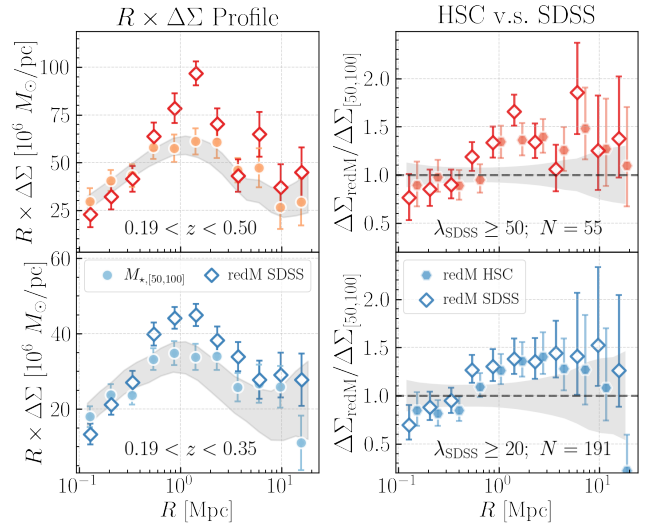


Figure F1. Similar to Figure 9, here we compare the $\Delta\Sigma$ profiles of SDSS **redMaPPer** clusters (empty diamonds) to those of HSC **redMaPPer** clusters (solid hexagons) and $M_{*,[50,100]}$ -selected HSC massive galaxies (solid circles). Given the completeness of SDSS **redMaPPer** clusters, we show the comparison in two richness and redshift bins: **top** panel is for $\lambda_{\text{SDSS}} \geq 50$ clusters at $0.2 < z < 0.5$ while the **bottom** panel is for $\lambda_{\text{SDSS}} \geq 20$ clusters at $0.2 < z < 0.35$. **Left** panels show the comparisons of lensing profiles. The shaded regions display the best-fit model profile of the $M_{*,[50,100]}$ samples. **Right** panels show the ratio of $\Delta\Sigma$ profiles between richness- and $M_{*,[50,100]}$ -selected samples. The SDSS **redMaPPer** clusters' $\Delta\Sigma$ profiles show similar systematic differences with the $M_{*,[50,100]}$ profile just like their HSC counterparts. The **Jupyter** notebook for reproducing this figure can be found here: [🔗](#).

in Chang et al. (2018) to their HSC counterparts. We ignore the small offset between richness measurements using different data and select 285 HSC **redMaPPer** clusters in the same richness and redshift bin. This roughly corresponds to the combination of the Bin 1 & 2 in our Top- N tests. In Chang et al. (2018), the authors adopted the same cosmology but use comoving coordinates instead. Therefore we calculate a new $\Delta\Sigma$ profile for HSC clusters using comoving coordinates as well.

Figure G1 shows that the $\Delta\Sigma$ profiles for HSC and DES **redMaPPer** clusters are broadly consistent with each other. Note that the DES $\Delta\Sigma$ profile is based on an completely independent lensing catalogue using different algorithms for shear measurement, lensing calibration, and photo- z estimation. While the two profiles show subtle difference at $1 < R < 4$ Mpc, they show very similar overall shapes and amplitudes. This again shows that our results about the shape of lensing profiles of **redMaPPer** clusters should be robust against imaging dataset and lensing measurements.

This paper has been typeset from a $\text{\TeX}/\text{\LaTeX}$ file prepared by the author.

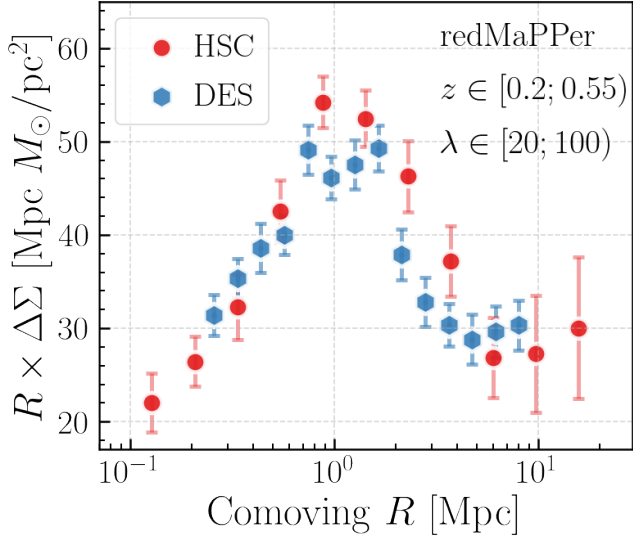


Figure G1. Comparison of the stacked $\Delta\Sigma$ profiles of HSC and DES redMaPPer clusters within the same richness ($20 \leq \lambda < 100$) and redshift ($0.2 \leq z < 0.55$) bin. The DES redMaPPer $\Delta\Sigma$ profile is from Chang et al. (2018). In different with the other $\Delta\Sigma$ profiles in this work, we use *comoving* coordinate here to be consistent with Chang et al. (2018). The Jupyter notebook for reproducing this figure can be found here: [🔗](#).